15 QCD processes at the LHC

15.1 Introduction

The study of QCD processes at the LHC will serve two main goals. First the predictions of QCD will be tested and precision measurements will be performed, allowing additional constraints to be established *e.g.* on the distribution of partons in the proton, or providing measurements of the strong coupling constant α_s at various scales. Second QCD processes represent a major part of the background to other Standard Model processes and signals of new physics at the LHC and thus need to be understood precisely in the new kinematic region available here. Deviations from the QCD expectations might themselves also indicate the occurrence of new physics, as in the case of compositeness for the jet transverse energy and di-jet invariant mass and angular distributions. Furthermore, the production cross-sections for almost all processes are controlled by QCD.

Tests of QCD can be performed by comparing measurements to fixed order (either LO (leading order) or NLO (next-to-leading order)) calculations or to leading-log Monte Carlo programs which contain $2 \rightarrow 2$ LO matrix elements and approximate higher orders through the use of parton showers (and also include the hadronisation of the partonic system). Perturbative QCD can also be tested by extracting (or constraining) the fundamental parameter α_s. The difference between a LO and a NLO calculation is quantified in the *K*-factor; the *K*-factor is defined as the ratio between the cross-section at NLO to the one at LO. The *K*-factor can become significantly larger than 1, especially when new sub-processes appear at next-to-leading order. Calculations at next-to-leading order are mostly restricted to parton level and often performed by numerical integration of the corresponding matrix elements.

This chapter gives an overview of different measurements of QCD processes [15-1], [15-2], [15-3] to be performed with ATLAS, classified by the main characteristics (or main selection criteria) of the final state. Besides a qualitative overview, a few examples are given where first quantitative investigations of the potential of ATLAS have been performed. The organisation of the chapter is as follows: the next section contains a brief summary on the present knowledge of parton densities and some perspectives for improvements before the start of LHC. Then measurements of properties of minimum-bias events (Section 15.3) are discussed, followed by a description of studies of hard diffractive scattering (Section 15.4). Next, the information to be deduced from the measurement of jets (Section 15.5) is described, followed by a section on photon physics (Section 15.6) and one concerning the production of Drell-Yan pairs and heavy gauge bosons (Section 15.7). Before concluding, the production of heavy flavours (charm, bottom and top, Section 15.8) is discussed.

Unless stated differently in the corresponding sections, the standard trigger settings have been used. The signatures listed in [15-4] for the first level (and the second level) of the trigger system consist mainly of inclusive signatures. It is foreseen to accept a fraction of events with lower thresholds and it is possible to include specific signatures (esp. at the higher levels of the trigger system) combining different objects and thus allowing lowering of the corresponding thresholds. One important exception is the case of hard diffraction and the case of minimum-bias events, where dedicated triggers will have to be employed.

15.2 Knowledge of the proton structure

15.2.1 Global parton analyses and parton kinematics at the LHC

The calculation of the production cross-section at the LHC both for interesting physics processes and their backgrounds relies upon a knowledge of the distribution of the momentum fraction x of the partons in the proton in the relevant kinematic range. These parton distribution functions (pdf's) are determined by global fits (see [15-5] for a pedagogical overview) to data from deep-inelastic scattering (DIS), Drell-Yan (DY), jet and direct photon production at current energy ranges. Two major groups, CTEQ [15-6] and MRS [15-7], provide regular updates to the parton distributions when new data and / or theoretical developments become available.

Lepton-lepton, lepton-hadron and hadron-hadron interactions probe complementary aspects of perturbative QCD (pQCD). Lepton-lepton processes provide clean measurements of $\alpha_s(Q^2)$ and of the fragmentation functions of partons into hadrons. Measurements of deep-inelastic scattering structure functions (F_2,F_3) in lepton-hadron scattering and of lepton pair production cross-sections in hadron-hadron collisions provide the main source of information on quark distributions $q^a(x,Q^2)$ inside hadrons. At leading order, the gluon distribution function $g(x,Q^2)$ enters directly in hadron-hadron scattering processes with direct photon production and jet final states. Modern global parton distribution fits are carried out to next-to-leading order (NLO) which allows $q^a(x,Q^2)$, $g(x,Q^2)$ and the strong coupling $\alpha_s(Q^2)$ to all mix and contribute in the theoretical formulae for all processes. Nevertheless, the broad picture described above still holds to some degree in global pdf analyses. In pQCD, the gluon distribution is always accompanied by a factor of α_s, in both hard scattering cross-sections and in the evolution equations for the parton distributions. Thus, the determination of α_s and the gluon distribution is, in general, a strongly coupled problem. One can determine α_s separately from e^+e^- interactions or determine α_s and $g(x,Q^2)$ jointly in a global pdf analysis. In the latter case, though, the coupling of α_s and the gluon distribution may not lead to a unique solution for either (see *e.g.* in [15-8]).

Currently, the world average of $\alpha_s(M_Z)$ is of the order of 0.118 – 0.119 [15-9]. The average value from LEP is 0.121 while the DIS experiments prefer a somewhat smaller value (of the order of 0.116 – 0.117). Since global pdf analyses are dominated by the high statistics DIS data, they would favour the values of α_s closer to the lower DIS values. The more logical approach is to adopt the world average and concentrate on the determination of the pdf's. This is what both CTEQ and MRS currently do. One can either quote a value of $\alpha_s(M_Z)$ or the value of Λ_{QCD}. For the latter case, however, the renormalisation scheme used together with the number of flavours has to be clearly specified. Usually the $\overline{MS}$ scheme is used. The specification of the number of flavours is important as the value of α_s has to be continuous across flavour thresholds. A range of $\alpha_s(M_Z)$ of 0.105 to 0.122 corresponds to the range of $100 < \Lambda_{QCD} < 280$ MeV for five flavours and to $155 < \Lambda_{QCD} < 395$ MeV for four flavours.

The data from DIS, DY, direct photon and jet processes utilised in pdf fits cover a wide range in x and Q. The kinematic 'map' in the $(1/x,Q)$ plane of the data points used in a recent parton distribution function analysis is shown in Figure 15-1. The HERA data (H1 and ZEUS) are predominantly at low x, while the fixed target DIS and DY data are at higher x. There is considerable overlap, however, with the degree of overlap increasing with time as the statistics of the HERA experiments increases. The DGLAP equations [15-10] in pQCD describe the change of the parton distributions with Q^2. The NLO DGLAP equations should describe the data over the whole kinematic range shown in Figure 15-1. At very low x, however, the DGLAP evolution is believed to be no longer applicable and a BFKL [15-11] description must be used. No clear evi-

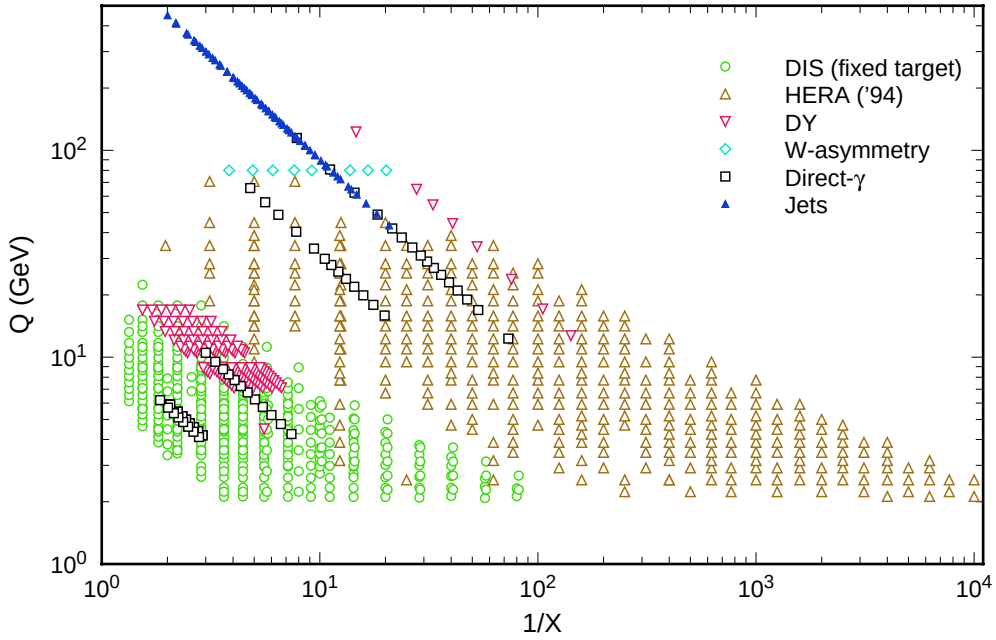

Figure 15-1 A kinematic map of data points in the *(1/x,Q)* plane from different processes used in a global fit of parton densities (from [15-5]).

dence of BFKL physics is seen in the current range of data; thus all global analyses use conventional DGLAP evolution of the pdf's. There is a remarkable consistency between the data in the pdf fits and the NLO QCD theory to fit these. Over 1300 data points are shown in Figure 15-1 and the χ^2 / DOF for the fit of theory to data is of the order of 1.

In Figure 15-2 the kinematics appropriate for the production of a state with mass M and rapidity y at the LHC is shown [15-12]. For example, to produce a state of mass 100 GeV at rapidity $y = 2$ requires partons of x values 0.05 and 0.001 at a Q^2 value of 10^4 GeV^2. The figure also shows another view of the kinematic coverage of the fixed target and the HERA experiments used in the pdf fits.

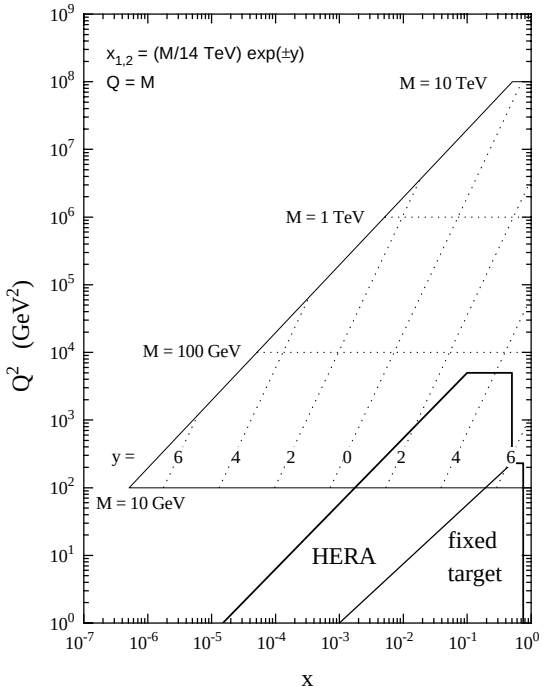

Figure 15-2 Parton kinematics at the LHC (from [15-12]) in the *(x,Q²)* kinematic plane for the production of a particle of mass M at rapidity y (dotted lines).

15.2.2 Properties and uncertainties of parton distribution functions

Figure 15-3 shows the parton distributions for the different quark flavours and the gluon as obtained from the CTEQ4M distribution [15-8] for a scale of $Q^2 = 20$ GeV^2, in Figure 15-4 the corresponding distributions are shown for a scale of $Q^2 = 10^4$ GeV^2. Clearly visible is the dominance of the gluon distribution for small parton momenta. In addition the violation of the flavour symmetry for $\bar{u}$ and $\bar{d}$ sea quarks can be seen.

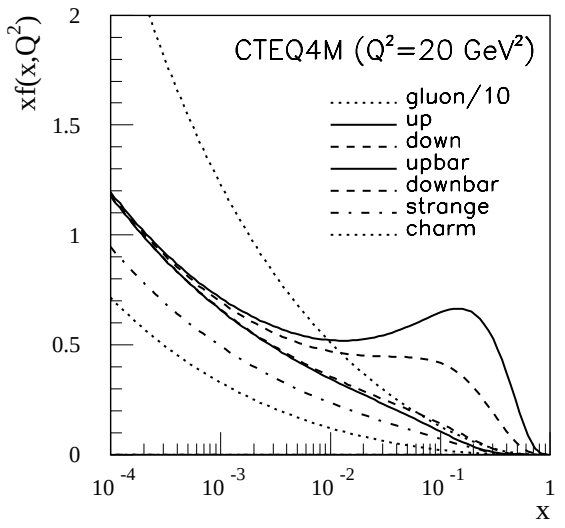

Figure 15-3 Parton distributions for the CTEQ4M pdf at Q^2 = 20 GeV^2. The gluon distribution has been reduced by a factor of 10.

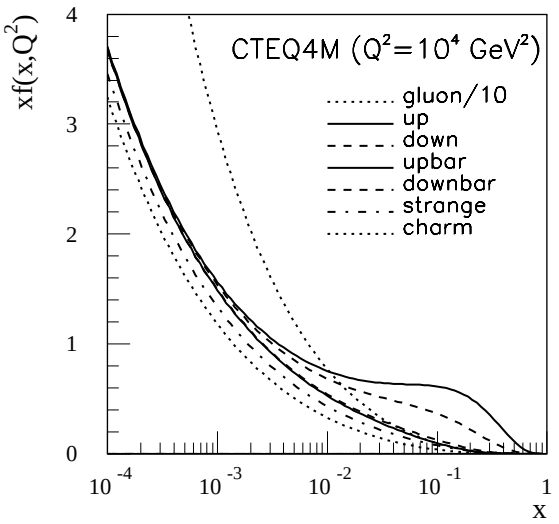

Figure 15-4 Parton distributions for the CTEQ4M pdf at Q^2 = 10^4 GeV^2. The gluon distribution has been reduced by a factor of 10.

Parton distribution determined at a given x and Q^2 'feed-down' to lower values of x at higher values of Q^2. The accuracy of the extrapolation to higher Q^2 depends both on the accuracy of the original measurement and any uncertainty on $\alpha_s(Q^2)$. For the structure function F_2, the typical measurement uncertainty at medium to large x is of the order of 3%. At high Q^2 (about 10^5 GeV^2) there is an extrapolation uncertainty of 5% in F_2 due to the uncertainty in α_s.

Figure 15-6 shows the gluon distribution as a function of x for five different values of Q^2, using the CTEQ4M distribution. Most of the evolution takes place at low Q^2 and there is only little evolution for x values around 0.1. In contrast, at an x value of 0.5, the gluon distribution decreases by a factor of approximately 30 from the lowest to the highest Q^2.

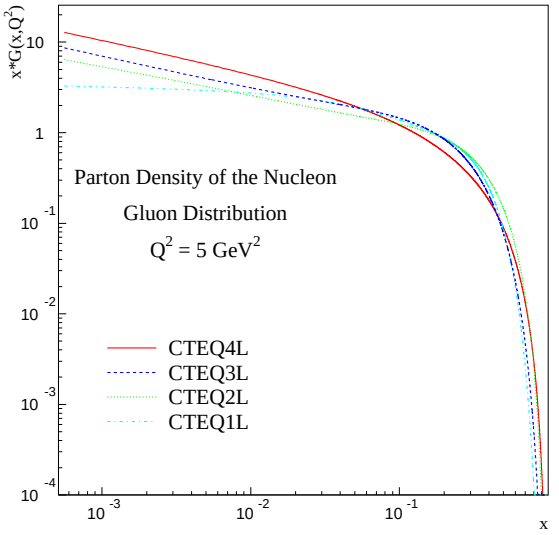

Figure 15-5 Gluon distribution for the CTEQ1L, CTEQ2L, CTEQ3L and CTEQ4L pdf's at a value of Q^2 = 5 GeV^2 (from [15-5]).

Global fits can also be performed using leading-order (LO) matrix elements, resulting in leading-order parton distribution functions. Such pdf's are preferred when leading order matrix element calculations (such as in Monte Carlo programs like HERWIG [15-13] and PYTHIA [15-14]) are used. The differences between LO and NLO pdf's, though, are formally NLO; thus the additional error introduced by using a NLO pdf should not be significant. A comparison of the LO and NLO gluon distribution is shown in Figure 15-7 for the CTEQ4 set, where the LO distribution is CTEQ4L and the NLO distribution is CTEQ4M. The differences get even smaller at larger Q^2 values.

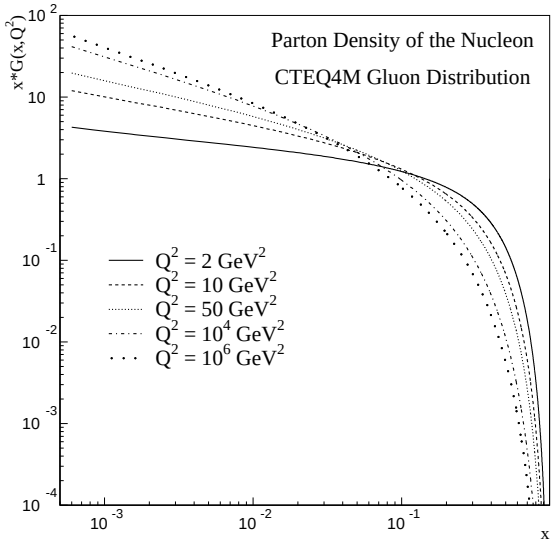

Figure 15-6 Gluon densities as a function of x from the CTEQ4M parton distribution set for five different Q^2 values: 2, 10, 50, 10^4 and 10^6 GeV^2 (from [15-5]).

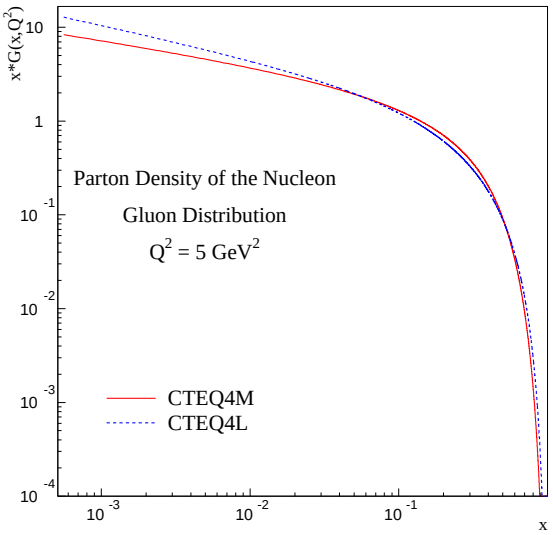

Figure 15-7 Comparison of the gluon distribution from the CTEQ4L (leading order) and the CTEQ4M (next-to-leading order) global fit (from [15-5]).

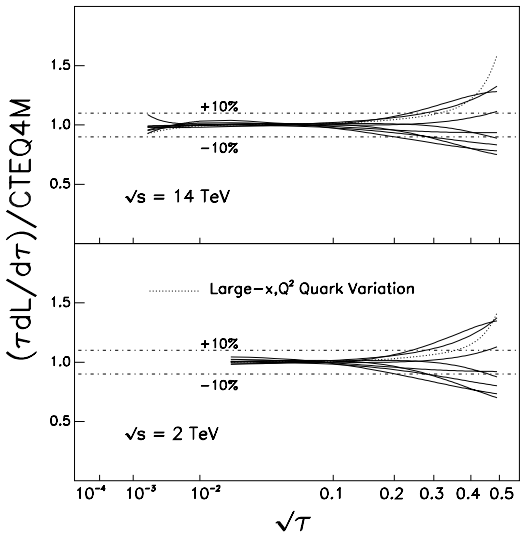

Figure 15-8 Normalised quark-gluon luminosity function (as a function of $\sqrt{\tau} = \sqrt{x_1 \cdot x_2}$) for variations in the gluon distribution which are consistent with existing DIS and DY datasets (from [15-17]). The dotted curve shows a toy model with more quarks at $x > 0.5$ for large Q^2 than in CTEQ4M.

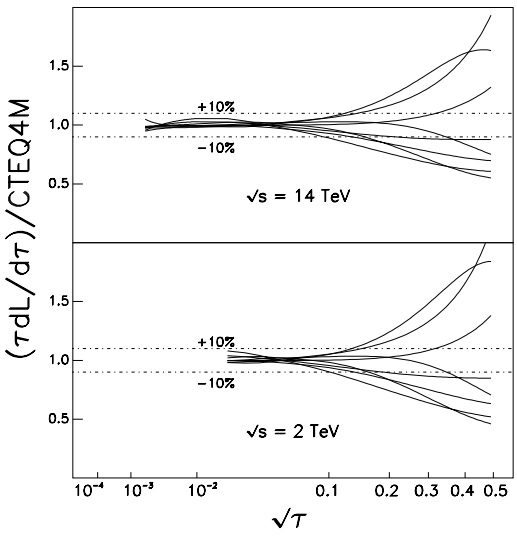

Figure 15-9 Normalised gluon-gluon luminosity function (as a function of $\sqrt{\tau} = \sqrt{x_1 \cdot x_2}$) for variations in the gluon distribution, which are consistent with existing DIS and DY datasets (from [15-17]).

Many of the comparisons in this document have been performed with the CTEQ2L pdf, a pdf that is on the order of five years old [15-15]. A comparison of the gluon distribution for CTEQ1L, CTEQ2L, CTEQ3L and CTEQ4L is shown in Figure 15-5. With increasing amounts of data included from HERA, the tendency has been for the low x pdf's to increase. The relative increases are reduced at higher values of Q^2.

In addition to having the best estimate for the values of the pdf's in a given kinematic range. it is also important to understand the allowed range of variation in the pdf's, *i.e.* their uncertainties. The conventional method of estimating parton distribution uncertainties is to compare different published parton distributions. This is unreliable since most published sets of parton distributions (*e.g.* from CTEQ and MRS) adopt similar assumptions and the differences between the sets do not fully explore the uncertainties that actually exist. Ideally, one might hope to perform a full error analysis and provide an error correlation matrix for all the parton distributions (see *e.g.* [15-16]). This goal may be difficult to carry out for two reasons. Experimentally, only a subset of the experiments usually involved in the global analyses provide correlation information on their data sets in a way suitable for the analysis. Even more important, there is no established way of quantifying the theoretical uncertainties for the diverse physical processes that are used and uncertainties due to specific choices of parametrisations. Both of these are highly correlated.

As the LHC is essentially a gluon-gluon collider and many hadron collider signatures of physics both within and beyond the Standard Model involve gluons in the initial state, it is important to estimate the theoretical uncertainty due to the uncertainty in the gluon distribution. The momentum fraction carried by gluons is 42% with an accuracy of about 2% (at Q = 1.6 GeV in the CTEQ4 analysis), determined from the quark momentum fraction using DIS data. This important constraint implies that if the gluon distribution increases in a certain x range, momentum conservation forces it to decrease in another x range. To estimate the uncertainty on the gluon distribution, an alternative approach has been carried out [15-17]: the (four) parameters of the gluon distribution (based on the CTEQ4 set) have been varied systematically in a global analysis and the resulting parton distributions have been compared to the DIS and Drell-Yan datasets making up the global analysis database. Only DIS and Drell-Yan datasets were used, as the experimental and theoretical uncertainties for these processes are under good control. Only those pdf's that do not clearly contradict any of the (DIS and Drell-Yan) data sets in the global analysis database were kept. The variation of the gluon distribution obtained with this procedure is less than 15% (10%) for low Q (high Q), except for large values of $x > 0.2$ (and very small ones $x < 10^{-4}$). In addition Figure 15-8 shows the effect of uncertainties on the quark distribution for x > 0.5, as obtained from a toy model (more details can be found in [15-17]).

To assess the range of predictions on physics cross-sections for a hard scattering process, it is more important to know the uncertainties on the gluon-gluon and the gluon-quark luminosity functions in the appropriate kinematic region of $\sqrt{\tau} = \sqrt{x_1 \cdot x_2}$. The relevant integrated parton-parton luminosity function is (in case of the gluon-gluon luminosity) defined as

$$\tau \frac{dL}{d\tau} = \int_{\tau}^{1} G(x, Q^2) G(x/\tau, Q^2) dx/x$$

This quantity is directly proportional to the cross-section for the *s*-channel production of a single particle and it also gives a good estimate for more complicated production mechanisms. In Figure 15-8 the allowed range of quark-gluon luminosities (normalised to the CTEQ4M values) is shown for the variations discussed above (for LHC and for Tevatron). The scale Q^2 is taken as τs, which naturally takes into account the Q^2 dependence of the gluon distribution as τ changes. The quark distributions in this case are taken to have no uncertainty, which is a reasonable assumption since the uncertainty on the gluon distribution is much larger. Figure 15-9 shows the corresponding variations in the gluon-gluon luminosity (normalised again to the values of the CTEQ4M distribution). For values of $\sqrt{\tau} < 0.1$ the resulting variation in the gluon-gluon and

quark-gluon luminosity function is less than 10%, for values of $\sqrt{\tau}$ between 0.1 and 0.2 (0.2 and 0.3) the variation increases to 20% (30%) for the gluon-gluon luminosity and 10% (15%) for the quark-gluon luminosity.

15.2.3 Expected improvements before the LHC start-up

DGLAP-based pQCD calculations have been extremely successful in describing data in DIS, DY and jet production, as well as describing the evolution of parton distributions over a wide range in x and Q^2 (for a recent review see *e.g.* [15-18]). From the pdf point-of-view, one of the current problems lies in the determination of the gluon density at high x. Fixed target direct photon cross-sections can serve as a primary probe of the gluon distribution at high x. However, rigorous theoretical treatment of soft gluon effects (requiring both k_T and Sudakov resummation) will be required before the data can be used with confidence in pdf fits [15-19].

Differential di-jet data from the Tevatron explore a wider kinematic range than the inclusive jet cross-sections. Both CDF and D0 have di-jet cross-section measurements from Run I which may also serve to probe the high x gluon distribution, in regions where new physics is not expected to contribute (*i.e.* at moderate E_{T}), but where any parton distribution shifts would be observable. The ability to perform such cross-checks is essential.

CDF and D0 will accumulate on the order of 2-4 fb^{-1} in Run II (2000-2003), a factor of 20-40 greater than the current sample. This sample should allow for more detailed information on parton distributions to be extracted from direct photon and DY data, as well as from jet production. Run III (2003-2007) could offer a data sample potentially as large as 30 fb^{-1}.

The luminosity upgrade foreseen at HERA in the year 2000 [15-20] should deliver to the experiments a luminosity of about 150 pb^{-1} / year, allowing for an integrated luminosity of about 1 fb^{-1} by 2005. This will allow an error of a few percent on the structure function F_2 for scales Q^2 up to 10^4 GeV^2. The gluon density, derived from the scaling violations of F_2, should be known to an accuracy of less than 3% in the kinematic range $10^{-4} < x < 10^{-1}$.

15.2.4 The role of data from ATLAS

ATLAS measurements of DY (including W and Z), direct photon, jet and top production will be extremely useful in determining pdf's relevant for the LHC. This data can be input to the global fitting programs, where it will serve to confirm / constrain the pdf's in the kinematic range of the LHC. Again, DY production will provide information on the quark (and anti-quark) distributions while direct photon, jet and top production will provide, in addition, information on the gluon distribution. Also the precise measurement of beauty production could be used to provide constraints on the gluon, however, in this case the present discrepancy between the theoretical prediction and the data from the Tevatron (which are a factor of 2 or more larger than the prediction) has to be resolved.

Another possibility that has been suggested is to directly determine parton-parton luminosities (and not the parton distributions per se) by measuring well-known processes such as W / Z production [15-21]. This technique would not only determine the product of parton distributions in the relevant kinematic range but would also eliminate the difficult measurement of the proton-proton luminosity (see Chapter 13). It may be more pragmatic, though, to continue to separate

out the measurements of parton pdf's (through global analyses which may contain LHC data) and of the proton-proton luminosity. The measurement of the latter quantity can be pegged to well-known cross-sections, such as that of the W/Z, as has been suggested for the Tevatron.

15.3 Properties of minimum–bias events

15.3.1 Importance of minimum–bias studies

Due to the high luminosity at the LHC, there will be up to an average of 25 inelastic collisions per bunch-crossing. The knowledge of the structure of these 'minimum-bias' events is of great importance for all physics studies to be carried out by ATLAS as well as a powerful diagnostic tool on the performance of the detector. Besides the properties of charged (and neutral) particle production, the understanding of jet structures with small transverse momentum ('mini-jets') is needed if vetoes on jet activity are to be used in physics analyses.

In this section, the selection of minimum-bias events is described (Section 15.3.2), followed by a brief overview of generators for minimum-bias events (Section 15.3.3) and a discussion of possible measurements (Section 15.3.4), including a comparison of the predictions by the different models.

15.3.2 Selection of minimum–bias events

In order to have an efficient detection of minimum-bias events, and to allow for a minimisation of uncertainties in the extrapolation due to the modelling of minimum-bias events, a very small acceptance loss is desirable. Given the angular acceptance in pseudorapidity of $|\eta| < 5$ in the ATLAS detector, the installation of additional detectors in the very forward region close to the beam-pipe is desirable. Possible locations along the beam-pipe outside of the ATLAS detector for such detectors can be found in Section 13.3.1, where also the acceptance for inelastic events as a function of the lower and upper limit on the pseudorapidity is described.

A trigger demanding signals in coincidence on both sides of the interaction region can select non-diffractive inelastic interactions with an acceptance loss of about 0.4%, if tagging is available in the region $3 < |\eta| < 7.5$. The acceptance of this coincidence for single-diffractive, double diffractive and central diffractive events is smaller and leads to an overall acceptance for inelastic events of about 90%. A large part of the diffractive inelastic events can be recovered by requiring activity in at least one of the two sides of the interaction point, *i.e.* a single arm trigger. If these dedicated forward detectors would not be available at the trigger, a selection of minimum-bias events could also be obtained from a trigger on random bunch crossings, taking into account only those crossings, where both proton bunches are filled.

15.3.3 Modelling of minimum-bias events

There are several models available, which can generate minimum-bias events and have been tuned to existing data up to highest available energies from Tevatron. The following four models have been considered HERWIG [15-13], ISAJET [15-22], PYTHIA [15-14] (a short description of these three models can be found in Section 14.4) and PHOJET [15-23]. The last generator is a

combination of ideas from the Dual Parton Model [15-24] approach to hadronic interactions at high energies and aspects of perturbative QCD (following very closely the approach of DTUJET [15-25]). The aim is to provide an almost complete picture of hadron-hadron, photon-hadron and photon-photon interactions at high energies.

The different settings used for these generators are summarised and commented in [15-26]. In the case of ISAJET and HERWIG, only simple models for minimum-bias events are used, which are restricted to soft physics processes. They do not attempt to connect soft and hard process. In PYTHIA and PHOJET on the other hand, this connection is made. PHOJET uses the Dual Parton Model for particle production at low transverse momentum and leading order QCD matrix elements for large transverse momentum processes (including parton showers to approximate higher order corrections). PYTHIA uses the leading order QCD matrix elements with a very low p_T cutoff to model low p_T non-diffractive physics. Both PHOJET and PYTHIA include multiple interactions.

In the case of PYTHIA, two different approaches to handle the divergences in the matrix elements have been considered: a sharp cut-off (‘Model1‘) and a smoothly varying cut-off (‘Model4’), corresponding to the value of the parameter MSTP(82) being equal to 1 or 4. The first setting significantly overestimates [15-26] the charged particle density as measured at the Tevatron (see below) and is not investigated further. In case of PYTHIA version 5.724, which is used in this document to model minimum-bias events (for more details see Section 2.3.2), the setting MSTP(82) = 4 is used together with the following two settings (as recommended): MSTP(2) = 2 (two loop expression for α_s in the matrix element) and MSTP(33) = 3 (inclusion of the *K*-factor in the hard scattering cross-section), which is labelled as ‘PYTHIA 5.724 - ATLAS’ in the figures. The most recent version 6.122 of PYTHIA has been also used. One important change for the generation of minimum-bias events is the introduction of an energy dependence for the transverse momentum cut-off. For the setting MSTP(82) = 4 it is recommended for PYTHIA 6.122 not to change the default parameters (shown as ‘PYTHIA 6.122 - Model4’). As will be shown below, using the parameters MSTP(2) = 2 and MSTP(33) = 3 in PYTHIA 6.122 for MSTP(82) = 4 (labelled ‘PYTHIA 6.122 - A’) is not able to describe the Tevatron data. For illustration, the predictions with these settings will however be shown (more details can be found in [15-26]).

15.3.4 Measurements

15.3.4.1 Total cross-section

The determination of the total cross-section in a luminosity independent way requires the simultaneous measurement of the elastic and the inelastic scattering rate. Details of this method can be found in Section 13.3.1. One important uncertainty in this measurement is the precise knowledge of the acceptance for inelastic events (minimum-bias events, single and double diffractive dissociation events as well as central diffractive events) and any possible model dependence for the acceptance determination.

15.3.4.2 Charged particle spectra and energy flow

At the LHC, minimum-bias events will make up the 25 interactions per bunch-crossing at high luminosity. In order to understand precisely their contribution to the measured quantities for the hard scattering events of interest, a detailed knowledge of the structure of the minimum-bias events is required. These measurements can in turn be used to verify and tune the corresponding models.

The event selection could be based on a trigger on random bunch crossings or on the tagging of minimum-bias events by demanding a coincidence in the forward detectors to be possibly placed outside the acceptance of ATLAS. For non-inclusive measurements further selection criteria have to ensure that only a single interaction has taken place in the bunch-crossing (*e.g.* by demanding only one reconstructed vertex in the event). One important aspect is the effect of the strong solenoidal field in ATLAS, which will lead to a decrease in acceptance for low p_T particles. Their detection could be improved by running in a special mode with the solenoidal field off, which should allow to measure the multiplicity as a function of pseudorapidity, without any measurement of the particle momenta.

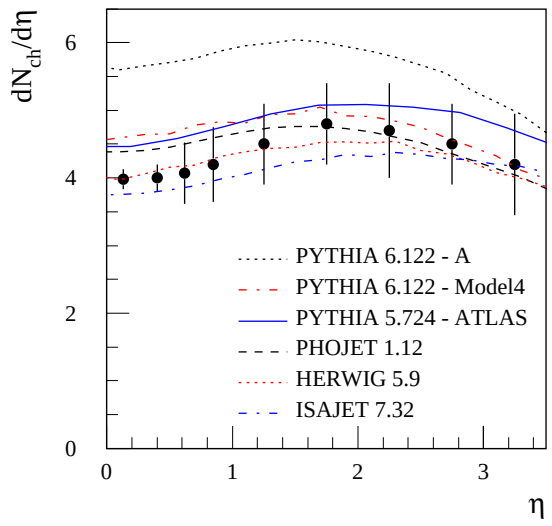

Figure 15-10 Charged particle density in minimum–bias events at Tevatron energies as a function of pseudorapidity (points, as measured by CDF [15-27]) and six model calculations (various curves). The PYTHIA 6.122-A model is shown for illustration only, as a non-recommended parameter setting was used.

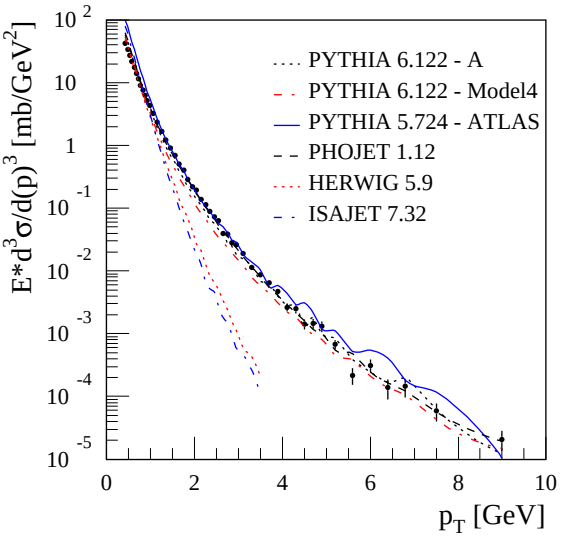

Figure 15-11 Transverse momentum spectrum of charged particles in minimum–bias events at Tevatron energies (points, as measured by CDF [15-28]) and six model calculations (various curves). For the HERWIG and ISAJET calculations, no hard scattering processes have been included.

In Figure 15-10 the charged particle density in minimum-bias events is shown as a function of pseudorapidity as measured by the CDF collaboration [15-27]. The data show a rather flat dependence on pseudorapidity with an average charged particle density of slightly more than 4 per unit of pseudorapidity. The data are well described by the HERWIG, ISAJET, PHOJET and PYTHIA (5.724-ATLAS and 6.122-Model4) calculations, whereas the new PYTHIA version 6.122 with the 'A' settings overestimates the Tevatron data significantly. For the central region ($\eta = 0$) the PYTHIA and PHOJET calculations slightly overestimate the data. Figure 15-11 shows the transverse momentum spectrum of charged particles in minimum-bias events as measured by CDF [15-28]. The two models where no hard processes have been included (HERWIG and ISA-

JET) clearly fail to describe the large transverse momentum part of the cross-section. Were a matching scheme (similar to the ones used *e.g.* in PYTHIA) between the soft process and the hard processes be provided, they should be able to also describe the transverse momentum spectrum. In contrast, the data are well described by PHOJET and the various PYTHIA calculations.

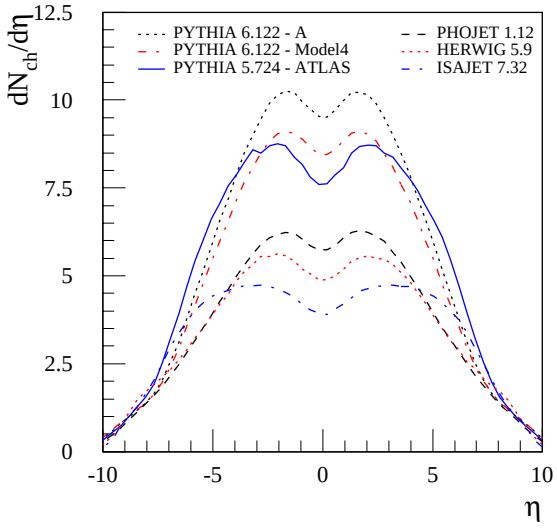

Figure 15-12 Charged particle density in minimum–bias events at LHC energies as a function of pseudorapidity, for six model predictions. The PYTHIA 6.122-A model is shown for illustration only, as a non-recommended parameter setting was used.

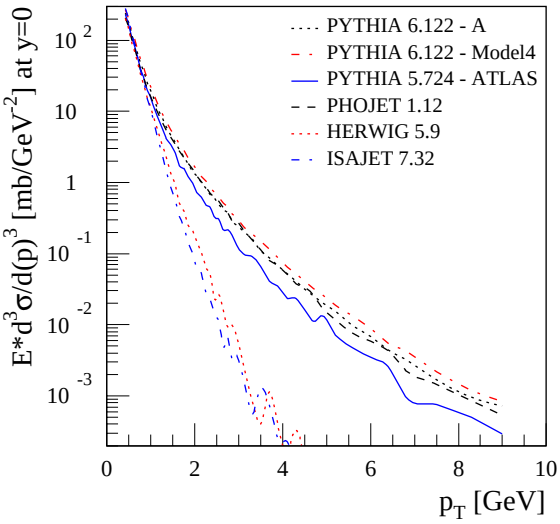

Figure 15-13 Transverse momentum spectrum of charged particles in minimum–bias events at LHC energies, for six model predictions. For the HERWIG and ISAJET calculations, no hard scattering processes have been included.

These six models are then used to give predictions for the LHC. In Figure 15-12 the expected charged particle density is shown as a function of the pseudorapidity and Figure 15-13 shows the cross-section for charged particle production as a function of transverse momentum. For the latter case, the two models (HERWIG and ISAJET), which failed to described the measured transverse momentum spectrum at the Tevatron, predict a very soft momentum spectrum. The reason is the same as for Tevatron energies: hard processes have not been included. It should be kept in mind however that they are able to describe the density of charged particles and their pseudorapidity distribution.

The predictions of HERWIG and ISAJET show very little dependence on the centre-of-mass energy in the average charged particle multiplicity. In the case of ISAJET the density is almost constant and for HERWIG it increases by about 1, similar is the case of PHOJET. The PYTHIA model predicts a larger increase in the charged particle multiplicity, going from about 4–5 at Tevatron energies to 8–9 at LHC energies (in the central region). The LHC predictions, shown over the full pseudorapidity range, show similar shapes for the different models (except for ISAJET and PYTHIA 5.724, which give a broader distribution). The largest charged particle density is predicted by the PYTHIA 6.122 calculation, using the ‘A’ settings. This is shown for illustration only, as the calculation overestimates already the Tevatron data. In case of the transverse momentum spectrum, the newest PYTHIA version predicts a slightly harder spectrum than the old version 5.724. Within the models presented, the calculation based on PYTHIA 5.724 with the ‘ATLAS’ settings appears to be a conservative estimate of the charged particle density in minimum-bias events.

Additional measurements could include the charged particle multiplicity as a function of the pseudorapidity, the scaled multiplicity distribution $n_{ch}/<n_{ch}>$ and the study of correlations between different particles, as was done at the Tevatron [15-29]. A differentiation between types of charged particles might be possible using a *dE/dx* measurement, as discussed in Section 3.4.4.

15.3.4.3 Jet structure and fragmentation functions at small transverse energy

The occurrence of jets with small transverse momenta (so called 'mini-jets') poses a challenge to QCD predictions. In order to study the transverse correlation between partons (see Section 15.5.6), jets with small transverse momentum have to be selected. At LHC energies, extrapolations predict that up to 50% of all inelastic events contain jets with transverse energies larger than 7 GeV. The understanding of the event structure in terms of jets with small transverse energy is important for the use of jet vetoing (see Section 9.1.3) or the identification of muons in the Tile calorimeter (see Section 5.3.3).

As the triggering of low energy jets in the LHC environment is an experimental challenge, the information obtained from a minimum-bias trigger at LVL1 (using either random bunch crossing or the information from additional dedicated detectors in the forward region) can be used to study the properties of these inelastic events not only in terms of particle production, but also in terms of jets with small transverse momenta and their properties. The higher level triggers of ATLAS could be used to provide an enriched sample of minimum-bias events with jet activity, by performing a jet reconstruction. Further studies are needed to quantify the reach in the minimum transverse energy to be accepted with such a selection scheme.

15.4 Measurements of hard diffractive scattering

15.4.1 Overview

In the 60s and 70s the Regge model provided a simple and efficient description of many measurements and phenomena in soft hadronic interactions. It was based on the principles of unitarity, analyticity and crossing symmetry. In addition to the Regge trajectories corresponding to the known mesons and baryons, an additional trajectory had to be introduced to describe deviations from a fall of the total cross-section nucleon-nucleon scattering like $s^{-1/2}$ and latter also the unexpected rise of the total cross-section with energy, as first noticed from the ISR data. This trajectory was named the Pomeron trajectory. It carries the quantum numbers of the vacuum and thus it can also be used to describe elastic scattering. Furthermore it also turned out to be a useful concept for the description of diffractive phenomena. Until recently there has been lack of interest in diffraction. The understanding of diffractive phenomena from first principles (*i.e.* from the Langrangian of QCD) is a 'first class challenge' to theory, which in the last few years has received revived attention due to the appearance of hard diffractive processes, *i.e.* diffractive processes in which a hard scatter takes place.

In terms of final state properties, diffractive events are characterised by the occurrence of rapidity gaps which are not exponentially suppressed with increasing gap size, as would be expected for gaps produced by fluctuations in the hadronisation of a non-diffractive event. Another characteristic property of the final state of single-diffractive (and central-diffractive) events is the appearance of a leading hadron, *i.e.* a hadron with a momentum close to the beam momentum (*e.g.*

$pp \rightarrow pX$). This hadron scatters quasi-elastically and is (due to kinematics) separated from the diffractive final state X by a distance $\Delta\eta$ in pseudorapidity. The value of $\Delta\eta$ depends on the centre-of-mass energy $\sqrt{s}$ and the invariant mass M of the system X through the relation: $\Delta\eta = \ln(s/M^2)$. At the LHC, typical values of $\Delta\eta$ are about 5.3 for $M = 1$ TeV and 9.9 for $M = 100$ GeV.

The name diffraction is related to the behaviour of the cross-section for these events as a function of the momentum transfer. An exponential fall-off with increasing momentum transfer is observed, reminiscent of the properties of the diffraction of light on a circular aperture. A further characteristic of diffractive processes is a slow dependence on the centre-of-mass energy.

The first indication for a partonic structure in diffractive processes (as suggested in [15-30]) has been obtained by the UA8 collaboration [15-31], studying single diffractive dissociation of protons and finding evidence for jets in the diffracted final state. This class of diffractive processes is called hard diffractive scattering, due to the presence of a hard (short distance) scale. Hard diffractive scattering is expected to be part of the inclusive hard scattering cross-section [15-32], and the measurement of jets, W/Z, direct photon and heavy flavour production has been suggested to provide information about the dynamics of the process. The UA8 data furthermore suggested that in part of the events almost the full Pomeron momentum participates in the hard scattering. This was named the ‘superhard Pomeron’.

The observation of deep-inelastic scattering (DIS) events at HERA with a rapidity gap revived interest in diffractive physics. This class of events was predicted by only a few people (*e.g.* in [15-30], [15-33] and [15-34]) and has now become a major part of the HERA physics programme [15-35]. One of the main motivations is to use deep-inelastic scattering as a probe of the colourless exchange governing diffractive scattering, which often appears under the name of the Pomeron. At HERA, typically about 10% of deep-inelastic scattering events can be attributed to a diffractive process.

The occurrence of hard scattering can be related to a partonic structure and a variety of measurements (production of jets, W and Z bosons and of Drell-Yan pairs [15-36] and the production of heavy flavours [15-32]) can be used in a similar way as in non-diffractive inelastic proton-proton interactions to provide constraints on parton densities. Given a set of derived parton distribution functions, a whole set of questions can be addressed: are these described by QCD evolution in the Q^2 dependence, is there agreement (universality of) between pdf’s extracted in different reactions (photon-Pomeron, proton-Pomeron or Pomeron-Pomeron), and are the pdf’s independent of the description of the coupling of the Pomeron to hadrons and so forth?

The inclusive single diffractive dissociation $pp \rightarrow pX$ is described by two variables: the (longitudinal) momentum fraction ξ and the square t of the momentum transfer at the vertex of the quasi-elastically scattered proton. The fraction ξ is related to the momentum fraction x_L of the scattered proton by $\xi = 1 - x_L$. Regge factorisation states the universality of the Pomeron trajectory (and other Regge trajectories) and assumes that only the coupling of the trajectory to a hadron depends on the nature of the hadron. This implies a decomposition of the inclusive cross-section for single diffractive dissociation into two factors: one describes the coupling of the Pomeron to the hadron (the flux factor), the second represents the inelastic cross-section between the Pomeron and the other hadron leading to the diffractive final state.

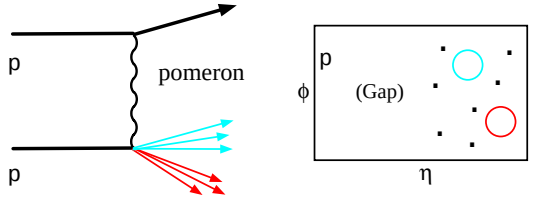

Figure 15-14 Single diffractive dissociation with jet production (adapted from [15-37]).

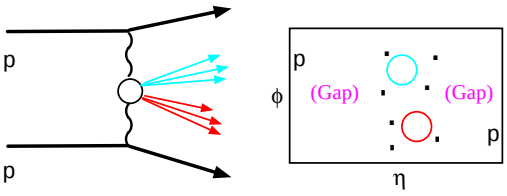

Figure 15-15 Central diffraction (double Pomeron exchange) with jet production (adapted from [15-37]).

In Figure 15-14 a sketch of a single diffractive dissociation event is shown, containing a hard scattering process leading to the production of two jets. In the η-ϕ phase space, the diffracted final state contains the two jets and is separated by a rapidity gap from the scattered proton. A similar sketch is given in Figure 15-15 for central diffraction (double Pomeron exchange), where the diffracted system is separated by two gaps from the two scattered protons.

15.4.2 Existing studies of hard diffraction

Detailed measurements of diffractive DIS (inclusive cross-section and final state studies) at HERA [15-35] supported the partonic interpretation and found that the process is dominated by gluons. A further area of investigation at HERA is the production of vector mesons (like ρ, ω, ϕ, J/ψ) which allows studies of the transition between soft and hard processes due to several available scales (mass M_V^2 of the meson, photon virtuality Q^2, momentum transfer t at the proton vertex) [15-38]. The HERA data are compatible with a factorisation of the measured diffractive cross-section into a flux factor and a term describing the partonic structure. However, it is necessary to invoke the contribution of non-leading trajectories besides the Pomeron to maintain the factorisation hypothesis. Assuming the validity of this approach, a structure function can be extracted, which exhibits clear scaling violations (different from those of a nucleon structure function, rather resembling those of a photon). The data indicate a dominance of the gluon distribution for all Q^2 [15-39]. These observations are supported by various measurements of final state properties in diffractive scattering at HERA, like topological variables, jet and heavy flavour production.

At the Tevatron, diffractive events in $p\bar{p}$ scattering were also observed by selecting events with a rapidity gap. Several classes were studied, including single diffractive dissociation with di-jet production [15-40], diffractive production of W bosons, double Pomeron exchange [15-41] and events with a rapidity gap between two jets [15-42][15-43][15-44]. The fraction of diffractive events for a given process (relative to the inclusive cross-section for this process) amounts to about 1%. Comparing this number to the results from HERA indicates a different survival probability for an event with a rapidity gap. At the end of run I, CDF installed a Roman Pot spectrometer to select elastically scattered anti-protons. Recently CDF observed also the diffractive production of J/ψ mesons and bottom quarks [15-45].

Measurements at the Tevatron of diffractive di-jet production and diffractive W production indicate a substantial difference in the rate compared to the prediction obtained using a factorisable model (see below) and the parton distributions as determined from the HERA data. The measured cross-sections are about a factor of 3 - 10 smaller [15-46]. One possible explanation is the (expected) breakdown of the (hard diffractive) factorisation model (which has been proven [15-47] only for the case of a single hadron beam in the initial state) in the case of hadron-hadron interactions. An interpretation of this factorisation breakdown is that spectator effects imply ad-

ditional soft interactions, which no longer lead to the diffractive final state. This would for example imply a different survival probability for the rapidity gap. A similar study for the di-jet production in double Pomeron scattering [15-48] leads to a factor of 10-100 with respect to the expectation in case of factorisation.

Indications for a perturbative behaviour in diffractive processes have been obtained from elastic photoproduction of J/ψ mesons in the reaction $\gamma p \rightarrow J/\psi p$ at HERA. The dependence on the photon-proton centre-of-mass energy $W_{\gamma p}$ due to exchange of a Regge trajectory is $d\sigma/dt = f(t)W^{2(2\alpha(t)-2)}$, where $\alpha(t)$ indicates the trajectory (*e.g.* the Pomeron trajectory as the leading one). Using HERA data to determine $\alpha(t)$, it was found [15-49] that the slope of the trajectory vanishes, *i.e.* there is no dependence on t. This behaviour not expected in the framework of the Regge model, where the diffraction peak (the sharp maximum of $d\sigma/dt$ for small $|t|$) 'shrinks' with increasing energy. Also in the measurement of single diffractive dissociation in $p\bar{p}$ collisions it was observed [15-50] that the differential cross-section as a function of x and t can best be described with a Pomeron trajectory containing a quadratic term, indicating either the onset of a perturbative Pomeron or the occurrence of multiple Pomeron exchange.

15.4.3 Models for hard diffractive scattering

Diffractive hard scattering, *i.e.* a diffractive process where in addition a hard scale is present, can be modelled under the assumption of diffractive factorisation. In this case, the cross-section for the process $pp \rightarrow pX$, where X contains a hard scattering, is given by the product of a diffractive parton distribution function, a parton distribution function for the proton and the hard scattering cross-section.

A relation to a partonic approach (similar to the quark parton model for the nucleons) has been proposed by several authors. One of the earliest ideas is due to Low [15-51] and Nussinov [15-52], who proposed as a QCD model for the Pomeron the exchange of a two gluon system in a colourless configuration. Bjorken and Kogut predicted the occurrence of hard diffractive processes in the context of the Aligned Jet Model [15-53] and the approach by Ingelman and Schlein [15-30] introduced the concept of parton densities for the Pomeron. The case of a 'superhard Pomeron' as mentioned above would imply in the partonic picture that one out of the two gluons carries almost the full momentum and the second gluon is a very soft one, which mainly neutralises the colour charge of the first one.

There are two places where factorisation might occur. Firstly, there is the so called Regge factorisation, which assumes that in a single diffractive process ($pp \rightarrow pX$) the vertex of the elastically scattered proton can be described independently of the reaction leading to the dissociative system. The proton-Pomeron vertex is described by a flux factor, depending only on the variables ξ and t. The inelastic reaction of the Pomeron with the second proton leads then to the dissociative final state X. The third ingredient is the Pomeron propagator.

Secondly, there is the hard scattering factorisation, which has been proven to be valid in the case where there is only one hadron beam involved (*e.g.* diffractive deep-inelastic scattering)[15-47]. In this case, the hard scattering cross-section is similar to a standard hard scattering cross-section with one of the two parton distribution functions replaced by a diffractive parton density. This parton density gives the distribution of a parton in a hadron under the condition that the outgoing diffracted hadron is detected and allows a separation of soft and hard processes. These diffractive parton densities avoid the concept of a Pomeron flux and the notion of Pomer-

on parton densities (as done in the Ingelman-Schlein model [15-30]), they are furthermore valid for all values of ξ. In the case of the Ingelman-Schlein model this is only true for small enough values of ξ, where Pomeron exchange is expected to dominate.

Based on a model for diffractive deep-inelastic scattering [15-54] which does not refer to the notion of a Pomeron, a model of soft colour rearrangement for hadron-hadron collisions has been proposed [15-55]. The model [15-54] for diffractive DIS assumes that after a normal hard scattering of the virtual photon on a parton of the proton, in part of the events, the exchange of a soft gluon (without changes to the momentum configuration of the partons) leads to the creation of two colour neutral systems, which then hadronise independently. In the case of hadron-hadron collision a similar mechanism could lead to the production of rapidity gaps in the case of a hard scattering process.

For the studies done on hard single diffraction (Section 15.4.5) and on hard central diffraction (Section 15.4.6), the PHOJET Monte Carlo program [15-23] has been used. The modelling of hard diffractive scattering is based on the approach of diffractive hard scattering factorisation, where the Pomeron is treated as a 'quasi-particle' and is assigned parton densities. Three possible parametrisations have been used (where in the case of the first two the Pomeron contains only gluons): a 'soft' gluon distribution ($xg(x) \propto (1-x)^5$), a 'hard' gluon distribution ($xg(x) \propto x(1-x)$) and a distribution ('CKMT parametrisation') containing both quarks and gluons in the Pomeron including the evolution according to the DGLAP equations. The hard scattering is described by leading order matrix elements, with parton showers added to approximate higher order corrections and hadronisation in the Lund String model. A comparison of the predictions of the PHOJET program to data obtained at the Tevatron can be found in [15-56].

15.4.4 Trigger and event selection

15.4.4.1 Rapidity gap signature

One of the possible ways to select diffractive scattering is to demand the presence of a rapidity gap in the final state, *i.e.* a region in phase space without particle production. The occurrence of such regions in 'normal' hard scattering events is expected to be suppressed strongly with growing size of the region in rapidity. In order to have good acceptance it is desirable to cover a large region in rapidity, going beyond the ATLAS acceptance of $|\eta| < 5$. An example for such detectors can be found in [15-57], where the TOTEM collaboration describes the integration of their inelastic detectors (covering the region $3 < |\eta| < 7$) into the environment of the CMS detector at interaction region IR5.

By tagging events only through the existence of a rapidity gap in the forward region (without observing the leading system), it cannot be completely excluded (due to the limited acceptance of the detector in the forward direction) that the unobserved leading system is, instead of a proton, a low mass proton excitation or a dissociative system of small mass. When a cross-section is measured, this contribution has to be estimated and subtracted. The acceptance for such forward going dissociative systems (as a function of their invariant mass) depends on the coverage in pseudo-rapidity in the forward direction. This acceptance can be obtained from a simulation of the detectors used for tagging and could be cross-checked (in case a leading-proton measurement is possible) using events with a measured scattered proton. The measurement of the proton momentum allows the determination of the mass of the forward-going system and with this the acceptance can be obtained from data.

15.4.4.2 Leading–proton detection

A very clean way of selecting single-diffractive events is the tagging and measurement of a leading proton, *i.e.* a quasi-elastically scattered proton with an energy close to the nominal beam energy. This can be achieved by placing position-sensitive detectors downstream of the interaction point close to the nominal beam trajectory. These detectors are usually put into so called 'Roman Pots' [15-58], in order to move them away from their nominal position during injection and tuning of the beam. The insertion of such detectors should not increase the background significantly. The detectors would also probably only be installed (or moved close to the beam) in the case of low-luminosity running. Further studies need to be performed to determine the impact of beam-halo interactions with the Roman Pots.

The momentum loss $\xi = \Delta p/p_0$ ($\xi = 1 - x_L$) of a proton can be obtained from a measurement of the displacement (transverse to the beam) away from the interaction point. The acceptance in ξ is limited by the transverse beam size σ_{beam} (this determines how close to the nominal beam position the detectors can be placed – usually up to (10–20)×σ_{beam}) and the dispersion of the machine. The resolution in ξ has a fundamental limit, which is the natural momentum spread of the beam, expected to be about 10^{-4} at the LHC. This limit can only be reached if several independent measurements are performed to determine the position and the angle of the proton at the interaction point. The use of a single measurement is limited by the width of the beam of scattered protons. A study [15-59][15-60] of the low β insertions at the LHC showed that, at a distance of about 200 m from the interaction point, a minimal ξ of $\xi_{\min} = 0.01$ can be reached (the ξ range for 80% acceptance is $0.01 < \xi < 0.09$). Going to distances larger than 300 m from the interaction point, gives a lower limit of $\xi_{min} = 2 \times 10^{-3}$ (80% acceptance for $0.002 < \xi < 0.015$). The acceptance in ξ could be increased to smaller values of ξ only for finite values of t.

A selection of leading protons by demanding $x_L > 0.9$ selects the kinematic region where Pomeron exchange is expected to dominate the diffractive process. This corresponds roughly to a demand for a rapidity gap of at least 4 units. The region of smaller x_L values is of interest for the studies of non-leading trajectories. For the studies presented in the next sections, it is assumed that Roman Pots will be able to measure scattered protons with $x_L > 0.9$ and $0.01\ \text{GeV}^2 < |t| < 1\ \text{GeV}^2$ on both sides of ATLAS. Further studies need to be performed when a more detailed design of a possible Roman Pot system is available, to determine in more detail the acceptance and the resolution to be obtained. Given the large separation of the detectors from the ATLAS interaction point (about 200 m), it is not yet clear whether it is possible to include a trigger on track segments in the Roman Pots at the first level of the ATLAS trigger system, which has a maximum latency of 2.5 μs [15-61]. Although a large fraction of this latency would be used for the protons to arrive at the detectors and for the signals to be brought back to the trigger electronics, it may be possible to provide a fast decision and to distribute this to the front-end electronics. However, a detailed feasibility study has not yet been performed.

More details on the layout of the LHC interaction regions (IR1 and IR5) can be found in [15-57]. In the proposal for the measurement of the elastic and total cross-sections by the TOTEM collaboration a detailed description of the planned Roman Pot detectors for the interaction region IR5 (CMS) is given, which can be transferred identically to the ATLAS interaction region (IR1). For the measurement of elastic scattering, a station of two Roman Pots is foreseen in front of the dipole D2, measuring the transverse displacement. For elastic scattering, the acceptance in momentum transfer strongly depends on the value β^* (being the value of the β function at the interaction region). For the high-luminosity running mode ($\beta^* = 0.5$ m, corresponding to small transverse beam sizes) the minimal $|t|$ is about 200 GeV^2. At injection, a value of $\beta^* = 18$ m is foreseen, implying an acceptance in $|t|$ between 1 GeV^2 and 10 GeV^2, whereas for $\beta^* = 1100$ m a range of $0.02\ \text{GeV}^2 < |t| < 1.4\ \text{GeV}^2$ is covered. To measure protons from single-diffractive

scattering, a spectrometer consisting of up to three stations (each consisting of two Roman Pots) is proposed. The machine optics close to the interaction point (as viewed from the interaction point) are composed of the quadrupoles Q1 – Q3 (strong focusing triplet to achieve the small beam sizes), the bending dipoles D1 and D2 (to get the orbits into collision and separated back) and the quadrupoles Q4 – Q7 (to adapt the machine optics to the arcs). A figure of the arrangement of these magnets can be found in [15-57] (Figure 6). The first two locations are situated between the dipoles D1 and D2; the first before the neutral particle absorber (TAN), the second behind the TAN. The third possible location is found between the quadrupoles Q4 and Q5. For leading protons, *e.g.* from single diffractive scattering, the acceptance in t extends to smaller values than listed above for the case of elastic scattering. A detailed study of the machine layout is needed to obtain the acceptance (as a function of ξ and t) for the different values of β^*, as described above.

15.4.4.3 Final–state requirements

Given the large cross-sections for diffractive processes, even after taking into account the small acceptance for the detection of leading protons, it is obvious that for normal running conditions additional conditions on the final state have to be applied (in order to avoid prescaling). These will be done *e.g.* by requiring the presence of jets in the final state. The cut on the jet transverse energy will be lower than in the case of inclusive jet production in 'normal' QCD events. A possible requirement would be at least one (or two) jets together with either a leading-proton tag or a rapidity gap signature from the forward detectors (as mentioned in Section 15.3.2). Whether the first possibility would be available at the first trigger level, has to be determined (see Section 15.4.4.2). If this were not the case, a refinement of the gap selection at the higher levels of the trigger system would happen, where the Roman Pot information would be available. In any case, pre-scaled triggers using the Roman Pots and / or the inelastic detectors alone should be available, as also should be the case for diffractive triggers where the jet energy threshold is further lowered.

15.4.4.4 Background sources

The following sources of background to the production of diffractive events have to be considered: pile-up, in which a diffractive event without jet production and a non-diffractive event with jet production coincide. This would fake a signal for hard diffractive scattering and would occur dominantly in low-mass diffractive events. The simultaneous occurrence of a hard diffractive event and a minimum-bias event would be a real hard diffractive scattering, but could obscure the properties of the event (*e.g.* by filling the gap). A selection on a single interaction (by requiring only a single primary vertex be reconstructed) would remove most of these overlays. Also other physics processes with similar signatures such as events due to meson exchange or double diffractive dissociation, where a leading particle of one of the dissociated systems fulfils the selection criteria, will take place.

15.4.5 Single hard diffractive dissociation

The measurement of di-jet production in single diffractive dissociation by the CDF collaboration [15-62] used a sample of same-side ($\eta_1 \cdot \eta_2 > 0$) di-jet events with a minimum transverse energy of 20 GeV for each jet. Using the information on charged particles from the tracking detectors, on calorimeter towers and hits in the scintillators of the beam-beam counters, multi-

plicity distributions on the side opposite to the jet system were studied and a clear excess of events with zero multiplicity was observed. The fraction of di-jet events that are diffractive (normalised to the non-diffractive events) was determined to be $(0.75 \pm 0.05 \pm 0.09)\,\%$ [15-62]. A further study by CDF [15-40] used a sample of events at 630 GeV and at 1800 GeV, where a leading anti-proton ($0.04 < \xi < 0.095$ and $|t| < 1\ \mathrm{GeV}^2$) has been measured. This allows tagging of colourless *t*-channel exchange in the kinematic region where Pomeron exchange should dominate. In both samples, large E_T jet pairs are observed, with a distribution of transverse energy similar (with a slightly steeper slope) to the one of jets in non-diffractive events.

The measurement of the longitudinal momentum x_L of the scattered proton gives the momentum fraction ξ of the proton momentum which is taken by the Pomeron: $\xi = 1 - x_L = P_{IP}/P_p$. Reconstruction of the two jets in the final state system with transverse energies $E_{T\ 1,2}$ and pseudorapidities $\eta_{1,2}$ determines the momentum fraction β of the parton in the Pomeron participating in the hard scattering:

$$\beta = \frac{E_{T1}e^{-\eta_1} + E_{T2}e^{-\eta_2}}{2\sqrt{\xi}P_{beam}}$$

The shape of the β distribution gives information about the partonic structure of the Pomeron.

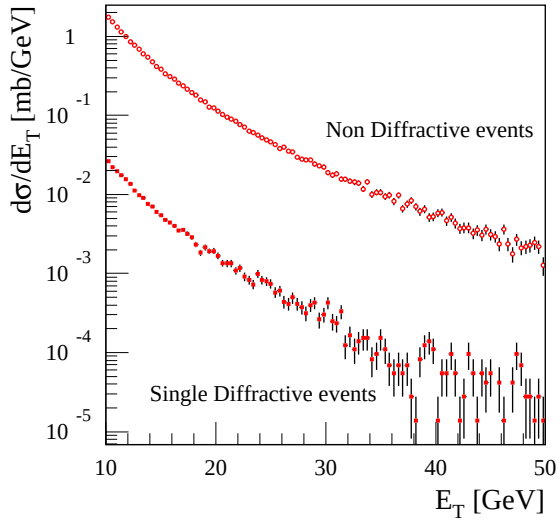

Figure 15-16 Cross-section for di-jet production ($|\eta^{jet}| < 3.2$) as a function of the jet transverse energy for non-diffractive and single diffractive events, obtained from the PHOJET Monte Carlo model.

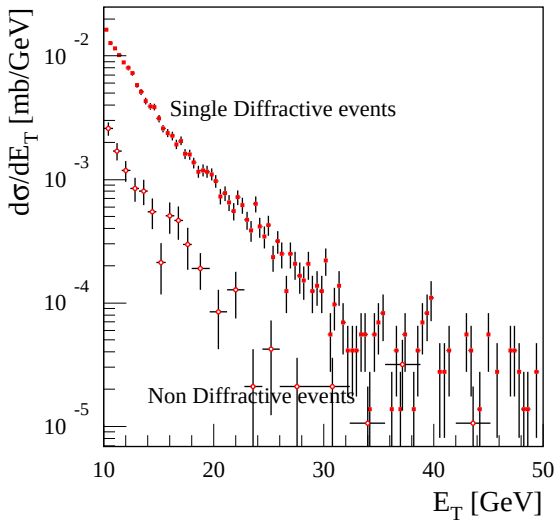

Figure 15-17 Visible cross-section for di-jet production ($|\eta^{jet}| < 3.2$) as a function of the jet transverse energy for non-diffractive and single diffractive events, when the detection of a leading proton is required (as obtained from the PHOJET Monte Carlo model).

Triggering of events with a hard diffractive interaction requires low transverse energy thresholds for the jets, due to the small invariant mass of the diffractive system. In Figure 15-16 the expected cross-sections for di-jet production with $E_T > 10\ \mathrm{GeV}$ and $|\eta| < 3.2$ are shown as a function of the minimum transverse energy (more details are to be found in [15-63]). As expected, the non-diffractive contribution has a cross-section which is almost two orders of magnitude larger than the single diffractive contribution. The rate for a di-jet trigger with low energy threshold would completely saturate the bandwidth of the trigger system. It can however be reduced by demanding the detection of a leading proton, as shown in Figure 15-17. This figure

shows the visible cross-section for the production of two jets with the same cuts as for Figure 15-16, but with the tagging of a leading proton with $x_F > 0.9$ and $0.01 < |t| < 1$ GeV^2 also being required. The non-diffractive cross-section is now smaller by about one order of magnitude than the single diffractive cross-section, although the ratio will be model dependent and needs to be verified using different models for the beam fragmentation region of the non-diffractive events.

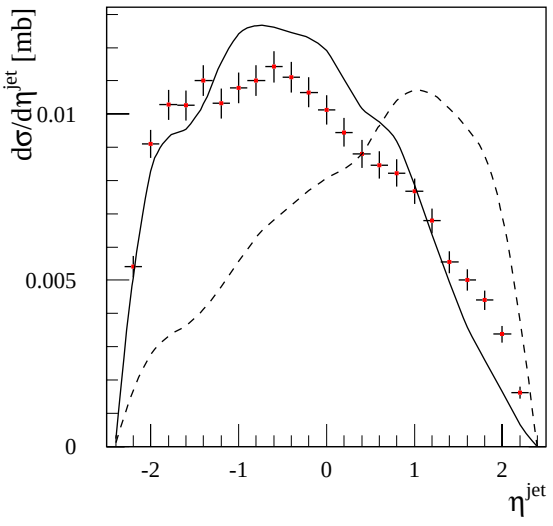

Figure 15-18 Cross-section for di-jet production ($|\eta^{jet}| < 3.2$ and $E_T > 10$ GeV) in single diffractive events with a tagged leading proton as a function of the jet pseudorapidity. Three different assumptions on the partonic structure of the Pomeron are shown: the CKMT parametrisation (points), a 'soft' gluon (solid line) and a 'hard' gluon distribution (dashed line).

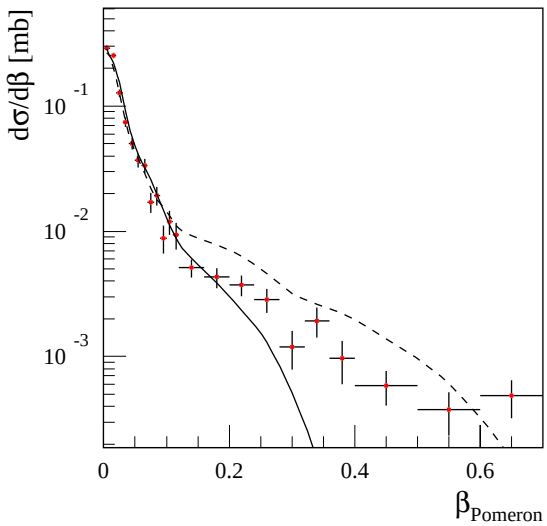

Figure 15-19 Cross-section for di-jet production ($|\eta^{jet}| < 3.2$ and $E_T > 10$ GeV) in single diffractive events with a tagged leading proton as a function of the momentum fraction variable β. Three different assumptions on the partonic structure of the Pomeron are shown: the CKMT parametrisation (points), a 'soft' gluon (solid line) and a 'hard' gluon distribution (dashed line).

In Figure 15-18 the cross-section for single diffractive events (tagged with a leading proton) with at least two jets with $E_T > 10$ GeV and $|\eta| < 3.2$ is shown as a function of the pseudorapidity of the two leading jets. Probably the actual minimum transverse momentum of the jets will be larger than 10 GeV, firstly due to constraints on the trigger rate and secondly due to the challenges in reconstructing jets with small transverse energy, where in addition the jet energy resolution is getting worse. Three different assumptions on the partonic structure of the Pomeron have been used: the CKMT parametrisation (shown as points), a soft gluon distribution (the solid line) and a hard gluon distribution (the dashed line). Between the last assumption and the first two, a very different shape is observed. Measuring the pseudorapidities of the two jets and their transverse energies allows the determination of the momentum fraction β of the partons in the hard scattering (assuming hard scattering factorisation). Figure 15-19 indicates the cross-section for single diffractive di-jet production as a function of β, for the same three assumptions on the partonic structure of the Pomeron. The differences between the assumptions are not as pronounced as in the case of the jet pseudorapidity distribution. More detailed studies are needed to assess the accessible kinematic range.

A further aspect of single diffractive dissociation is the production of a Higgs boson. The expected fraction of events with a Higgs boson being produced diffractively ranges between 10% and 25% (for $90 < m_H < 130$ GeV) [15-64] and 5% to 15% for a larger value of m_H [15-65]. The size

of the rapidity gap expected is small and no significant improvement in the signal-to-background ratio is expected, for the Higgs decays to two photons and to two Z bosons in the intermediate Higgs mass range.

15.4.6 Double Pomeron exchange

Double Pomeron exchange at the LHC is expected to give rise to final states of much larger invariant mass (up to 700 GeV) than at the Tevatron (with about 90 GeV), assuming a selection by demanding two leading protons with $x_F > 0.95$. The production of events with di-jets due to double Pomeron exchange, as suggested in [15-66], has been observed at the Tevatron [15-41]. In comparison with single diffractive hard scattering, an advantage of double Pomeron exchange is that almost no effects from underlying events or soft colour exchange are expected. The survival probability for the gaps should therefore not be influenced by these effects, as it is the case for single diffractive hard scattering. Taking into account $q\bar{q}$ production only, a cross-section of 5 nb at Tevatron energies has been calculated [15-66]. Events corresponding to double Pomeron exchange have been observed at the Tevatron, a study [15-41] by the CDF collaboration started from a sample of events with a tagged leading anti-proton ($0.05 < \xi < 0.1$ and $|t| < 1$ GeV^2), which contained at least two jets with $E_T > 7$ GeV. A study of the multiplicities of calorimeter towers and hits in the beam-beam counter scintillators on the outgoing proton side gave an excess at zero multiplicity, indicating the presence of double Pomeron exchange. The transverse energy spectra of the jets resembles those of single diffractive and non-diffractive events, but are more back-to-back in azimuth. The observed number of events is significantly smaller than expected from HERA data, assuming factorisation. Good agreement [15-41] can be obtained by reducing the prediction by a factor of 0.18^2, the square of the factor found in single diffractive di-jet production.

The study of double Pomeron exchange at LHC energies can be done in an inclusive way by demanding the presence of a leading proton in both 'Roman Pot' detectors (together with or without some activity in the central detector) or by taking a sample where at least one leading proton together with jet activity in the central part of ATLAS is required. The latter selection resembles the single hard diffractive selection, a lower jet E_T cut could be used by demanding in addition a rapidity gap opposite the leading proton.

Figure 15-20 shows the cross-section for central diffraction, resulting from Pomeron-Pomeron interactions, as a function of the invariant mass distribution of the final state. The solid line shows the cross-section without cuts on the outgoing protons, the dashed line has been obtained assuming that both protons are tagged with momenta corresponding to the values of $x_F > 0.9$ and $0.01 < |t| < 1$ GeV^2. As mentioned earlier, large invariant masses of the diffractive final state can be reached. This obviously implies the availability of the phase space for hard processes leading to the production of jets or electroweak bosons, which then can be used to probe the partonic structure. Requiring, in addition, the production of at least two jets with $E_T > 10$ GeV and $|\eta| < 3.2$ (indicated by the points in Figure 15-20), reduces the cross-section significantly and restricts the accessible invariant mass range to masses above 100 GeV.

Figure 15-21 shows for the selection of central diffractive events using two tagged protons and at least two jets, the cross-section as a function of the jet pseudorapidity for three different assumptions on the partonic structure of the Pomeron. The points corresponds to CKMT parametrisation, the solid line is a parametrisation using gluons only with a soft momentum distribution, *i.e.* most gluons have a small momentum fraction. These two assumptions give a

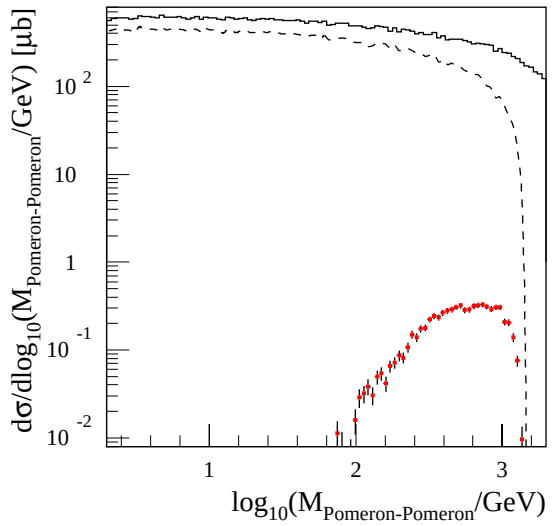

Figure 15-20 Cross-section for central diffraction as a function of the invariant mass of the diffractive system (the Pomeron-Pomeron invariant mass) for three assumptions: without final state requirements (solid line), requiring the detection of two leading protons (dashed line) and requiring in addition at least two jets with $|\eta| < 3.2$ and $E_T > 10$ GeV (points).

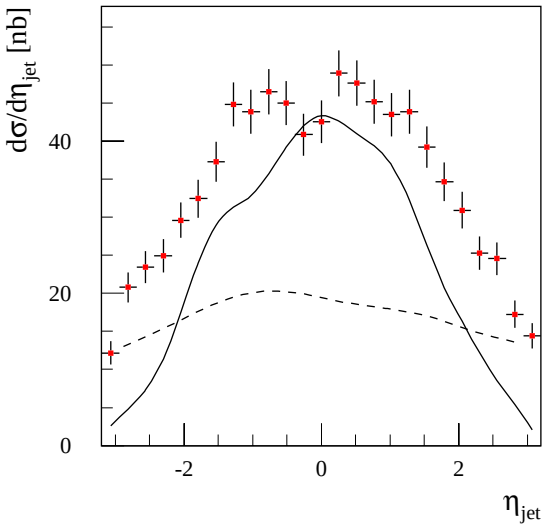

Figure 15-21 Cross-section for central diffraction (with both protons being tagged and at least two jets with $|\eta_{jet}| < 3.2$ and $E_T > 10$ GeV being found) as a function of the pseudorapidity of the jets. Three different assumptions on the partonic structure of the Pomeron are shown: the CKMT parametrisation (points), a 'soft' gluon (solid line) and a 'hard' gluon distribution (dashed line).

similar shape and differ mainly in the visible cross-section. The third assumption, shown as the dotted line, contains a hard distribution of gluons and exhibits a much flatter dependence of the cross-section on pseudorapidity.

Besides providing additional tests of the flux renormalisation (checks of factorisation breaking) the study of jet production in double Pomeron exchange allows studies of the partonic structure in a similar way to the ones done in non-diffractive proton-proton collisions. Selecting leading protons on both sides with $x_F > 0.9$ corresponds to having effectively a Pomeron-Pomeron collider with a maximal centre-of-mass energy of 1400 GeV. Calculations for the cross-section of double Pomeron events with di-jet production [15-67] indicate a cross-section between 0.05 and 0.3 nb for the kinematic range $0.002 < \xi_{1,2} < 0.03$, $|y_{jet\ 1,2}| < 1$ and $E_{T\ jet\ 1,2} > 20$ GeV.

The production of Higgs bosons via vector boson fusion can also lead to final states containing two scattered protons together with jets at large rapidities (in case of W and Z) and the Higgs decay products in the central gap region. As discussed in [15-68], the rapidity gap signature could be useful in improving the signal-to-background ratio. In double Pomeron scattering there is also the possibility to produce a Higgs boson in this reaction [15-69], leading to a final state with two quasi-elastically scattered protons and the decay products of the Higgs boson, separated by two gaps in rapidity from the protons, in contrast to the case of $WW \rightarrow H$ and $ZZ \rightarrow H$, where the protons are expected to scatter mainly incoherently.

About 1% of all events are predicted to be due to double Pomeron scattering [15-70]. Estimates of the cross-section for the process $pp \rightarrow ppH$, where the Higgs is produced and both protons are scattered quasi-elastically, give values of 0.3 to 0.02 pb for Higgs masses between 100 GeV and 1 TeV. The calculation is based on lowest order QCD diagrams, higher order corrections are expected to increase the cross-section. Backgrounds are due to the production of heavy-quark

pairs via the same mechanism, and should mainly contribute for small Higgs masses. Another issue is the survival probability of the rapidity gap. Allowing for proton dissociation, and demanding a rapidity of at least 6 units within which the Higgs is produced, increases the cross-section by up to a factor of 10 [15-71].

The mass resolution (using the missing mass technique) expected when both protons are detected is dominated by the beam divergencies at the interaction point [15-72]. In the case of the Tevatron, the expected mass resolution is about 300 MeV (for $\xi = 0.05$ and $|t| < 1\ \mathrm{GeV}^2$). The advantage of this method would be to avoid the small branching ratio for the decay of a Higgs to two photons by using the decay mode to $b\bar{b}$, while possibly allowing for small transverse momentum thresholds for the $b\bar{b}$ reconstruction. A trigger could be built from a coincidence between tags for leading proton in the Roman Pot spectrometers on both sides of the ATLAS detector, this selection could be refined by final state requirements using the central detector.

15.4.7 Colour-singlet exchange

Jet production in hadron-hadron collisions mainly proceeds by the exchange of a quark or a gluon between two partons, leading to a flow of colour between the two partons that give rise to the observed jets. Between the two jets therefore the production of particles is expected. If the exchange is a Pomeron or an electroweak gauge boson (W, Z or γ^*), a rapidity gap between the two jets is expected.

At Tevatron energies, the ratio of di-jet events with a gap to all di-jet events is expected to be of order 1% and probes the nature of the colourless exchange by studying the properties of the produced di-jet system. Different models for the colourless exchange predict different dependencies of the ratio on the size of the central gap and on the E_T of the jets. In case of electroweak exchange, the fraction is expected to be about 10^{-4}.

The production of events with a central rapidity gap (defined by measuring the multiplicity of calorimeter towers and charged particle tracks) between two jets has been observed at the Tevatron both by CDF [15-43][15-44] and D0 [15-42]. The measurement by D0 requires two jets of at least 30 GeV transverse energy. The colour singlet fraction determined from the data is $(0.94 \pm 0.04 \pm 0.12)\,\%$ [15-42]. This fraction is found to increase with increasing values either of the minimum E_T for the jets or the separation $\Delta\eta$ in rapidity of the two jets. This dependence can be used to discriminate between different models for the colour singlet exchange. The present D0 data disfavour a model based on two-gluon exchange, and favour a model using soft colour rearrangement. In contrast to the D0 data, the CDF collaboration does not find a significant dependence of the colour singlet fraction on E_T or $\Delta\eta$. The measurement [15-43] requires two opposite side jets with $E_T > 20$ GeV and $1.8 < |\eta_{jet}| < 3.5$. The colour singlet fraction amounts to $(1.13 \pm 0.12 \pm 0.11)\,\%$. A trigger for ATLAS could be based on the energy deposition in the forward calorimeters, which cover the range $3 < |\eta| < 5$. More details on such a trigger are given in Section 15.5.4.3, in the context of the study of BFKL signatures in di-jet production at large angular separation. The final event selection for studies of colour singlet exchange would - in contrast to the BFKL selection - require a gap in the central rapidity region.

15.4.8 Diffractive *W* and *Z* production

As in the case of inclusive *W* (and *Z*) production (see Section 15.7.3) for inelastic proton-proton scattering, the diffractive production of *W* (and *Z*) bosons constrains parton densities in single diffractive dissociation, as discussed in [15-73]. At the LHC it is not possible to make use of the correlation between the *W* charge (*i.e.* the charge of the decay lepton) and the out-going proton (anti-proton), as it was done in the measurement by CDF [15-74]. In this measurement, CDF observed that a fraction of $R_W = 1.15 \pm 0.55\,\%$ of all events with a *W* boson are of diffractive nature (under the assumption of a hard partonic structure of the Pomeron with quarks and gluons).

The production of diffractive di-jets is expected to be dominated by gluons, whereas the diffractive *W* production is dominated by quarks. The relative contribution of quarks and gluons can thus be constrained by a combination of both measurements. Results from the TEVATRON obtained by CDF [15-62] indicate a gluon fraction $f_g = 0.7 \pm 0.2$. This is compatible with the results obtained at HERA ($0.3 < f_g < 0.8$ obtained by the ZEUS collaboration, combining a measurement of the diffractive structure function F_2^D and of diffractive di-jet photoproduction [15-75]). The fraction of the momentum of the Pomeron carried by partons was determined to be $D = 0.18 \pm 0.04$, which reflects the fact that the observed cross-section is smaller than the one expected from the HERA data, assuming hard scattering factorisation. This indicates a breakdown of factorisation.

At ATLAS, the experimental selection of diffractive *W* and *Z* boson production could be based on the inclusive lepton triggers for inclusive vector boson production, as described in Section 15.7.3 and Section 15.7.4. The analysis of these events would then require a rapidity gap signature. Smaller transverse momenta could be accessed with prescaled triggers or by including in the trigger requirements for the selection of a leading proton or a rapidity gap in the forward direction, if the information from these dedicated detectors became available.

15.4.9 Diffractive heavy flavour production

Another tool to get information on the parton content in diffractive processes is the study of heavy flavour production [15-76]. A calculation of the cross-section for single ($pp \rightarrow p + Q\overline{Q} + X$) and double diffractive ($pp \rightarrow p + Q\overline{Q} + X + p$) heavy quark production [15-77] at an centre-of-mass energy of 10 TeV lead to the following predictions, which should increase slightly for LHC energies:

- charm production: $\sigma_{\text{single diffractive}} = 2 - 4\ \mu\text{b}$ (20 - 40%),
  $\sigma_{\text{double diffractive}} = 40 - 65\ \text{nb}$ (0.4 - 0.7%)
- bottom production: $\sigma_{\text{single diffractive}} = 0.5 - 1\mu\text{b}$ (15 - 40%),
  $\sigma_{\text{double diffractive}} = 6 - 15\ \text{nb}$ (0.2 - 0.5%)
- top production: $\sigma_{\text{single diffractive}} = 1 - 5\ \text{pb}$ (0.3 - 2%),
  $\sigma_{\text{double diffractive}} < 10\ \text{fb}$ ($< 6 \times 10^{-3}$)

where the numbers in brackets denote the fraction of the diffractive process with respect to the total cross-section. In the calculation, three models for the Pomeron parton distributions have been used, which differ in the parton content at the starting scale of the parametrisation (using quarks only, quarks and gluon and mainly hard gluons).

The detection of diffractive charm production could use the signature of a semi-leptonic decays or the reconstruction of charmed mesons (like D^{*+-}). Especially for the latter case, feasibility studies have to be performed. In the case of *b* quark production inclusive signatures (muon production) or the tagging of *b*-jets could be studied. At the Tevatron, the CDF collaboration has observed the diffractive production of *b* quarks as well as the diffractive production of J/ψ mesons [15-45].

A detailed study of the diffractive production of *b* quarks at the LHC and their properties has been performed in [15-60]. The cross-section for diffractive masses M_{diff} between 1.4 and 4.4 TeV amounts to 7.1 μb, the one for $0.44 < M_{diff} < 1.4$ TeV to 3.3 μb and for $140 < M_{diff} < 440$ GeV to 1.2 μb. The fraction of events with *b* quark production to the total diffractive cross-section varies between 3×10^{-4} (M_{diff} = 140 GeV) and 6×10^{-3} (M_{diff} = 4.4 TeV). The average pseudorapidity of beauty particles depends on the diffractive mass, but shows also sensitivity to parton distributions of the Pomeron. For a hard (soft) gluon distribution in the Pomeron, the average pseudorapidity of the beauty particles changes from -4 (-5) at M_{diff} = 140 GeV to 3.5 (0.5) at M_{diff} = 4.4 TeV when the leading proton is at positive pseudo-rapidity. For the acceptance of the Inner Detector of $|\eta| < 2.5$ a value of the diffractive mass between 700 and 4 TeV is expected. The ratio of the diffractive charm production to the diffractive beauty production ranges from a factor of about 15 at M_{diff} = 140 GeV to about 50 at M_{diff} = 4.4 TeV.

As in the case of diffractive vector boson production, a sample of diffractive heavy flavour production could be obtained from the triggers for *b* production (as mentioned in Section 15.8.3). For the case of diffractive charm production, the first level trigger would have to start with a rapidity gap signature or a leading proton candidate. Next the higher trigger levels could try to reconstruct final state signatures indicating the presence of open charm.

15.4.10 Summary on hard diffractive scattering

The increase of centre-of-mass energy from the Tevatron to the LHC could allow for more precise studies of hard diffractive scattering, and further understanding of the transition between perturbative and non-perturbative QCD. The advantage of the LHC is in the production of diffractive final states with larger masses, allowing the probing of partonic structure with a variety of different processes. A selection of events with two leading protons (or rapidity gaps on both sides of the detector) transforms the proton-proton collider into a Pomeron-Pomeron collider (with variable beam energy), where the maximal centre-of-mass energy ranges between the one of the S$p\bar{p}$S and the Tevatron collider.

Many open questions need to be addressed in further studies. This especially concerns the experimental selection of diffractive events, either using a leading proton signature or the presence of a rapidity gap. In the first case, the kinematic reach for the low β^* configuration of the interaction region needs to be determined, assuming the positions of the Roman Pot detectors as described in [15-57]. The reconstruction of the hard scattering in the central detector has to be studied for lower thresholds on transverse energy and momenta than in the case of proton-proton collisions, to take into account the effectively smaller centre-of-mass energy.

15.5 Jet physics

15.5.1 Overview

At hadron colliders, the most prominent signature for a hard scattering process to take place is the production of particles with a large total transverse momentum, *i.e.* the jets. The measurement of jets allows to draw conclusions about the hard scattering process. To do so one has to take into account the evolution of the partonic system from the hard scattering to the observed set of hadrons. This evolution includes parton showering (the creation of additional partons, typically with decreasing transverse momenta), the fragmentation (of coloured partons to the colourless hadrons), short lived particle decays and the effects of the underlying event as well as the ones of multiple interactions in a single bunch crossing.

In this section, several observables for jet production will be discussed: inclusive jet cross-section (Section 15.5.2), inclusive di-jet production (Section 15.5.4) and multi-jet production (Section 15.5.5). Further topics include aspects of jet fragmentation (Section 15.5.3) and the measurement of multiple parton scattering (Section 15.5.6).

15.5.2 Inclusive jet cross-section

15.5.2.1 Results from the Tevatron

The recent measurement of the inclusive jet cross-section by the CDF collaboration [15-78] up to transverse energies of 450 GeV showed an excess over the theoretical expectation from a NLO calculation at large transverse energies (> 250 GeV). This excess could be interpreted as a sign of new physics. However it could also be due to a lack of understanding of the underlying QCD process (*e.g.* the parton distributions in the proton). The CTEQ4 and CTEQ5 pdf fits have included the inclusive jet data both from CDF and D0 [15-79]. The high E_{T} jet data have little statistical weight, however, and the CDF excess remains when comparing to predictions using these pdf's. In the CTEQ4HJ fit, the high E_{T} jet data from CDF were given an enhanced weight. Using this distribution, the discrepancy between theory and data is reduced, but still present. The increase in the predicted cross-section comes about because of an increase in the gluon distribution at high x (a factor of two at $x = 0.5$). A similar measurement by the D0 collaboration [15-79] showed good agreement of the NLO calculation with the D0 data up to transverse energies of 450 GeV. The best agreement with the D0 data, however, is obtained with the CTEQ4HJ (and CTEQ5HJ) pdf's. A comparison of the data from the two experiments yields a 42% probability [15-80] that they are compatible, when taking into account the systematic errors and their correlations.

A further test of QCD can be performed by comparing the inclusive jet cross-sections for different centre-of-mass energies. This is best done by determining the ratio of the cross-sections from the data at 630 GeV and at 1800 GeV, and studying the ratio as a function of x_T, where x_T is the scaled transverse momentum of the jet: $x_T = 2p_T/\sqrt{s}$. The ratio is less sensitive to experimental and theoretical uncertainties, its value is determined by the evolution of parton densities, the amount of gluon emission and the running of the strong coupling constant. For values of $x_T > 0.1$, the CDF and D0 measurements agree; at lower x_T, some differences are present [15-80]. The theoretical expectation (based on NLO QCD) for the ratio is larger than the measured one, with a significance of about 3σ.

15.5.2.2 Experimental selection

The selection of inclusive jet production will be based on an inclusive jet trigger (at LVL1, for more details see Section 11.3.2) with a threshold of 180 GeV at low luminosity (290 GeV at high luminosity), where the jets have to be within $|\eta| < 3.2$. To cover a wider range in jet transverse energy (towards lower values), prescaled triggers will be used. At the higher levels of the ATLAS trigger and in the analysis, different jet algorithms can be applied. In the following a 'simple' cone algorithm [15-81] is assumed. Future studies have to show the advantages of using a recombination algorithm, like *e.g.* the k_T algorithm [15-82].

The details of the jet algorithm used in an individual analysis may depend on whether the jets are used for precision QCD comparisons and measurements or for jet spectroscopy. In leading-order predictions, each theoretical jet consists of a single parton. To completely reconstruct final states (for $t\bar{t} \rightarrow$ jets) one wants to correct the experimental jet 4-vector back to the parton value. At NLO, a jet can consist of two partons and for the first time structure can be explored. One does not want to correct for the energy 'out-of-cone' since this is at least partially described by the NLO calculation. The NLO calculation for three jet production has been recently completed. In this calculation [15-83], there are up to three partons in a jet, presumably allowing for a more detailed probe of the jet structure. It includes the one loop corrections to the $2 \rightarrow 3$ diagrams and the real emission in the $2 \rightarrow 4$ process. A NNLO calculation for the inclusive jet cross-section is still some time in the future since it involves the very difficult calculation of two-loop corrections. At NLO and beyond, the details of the jet algorithm become important, in particular if the calculations are to remain infrared safe.

15.5.2.3 Experimental uncertainties

One important aspect in all jet studies is the relation between the jet transverse energy measured in the detector and the 'true' transverse energy of the parton in the hard scattering process. The measured energy can differ from the 'true' one due to the following experimental effects (more details *e.g.* on the jet energy scale determination can be found in Section 12.5.1), not including theoretical uncertainties:

- the calorimeter response: deviation from uniform response over the acceptance (due to dead material, gaps and intercalibration errors), non-linearities in the response to low and high p_{T} particles, the knowledge of the e/π ratio and the p_{T} dependence of the jet particle content;
- the effect of the magnetic field in providing a p_{T} cut-off for particles to reach the calorimeter;
- the effect of the underlying event (in the same interaction as the hard scattering) and / or the contribution of other interactions in the same bunch-crossing;
- the production of neutrinos and muons inside a jet, which lead to a smaller energy deposition in the calorimeter;
- the finite size of the jet reconstruction volume, leading to a loss of energy not being attributed to the jet or to fluctuations of particles from other jets into the volume. This is only a problem if it is not modelled correctly by the NLO calculation.

All these effects lead to a smearing and shift of the jet energy. The correction for these effects has to be determined and be applied. The correction leads to the following sources of systematic uncertainties, which need to be quantified:

- knowledge of the jet energy scale of the calorimeters;
- knowledge of the energy resolution for jets;
- knowledge of the linearity of the calorimeter response (low and high p_T);
- understanding of the calorimeter response to hadrons, electrons and photons;
- knowledge of the jet trigger efficiency;
- knowledge of the luminosity for the overall normalisation.

The expected statistics at large jet E_T values implies a desirable control of the systematic uncertainties to a precision of less than 1% for energies below 1 TeV and to about 10% for transverse energies of about 3 TeV. The strategy for the determination of the jet energy scale is discussed in Section 12.5.1.

15.5.2.4 Theoretical uncertainties

The inclusive jet cross-section is calculated at next-to-leading order [15-84], this includes the one loop corrections to the tree level diagram of the $2 \rightarrow 2$ process and the real emission diagram in the $2 \rightarrow 3$ process. Due to the possible appearance of more than two partons in the final state, a jet algorithm has to be applied in the case of a NLO calculation. Comparison of a simple cone algorithm for the NLO partons with the experimental jet definition showed that the latter fails to merge sub-jets which are rather far separated. To cure this problem, an additional parameter was introduced in the jet definition at parton level: R_{sep}. Two partons are not joined in a single jet if their distance in η–ϕ space is larger than $R_{sep} \times R$, where R is the radius used for the cone definition. A value of R_{sep} of 1.3 approximately mimics the CDF and D0 experimental jet analyses. The knowledge of the theoretical prediction of the inclusive jet cross-section at NLO depends on the following uncertainties:

- renormalisation and factorisation scale dependence, where usually both scales are taken to be identical and only the common variation is investigated;
- jet definition for the NLO calculation (*e.g.* the R_{sep} parameter);
- knowledge of the parton distribution functions;
- the value of the strong coupling constant;
- uncertainties in the parton shower modelling;
- the impact of non-perturbative hadronisation effects, which are expected to be power suppressed ($1/Q$);
- modelling of the underlying event and modelling of minimum-bias events (pile-up due to multiple interactions per bunch-crossing).

The largest theoretical uncertainty in the prediction for the Tevatron jet cross-section comes at high E_T and is due to the uncertainty in the gluon distribution at high x. The next important uncertainty is due to the renormalisation scale dependence (as discussed in [15-85]), which does not show a strong E_T dependence.

15.5.2.5 Expected cross-section

The following results have been obtained using the ATLFAST simulation (see Section 2.5) of the ATLAS detector response and a leading order QCD calculation (PYTHIA [15-14]) of jet production, based on the CTEQ2L parton distribution [15-15]. Four samples with increasing cuts on the minimum transverse momentum of the hard scattering matrix element ($\hat{p}_T > 180$, 500, 1000 and 1380 GeV) have been generated, including the effects of initial and final state interactions, and of multiple parton scattering. This procedure has been chosen to produce a reasonable number of simulated events for large transverse momenta. However, threshold effects which lead to a distortion of the spectrum could not be avoided completely. The pile-up contribution to the energy resolution due to minimum-bias events was taken into account. The detector response has been unfolded from the result of the simulation to a cross-section at the hadron level. In addition, a pseudo *K*-factor (obtained from the JETRAD NLO result [15-84] and the PYTHIA LO result) was included to the unfolded cross-section, where details are described in [15-86]. Jets were defined using a cone algorithm with a cone size of R = 0.8. This value of 0.8 was obtained as a result of an optimisation procedure to achieve a compromise between out-of-cone losses and contamination from sources not related to the jet, *e.g.* from the underlying event, other jets or initial state radiation. More details on this optimisation can be found in [15-86].

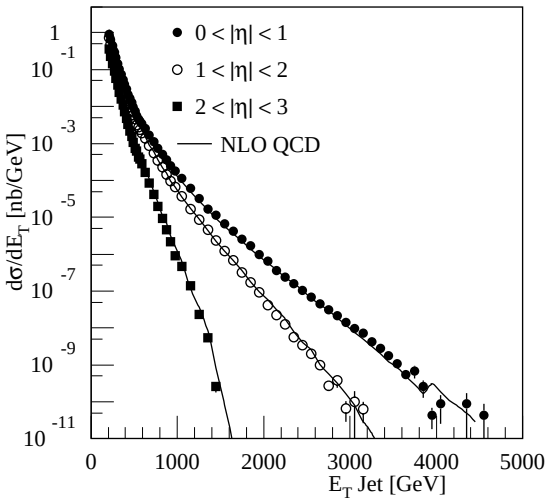

Figure 15-22 Inclusive jet cross-section (at hadron level) for different ranges of the jet pseudorapidity obtained from a PYTHIA calculation (points) and from a NLO Monte Carlo calculation (solid line).

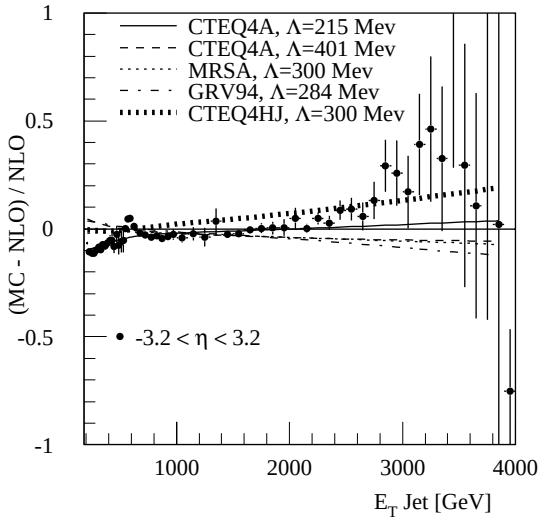

Figure 15-23 The ratio of the inclusive jet cross-section from PYTHIA (including a pseudo *K*-factor) to the one at NLO from the JETRAD calculation (including a hadronisation correction) is shown as points. Also shown is the relative difference to the NLO calculation for a variation of Λ_{QCD} and for different pdf's (the various curves).

In Figure 15-22 the inclusive jet cross-section is shown as a function of the transverse energy of the jet for three different bins in η: $0 < |\eta| < 1$, $1 < |\eta| < 2$ and $2 < |\eta| < 3$. The statistical error of the simulated events corresponds (for high E_T values) to the one expected for an integrated luminosity of 300 fb^{-1}. At small E_T values the statistical error is negligible. The expected statistics for an integrated luminosity of 30 fb^{-1} amounts to 4×10^5 events with $E_T^{jet} > 1$ TeV, 3000 events for $E_T^{jet} > 2$ TeV and about 40 events with $E_T^{jet} > 3$ TeV. Also shown in the figure is the

prediction of a NLO calculation (JETRAD) [15-84], using the CTEQ4M parton distribution set. This calculation of inclusive jet production at the parton level has been corrected for hadronisation effects, details are discussed in [15-86].

In Figure 15-23 the normalised difference of the simulated data to the NLO calculation is shown, as obtained from the CTEQ4M distribution and setting Λ_{QCD} (for five flavours) to a value of 300 MeV. This figure shows clearly the threshold effects that appear for transverse energies close to the matrix element cut-off $\hat{p}_T$. Further sources which could lead to a distortion of the spectrum are the parametrisation of the pseudo *K*-factor used to correct the PYTHIA cross-section and the hadronisation correction applied to the JETRAD calculation. The other curves indicate the relative difference between this reference NLO calculation and NLO calculations using different values for Λ_{QCD} (215 and 401 MeV) as well as using two other parton distribution functions (MRSA [15-87] and GRV94 [15-88]). The largest effect is observed when the CTEQ4HJ parton distribution is used. Based on the expected statistical accuracy in the region between 1 TeV and 2 TeV of transverse energy, the data should allow distinguishing between current distributions, like CTEQ4HJ and CTEQ4M. More studies are needed, however, to assess the expected systematic uncertainties.

15.5.2.6 Determination of α_s

An investigation has been carried out [15-89] as to whether it is possible to determine α_s and parton distribution functions from the collider data alone, without input from other experiments. As processes initiated by gluons play an important role and a strong correlation between α_s and the gluon distribution is expected, this probably excludes an independent determination of either quantity.

An extraction of the strong coupling constant α_s will not be able to compete with the precision measurements available from e^+e^- annihilation and deep-inelastic scattering. However the scale dependence of α_s could be determined in a single experiment (even a single process) over a large range in scale, including the highest achievable values of several TeV. This verification of the running of α_s implies a check of QCD at the smallest distance scales. As the running 'slows down' at large scales, this task is made more difficult. For a value of $\alpha_s = 0.118$ at 100 GeV the corresponding value at 4 TeV is about 0.075. A further possibility for an α_s determination is the production of multi-jets, as mentioned in Section 15.5.5. In the following, a possible procedure for a determination of α_s based on the inclusive or the triple differential jet cross-section is described. More studies are needed to arrive at quantitative conclusions about the potential accuracy.

The determination of α_s is based on the assumption, that the data can be described by perturbation theory with only small corrections for non-perturbative effects. The differential cross-section for inclusive jet production at next-to-leading order is the sum of two terms:

$$\frac{d\sigma}{dE_T} \sim \alpha_s^{\,2}(\mu_R)A(E_T) + \alpha_s^{\,3}(\mu_R)B(E_T)$$

where the functions *A* and *B* are calculated using parton distribution functions [15-89]. Fitting this expression to the measured inclusive cross-section gives for each E_T bin a value of $\alpha_s(E_T)$, which should show the running of the coupling constant. These values can then be evolved to the value of the coupling constant at the M_Z scale. The calculation of the functions *A* and *B* actually involves an assumption on the strong coupling constant, as global fits of parton densities are made for a certain value of α_s. To overcome this coupling between parton densities (espe-

cially the gluon density) and the strong coupling constant, a multi-step approach has been proposed in [15-89]. Firstly, parton distribution functions and the associated α_s value should be used to compare theory with data and to put constraints on the parton densities. In the next step, a particular set of parton distribution functions should be assumed as being correct and the strong coupling constant be extracted simultaneously for scales between several tens of GeV and several TeV (at the LHC). The third step would be a simultaneous determination of the strong coupling constant and the parton distribution functions from the triple differential di-jet cross-section. This step could be divided into two smaller levels: firstly, the quark distributions would be assumed as correct from the deep-inelastic scattering data and the gluon distribution would be determined. Secondly, information from other processes (like W/Z + jet production) would be included to also determine the quark distributions from the hadron collider data alone.

15.5.3 Jet shape and fragmentation

The definition of jets depends on their internal structure. Thus, it is important to provide direct measurements of it. The measurements will include the study of the jet shape, defined as the fraction of energy inside a cone of radius r ($r < R$) with respect to the cone of size R defining the jet. Existing measurements show broader jets at the Tevatron [15-90] than predicted by the HERWIG model. A comparison of the jet shape as a function of the jet transverse energy and the pseudorapidity of the jet with a next-to-leading order calculation [15-91] finds good agreement between the data and the calculation, provided that in the calculation the R_{sep} parameter determining the merging of partons is varied with the transverse energy and the pseudorapidity of the jets to take into account effects of jet broadening. Such a flexibility allows for few definite predictions. Furthermore similarities between the jet shapes in low Q^2 electron proton interactions and $p\bar{p}$ collisions were found. Jets do get narrower with increasing E_{T} and for a fixed value of E_{T}, jets are narrower in the forward region with respect to the central region.

When a k_T algorithm [15-82] is used to define a jet, sub-jets can be defined and their multiplicity being studied as a function of a resolution parameter as discussed in [15-92]. Recently, the NLO 3-jet calculation has been completed [15-83], which involves the 1-loop correction to the 3-jet cross-section. With up to four partons in the final state (and up to three in an individual jet), a more quantitative comparison with the experimentally measured shape of a jet is possible.

The measurement of charged particles in the Inner Detector will allow measurement of fragmentation functions. Since differences in the fragmentation function are expected for gluon and quark jets, the tagging of quark and gluon jets could provide additional information. Studies have to be performed to indicate the range in E_{T} where an efficient tagging is possible. From the fragmentation functions obtained, the information on scaling violations might lead to a determination of the strong coupling constant. An important application of a measurement of the fragmentation functions to charged particles for jets is the determination of the jet energy scale. The CDF collaboration uses this measurement to model the response of the calorimeter to jets in their determination of the energy scale [15-93]. An example for the measurement of charged particles inside jets is described in Section 3.5.2, using jets from the decay of a Higgs boson to $q\bar{q}$ and searching for tracks with $p_{\mathrm{T}} > 1$ GeV. Track reconstruction efficiencies of about 90% are obtained, together with a small probability of less than 0.4% for fake tracks.

15.5.4 Di-jet production

15.5.4.1 Triple differential cross-section

The measurement of the di-jet differential cross-section [15-94] for different values of the minimal E_T for both jets and of the two jet pseudorapidities $\eta_{1,2}$ allows selection of various kinematic regions in Q^2 and the parton momenta. At leading order, the parton momenta $x_{1,2}$ are then given by:

$$x_{1,2} = \frac{E_T}{\sqrt{s}}(e^{\pm\eta_1} + e^{\pm\eta_2})$$

Here the transverse energy of the leading jet is E_T and the pseudorapidities of the jets are given by $\eta_{1,2}$.

This relation expands to

$$x_{1,2} = \frac{1}{\sqrt{s}}\sum_{jets} E_{Tjet}e^{\pm\eta_{jet}}$$

for the case of NLO when more than two partons are produced. Their energies are assumed to be ordered in decreasing E_T. Theoretically it might be preferable [15-95] to measure the cross-section for di-jet production as function of the following three variables, $\eta^* = 0.5 \times |\eta_1 - \eta_2|$, and the two momentum fractions $X_{A,B} = \sum(E_{Ti}/\sqrt{s})e^{\pm\eta_i}$, depending on the transverse energies and pseudorapidities of the jets. The cross-section as a function of the leading jet transverse energy and the two pseudorapidities is not well behaved for large E_T, as there are large NLO corrections and consequent large uncertainties. In this region of phase space, the NLO cross-section is effectively a leading order cross-section, as the region is kinematically inaccessible at leading order.

Figure 15-24 shows examples of the differential cross-section for different jet rapidities, as obtained from a PYTHIA simulation (and compared to the results of the NLO calculation of JETRAD) using a similar approach as discussed in Section 15.5.2.5. Jets are pre-selected within the pseudorapidity range of $|\eta| < 3.2$ and the minimal transverse energy is 180 GeV.

In Figure 15-25 the expected range in x and Q^2 is shown, where for a given event the parton momentum fractions $x_{1,2}$ are calculated according to the formula mentioned above. The value shown has been chosen randomly between the two values available for the event, and the value of Q^2 has been calculated according to the expression

$$Q^2 \sim -\hat{t} = 2E_T^2\cosh\eta^{*2}(1 - \tanh\eta^*)$$

The size of the boxes is proportional to the number of events with these values. For a transverse energy threshold of 180 GeV, most of the events have Q^2 values of about 10^5 GeV^2 and values of $0.1 < x < 0.01$. Clearly visible is the kinematic boundary due to the centre-of-mass energy, which for a given momentum fraction leads to an upper limit on Q^2, where the latter increases with increasing x.

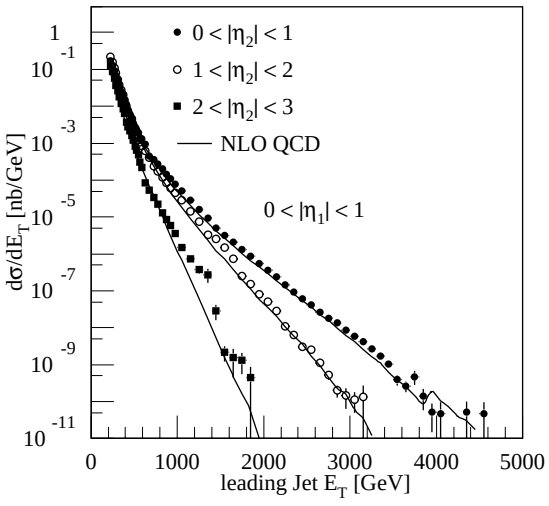

Figure 15-24 Di-jet cross-section (at hadron level with a leading jet $|\eta_1| < 1$) for different ranges of the pseudorapidity of the second leading jet obtained from a PYTHIA calculation (points) and from a NLO Monte Carlo calculation (solid line).

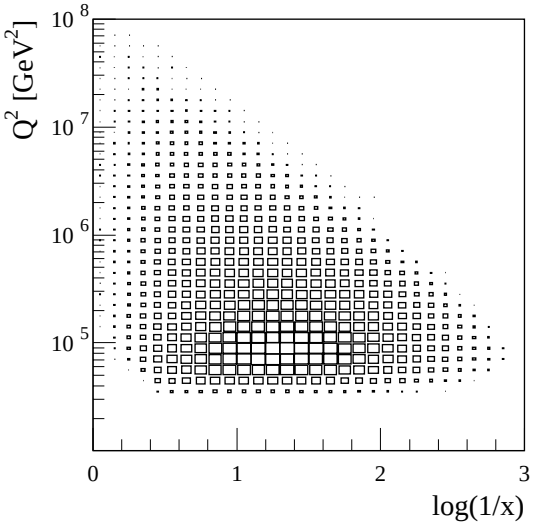

Figure 15-25 Range in *1/x* and Q^2 for the di-jet differential cross-section measurement. Only those bins are shown which contain more than 100 events for an integrated luminosity of 300 fb^{-1}.

At the Tevatron, the CDF collaboration chose to study the ratio of cross-sections where the leading jet is required to be central and the second jet is restricted to four slices in pseudo-rapidity [15-96] based on an integrated luminosity of less than 10 pb^{-1}. A cross-section based on the full statistics from Run I is to be published soon. Leaving the leading jet pseudorapidity fixed, the D0 collaboration studied the signed pseudorapidity distribution of the second jet [15-97]. Ultimately it should be possible to derive from the triple differential cross-section both the strong coupling constant and parton distribution functions. A summary of the recent measurements by the CDF and D0 collaborations of the triple differential cross-section can be found in [15-98].

15.5.4.2 Di-jet invariant mass and angular distribution

As in the case of the inclusive jet cross-section, the di-jet invariant mass and angular distributions are used to search for new physics. The expected sensitivity to new physics is discussed in Chapter 21. The invariant mass of the di-jet system is calculated from the two leading jets found using a cone algorithm with a radius of 0.8, treating the jets as massless objects.

Figure 15-26 shows the cross-section for di-jet production (restricted to jet pseudorapidities of $|\eta| < 1$) as a function of the invariant mass of the di-jet system, as obtained from the PYTHIA calculation (using the CTEQ2L pdf), including the simulation of detector effects. As discussed before, the cross-section obtained after the detector simulation (using ATLFAST) has been corrected to the hadron level. The error bars indicate (for large masses) the achievable statistical accuracy for 300 fb^{-1}. Also shown for comparison is the result of a NLO calculation based on JETRAD [15-84], using the CTEQ4M parton distribution. The partonic cross-section has been corrected for hadronisation effects. In Figure 15-27 the ratio of the di-jet invariant mass cross-section from PYTHIA (corrected with a pseudo *K*-factor) to the one from this NLO calculation (including a hadronisation correction) is shown, together with the ratio of NLO calculations using different parton distribution functions and different values of the strong coupling constant

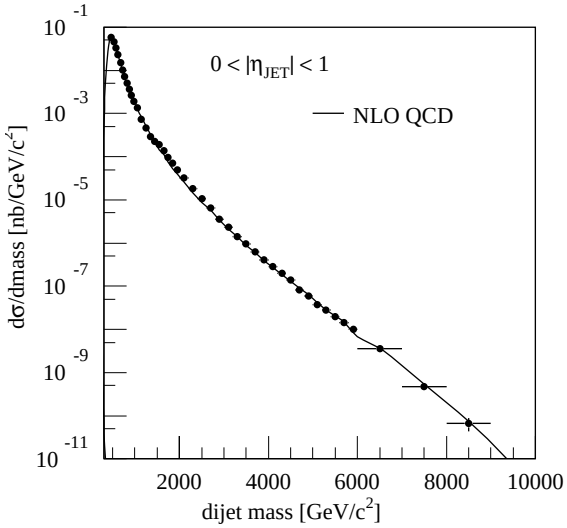

Figure 15-26 Di-jet invariant mass cross-section (at hadron level) for centrally produced jets ($|\eta| < 1$) obtained from a PYTHIA calculation (points) and from a NLO Monte Carlo calculation (solid line).

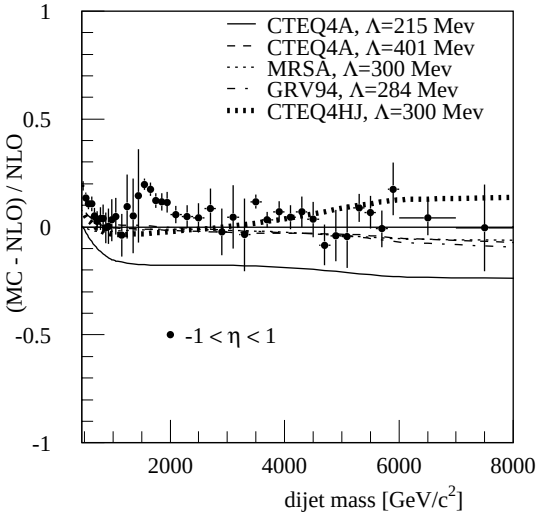

Figure 15-27 The ratio of the di-jet invariant mass cross-section from PYTHIA (including a pseudo *K*-factor) to the one at NLO from the JETRAD calculation (including a hadronisation correction) is shown as points. Also shown is the relative difference to the NLO calculation for a variation of Λ_{QCD} and for different pdf's (various curves).

(normalised to the CTEQ4M parton distribution and a value of Λ_{QCD} = 300 MeV). Clearly visible are the threshold effects close to the cut-offs on $\hat{p}_T$, where the statistical errors for masses smaller than about 4 TeV correspond to integrated luminosities much smaller than 300 fb^{-1}. Furthermore, this ratio is formed between a LO and a NLO calculation, which could produce additional distortions. The two largest effects are observed for a small value of Λ_{QCD} (CTEQ4A with 215 MeV) and for the CTEQ4HJ distribution, which allowed more freedom in the gluon distribution at large x to accommodate the excess of large E_T jets at the Tevatron. The errors bars shown indicate the statistical uncertainty at design luminosity only for invariant masses larger than 5 TeV, below the final statistical uncertainty will be smaller than the one shown. A measurement of the di-jet invariant mass distribution at the Tevatron by the D0 collaboration [15-99] showed good agreement of a NLO calculation with the data up to di-jet masses of 900 GeV. The data are at large masses slightly larger than the prediction based on the CTEQ3M distributions, here the CTEQ4HJ distributions give a better agreement.

15.5.4.3 Di-jet production at large angular separation

In a di-jet event, the two jets are expected to be balanced in E_T and to be back-to-back in azimuth. The configuration expected to dominate at leading order is central production of the di-jet system. It has been proposed [15-100] to study configurations where both jets are produced in the forward direction, being separated in rapidity by $\Delta = y_1 - y_2$. With increasing values of Δ, terms of the form $\log(s/Q^2)$ become more important in the partonic cross-section and can be resummed using the techniques of the BFKL approach. These terms appear only in certain regions of phase space and resummation should restore in this case the predictive power of the calculation. It is at present unclear, whether these regions can be probed by measurements at HERA or the Tevatron. The observation of the increase in the cross-section for large separation in rapidity (in fixed order QCD the partonic cross-section should remain constant) is difficult, since at larg-

er values of Δ the parton momentum fractions become large and the observable cross-section gets smaller. As observed at the Tevatron, additional radiation leads to a decorrelation in azimuth between the two jets [15-101][15-102], but in a manner correctly described by DGLAP kinematics.

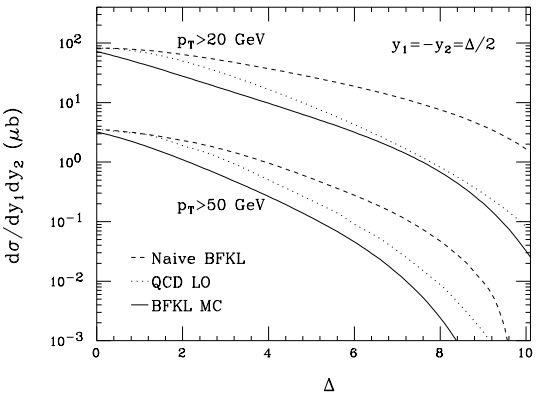

Figure 15-28 Differential cross-section for the production of two jets separated by Δ in rapidity. Three models are shown: a LO QCD calculation, a BFKL prediction and a BFKL Monte Carlo calculation (from [15-103]).

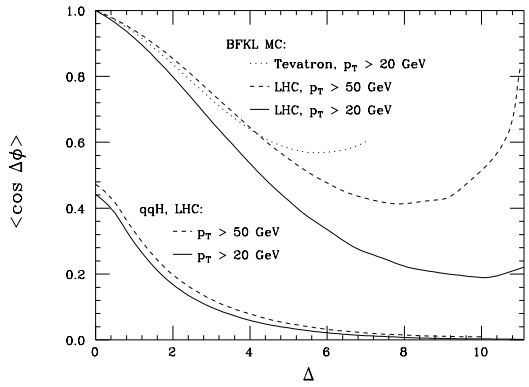

Figure 15-29 Azimuthal decorrelation in the production of two jets separated by Δ in rapidity. Shown are the results for the Tevatron and for the LHC from a BFKL Monte Carlo calculation (from [15-103]).

The cross-section for the production of two jets separated by a value of Δ in rapidity is shown in Figure 15-28 as a function of Δ. Three different calculations are shown for two cuts on the p_T of the most forward going jets: a LO QCD calculation, a 'naive' BFKL calculation (which contains only the resummation without taking into account kinematical constraints) and a realistic BFKL MC implementation [15-103], all using the CTEQ4L distribution. The decorrelation should be insensitive to the parton distribution functions. Figure 15-29 shows the expected azimuthal decorrelation in terms of <cos(π - Δφ)> (where Δφ is the angular separation between the two jets in azimuth) as a function of the separation Δ. The decorrelation increases (<cos(π - Δφ)> decreases) with increasing Δ. Shown are the predictions for Tevatron energies and for LHC energies, for the latter two values of the minimal jet transverse energy are used. Also shown is the expected decorrelation for the production of a heavy Higgs boson via gauge boson fusion in the process $qq \rightarrow qqH$, giving rise to two jets separated by Δ.

From the measurement of the D0 collaboration[15-104] (using jets with E_T > 20 GeV and a range of 0 < Δ < 6) it is known that a NLO calculation predicts too little decorrelation, whereas a 'naive' BFKL calculation predicts too much decorrelation at large separations. The HERWIG and PYTHIA models are able to describe the D0 data quite well.

The experimental challenge consists in selecting events where there is one jet on each side of the detector in the far forward region and trying to allow for as low transverse momentum of the jets as possible. The measurement requires in addition a good resolution in azimuthal angle to measure the decorrelation. The ATLAS forward calorimeter could provide a trigger on summed transverse energy in the region 3 < |η| < 5, as mentioned in [15-61] with a possible azimuthal division. The threshold on the jet energy will be restricted by the energy deposition in the forward calorimeter due to the underlying event and due to multiple interactions per bunch crossing. A LVL1 trigger would require a coincidence between energy depositions in the forward calorimeters at both sides of the detector, at the higher levels of the trigger a more refined jet selection could be applied, where the non-projective geometry of the calorimeter cells is taken

into account (see Section 9.1.4). In addition, the lateral size of the hadronic shower gets important. Without the use of the information of the forward calorimeter, the event selection would be restricted to values $\Delta < 6$. The fundamental selection for these events resembles the one for the study of colour singlet exchange at large momentum transfer, as discussed in Section 15.4.7. In the case of BFKL studies however, no requirements on the central rapidity region are made.

15.5.5 Multi-jet production

Possible measurements include the measurement of the cross-section for the production of *n* jets, along with a detailed analysis of the topological properties of the events. These can be used to constrain contributions from new physics, leading to final states with many jets. In the rest frame of the n-jet system, there are 4*n*-4 independent variables. These are typically divided into angular and fractional momentum variables, as well as invariant mass variables of combinations of different jets. The CDF collaboration has published a detailed study of multi-jet events (up to 6 jet events) and their topological properties [15-105]. The jet multiplicity distribution and the shape of the multi-jet mass and leading jet angular distribution shave been compared to a full leading order matrix element calculation [15-106][15-107] as well as to a leading order matrix element calculation (HERWIG) [15-13] for the $2 \rightarrow 2$ hard scattering, supplemented with parton showers. Both calculations agree well with the data. The inclusive p_T distribution is found to be able to discriminate between the two models, the HERWIG calculation overestimates the number of 3 and 4 jets at intermediate p_T. Multi-jet production can also be used to study effects of colour coherence, as discussed later.

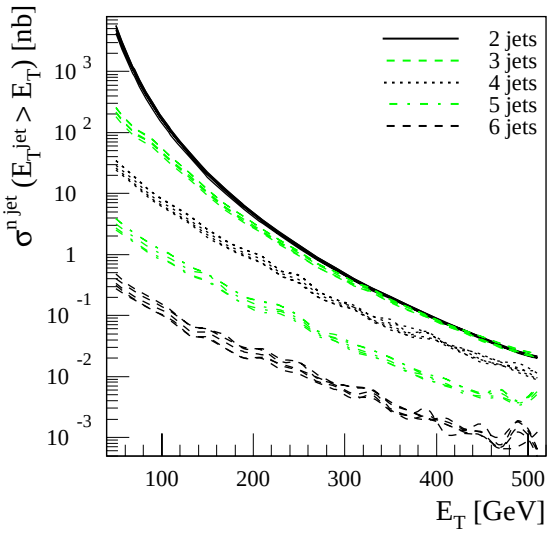

Figure 15-30 Cross-section for the exclusive production of *n* jets (*n* = 2,3,4,5,6 and $|\eta| < 3.2$) as a function of the minimum jet transverse energy at parton level for different parton distributions (CTEQ2L, CTEQ4L, CTEQ4HJ, MRSA and GRV94) from a LO calculation.

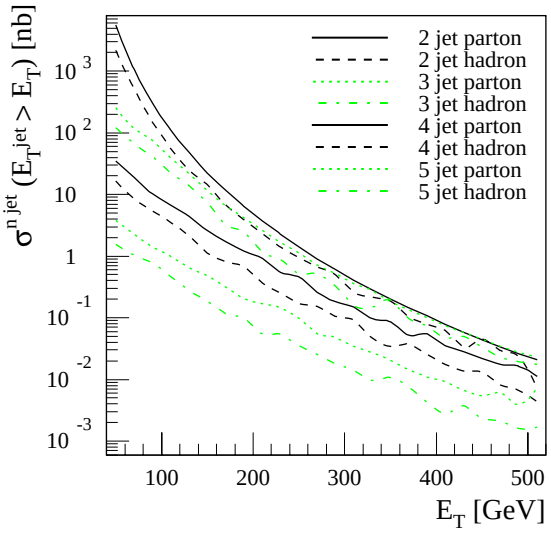

Figure 15-31 Cross-section for the exclusive production of *n* jets (*n* = 2,3,4,5 and $|\eta| < 3.2$) as a function of the minimum transverse energy of each jet comparing parton to hadron level. The hadron level cross-section has parton showers and hadronisation added to the LO result.

A thorough understanding of the properties and cross-sections for multi-jet production is important for several other physics studies, *e.g.* $t\bar{t}$ production with hadronic final states, the search for R-parity violating SUSY (where around 8 - 12 jets are expected for a signal) and for Higgs production in association with heavy quark pair ($b\bar{b}$ or $t\bar{t}$), where the Higgs decays to $b\bar{b}$. As mentioned previously in Section 15.5.2.6, the ratio of the cross-section for the production of 3 jets to the one of 2 jets might be used to extract the strong coupling constant.

The cross-sections for the production of n jets (n = 2,3,4,5,6) are shown in Figure 15-30 as a function of the jet transverse energy. They have been obtained from a leading order calculation[15-106] and [15-107]. In Figure 15-30 the differential cross-section for the production of n jets at the parton level is shown as a function of the transverse energy of the jets. Several parton distributions have been used: CTEQ2L, CTEQ4L, CTEQ4HJ, MRSA and GRV94. In the calculation, a minimal angular separation of 40 degrees between two partons was required. The experimental selection can be found in the trigger menu in Section 11.7. Multi-jet triggers with smaller thresholds will be available, although they will be subjected to a pre-scaling. A comparison between the cross-section at parton level and the one at hadron level is shown in Figure 15-31. The multi-jet cross-section at hadron level was obtained by adding parton showers to the partons from the NJETS calculation and hadronising the partonic system. Jets were defined using a cone algorithm with a radius of R = 0.4. The hadron level cross-sections are slightly smaller than the parton level ones for all jet multiplicities shown (n = 2,3,4,5).

Effects of colour coherence are expected to lead to an inhibition of soft gluon radiation (for example observed in the ‘string’ effect [15-108] in e^+e^- annihilation). The measurement of such effects in a hadron-hadron collider environment is difficult due to the many colour flow patterns present. The CDF collaboration tried to avoid these difficulties by selecting events where the leading jet has a large enough energy, so that the soft radiation becomes hard enough to form secondary jets. The measurement [15-109] of kinematical correlations between the second and third most energetic jet indicated the contribution of the interference between initial and final state gluon emission from the colour connected partons. A comparable investigation by D0 [15-110] arrived at similar conclusions.

15.5.6 Double parton scattering

Given the large density of partons with small longitudinal momenta in the proton, there exists the possibility of two (or more) hard interactions taking place in a high energy collision. The cross-section for double parton scattering can be expressed in terms of a two-parton distribution function $D(x,x',b)$ [15-111] depending on two momentum fractions and a transverse distance scale. In the case of no correlation between the partons, this function factorises and the double parton scattering cross-section σ_D can be written in terms of the single parton scattering cross-section σ_S and an effective cross-section σ_{eff}. This effective cross-section contains information about the spatial distribution of partons in the proton. Its value will increase with the uniformity of the spatial distribution and will decrease with increasing concentration of ‘clumpy’ regions containing a high density of partons. In the latter case the probability for a double parton scattering is larger, as the first scatter selected a region of high parton density. The ultimate goal will be to derive from measurements not only the occurrence of multiple parton scattering, but to extract parton densities containing the information about the correlation between several partons.

The occurrence of double parton scattering has been measured by the CDF collaboration, using events with exactly three jets and a photon (or a π^0) [15-112]. Requiring a transverse energy of the photon of more than 16 GeV and of the second and third jet of 5 to 7 GeV, an effective cross-section of $\sigma_{eff} = 14.5 \pm 1.7^{+1.7}_{-2.3}$ mb was extracted. No dependence of the process on the value of x was observed.

At the LHC the experimental challenge is to select events with mini-jets, *i.e.* jets which do not have a very large transverse energy. Besides the actual reconstruction of such jets the triggering of these events has to be studied in more detail. Based on a minimum-bias trigger for the first level of the ATLAS trigger, the higher levels, which have access to the full granularity of the sub-detectors, could try to enhance the signal by reconstructing jets with low transverse energy. More studies have to be performed to assess the minimal transverse energies for the jet reconstruction. In the context of low p_T jet tagging at low luminosity (more details can be found in Section 9.1.4) a minimal value of about 15 GeV was studied.

15.6 Photon physics

15.6.1 Overview

The detection of photons at a hadron collider is a challenging task due to the large background from jet production, where fluctuations can mimic the signature of a photon. ATLAS with its fine granularity calorimeters extending to $|\eta| < 2.5$ offers the possibility for a large rejection factor against this background (see Section 7.6). The advantage of photon measurements is the better energy determination in comparison to jet measurements. In addition the definition of a jet leads to ambiguities. Direct photon measurements can provide important constraints on parton distributions, especially on the gluon distribution in the proton. In case of photons, however, the experimental background due to jets containing a leading π^0 has to be understood well. The signal-to-background ratio can be improved significantly by requiring the photon candidate to be isolated, *i.e.* there should be no significant hadronic activity in a cone around the photon direction. Searches for the Higgs boson in the decay to two photons require a good understanding of the irreducible background from photon pair production.

In this section, the measurement of the inclusive prompt photon production (Section 15.6.2) and the production of photon pairs (Section 15.6.3) will be discussed. Additional topics include the production of photons with an associated final state property, like jets (Section 15.6.4) or open charm (Section 15.6.5).

15.6.2 Inclusive photon production

The production of direct photons has two main contributions, the QCD Compton process ($qg \rightarrow q\gamma$) and the annihilation graph ($q\bar{q} \rightarrow g\gamma$). In the case of Tevatron energies and small to moderate transverse momentum of the photon, the Compton process dominates. Also at the LHC the Compton process dominates in most of the kinematical region. Only this process provides a sensitivity to the gluon distribution. A calculation of direct photon production including next-to-leading-logarithms [15-113] starts from the two lowest order processes listed above (a similar calculation can be found in [15-114]). The calculation is based on a Monte-Carlo approach, allowing for the inclusion of cuts. Calculations at next-to-leading order include the one-

loop corrections to the $2 \rightarrow 2$ process and the tree level calculation of the $2 \rightarrow 3$ processes. The bremsstrahlung process corresponds to the emission of a photon from a final state parton. For large angles, this contribution is included in the $2 \rightarrow 3$ diagrams, for small angles only a phenomenological treatment via a non-perturbative fragmentation function is available. In [15-115] the calculation for isolated prompt photon production is shown, including studies on the uncertainties due to the scale dependence, the isolation criteria and the fragmentation contribution. The differences between the data at low photon transverse momenta at the Tevatron and the NLO expectation (which is lower than the data) can possibly be explained by the effects of initial state gluon radiation.

The usual measurement of prompt photon production requires in the experimental selection an isolated photon, by demanding no significant hadronic energy deposition inside an isolation cone around the photon direction. This definition is not simply transferrable to a perturbative QCD calculation, as the cancellation of infrared divergences [15-116] must not be spoilt, which would happen if a sharp isolation of the photon from other partons is made. Not applying a sharp isolation however allows contributions from photon fragmentation and from jet background to appear. Two approaches have been suggested: a cone based approach, where only a small amount of hadronic energy in a cone around the photon direction is allowed and the 'democratic' approach, where the photon is treated as a parton in performing a jet clustering. Then a cut on the hadronic energy of the jet containing the photon is applied. In the case of photon and associated jet production, a procedure has been suggested which is infrared safe to all orders and minimises the fragmentation contribution[15-116]. The cone approach is extended by requiring an upper limit on the hadronic energy in a cone around the photon for all cone sizes δ smaller than a fixed value δ_0. The upper limit on the hadronic energy E_{max} depends on the cone size: $E_{max} = f(\delta)$, where the function f goes to 0 when the size δ approaches 0. The jet finding is performed on all partons, but only those jets which are outside the isolation cone are accepted. This method allows hadrons to be close to the photon, as long as their energies get smaller as they get closer.

The primary background to direct photon production is due to jet fragmentation into a leading π^0 or η. The imposition of an isolation cut greatly discriminates against this jet fragmentation background, while having little effect on the prompt photon signal. Studies at the Tevatron (*e.g.* by CDF for $p_T^{\gamma} > 12$ GeV) have shown that after an isolation cut (less than 2 GeV in a cone of radius 0.7) the signal fraction (of the direct photon candidates) increases by up to several orders of magnitude (to ~20% at low p_T, approaching 100% at high p_T). For larger transverse momenta, the EM showers generated in the calorimeter overlap significantly and an analysis of the shower shape is necessary to allow a statistical subtraction of this background source. Another estimate of the background can be obtained from the measured converted photons in the tracking detectors.

In the kinematic range of the photon transverse momentum between 100 and 500 GeV the expected ratio between the inclusive direct photon cross-section (at NLO for $|\eta| < 0.7$, as shown in Figure 15-32) and the inclusive jet cross-section (at NLO [15-84] for $|\eta| < 0.7$) is about 1.5×10^{-3}. For photon transverse energies between 40 and 100 GeV a rejection of about 3000 against jets is achieved. More details on the separation between photons and jets can be found in Section 7.6.

The minimal parton momentum x_{min} is determined by the transverse energy threshold E_T^{min} and the maximal pseudorapidity η_{max} of the photon via the relation $x_{min} = 2(E_{Tmin}/\sqrt{s})e^{-\eta_{max}}$, the maximal momentum fraction x_{max} via $x_{max} = 2(E_{Tmax}/\sqrt{s})e^{\eta_{max}}$. The selection at ATLAS will be based on a trigger demanding an isolated photon of transverse energy larger than 40 GeV (low luminosity) or 60 GeV (high luminosity) within $|\eta| < 2.5$. This gives a value of

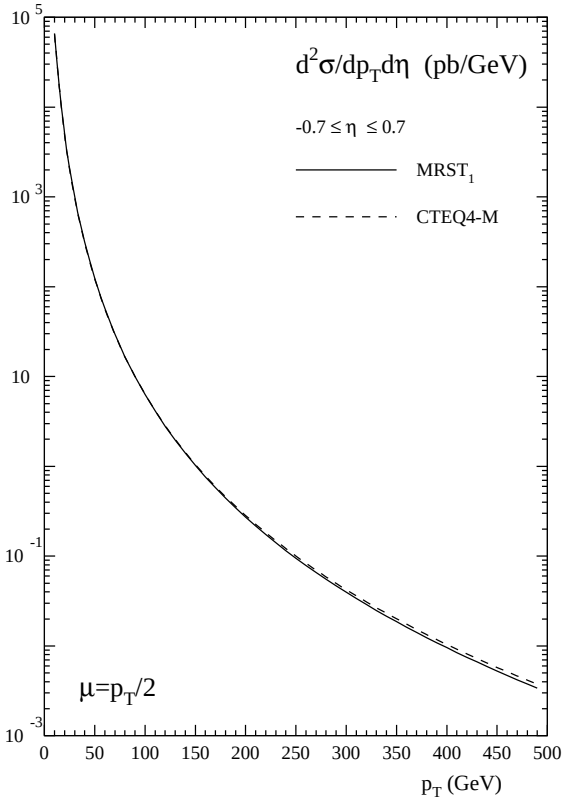

Figure 15-32 Inclusive direct photon cross-section (for central photon production $|\eta| < 0.7$) at next-to-leading order as a function of p_T (from [15-117]) for two pdf's.

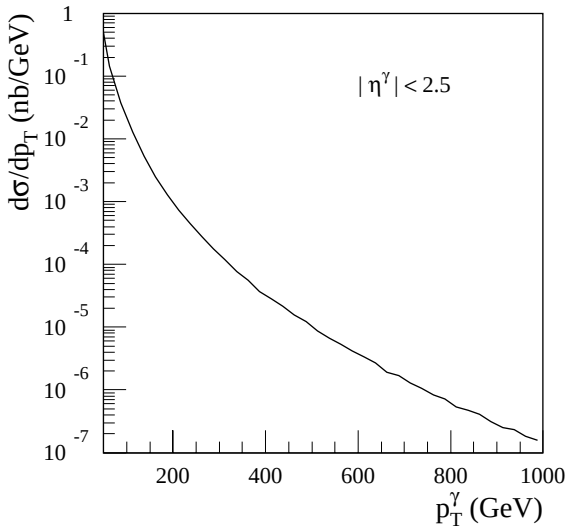

Figure 15-33 Inclusive direct photon cross-section at leading order (from PYTHIA, including the ATLFAST detector simulation) as a function of p_T for the CTEQ3L pdf.

$x_{min} = 5 \times 10^{-4}$, lower values could be reached by using lower thresholds, which will however be subjected to a prescaling. For a photon transverse energy of 500 GeV, a value of $x_{max} = 0.2$ is obtained. In Figure 15-32 the cross-section for prompt isolated photon production is shown as a function of the transverse momentum of the photon, as obtained from a next-to-leading order calculation [15-117] for central photon production ($|\eta| < 0.7$). Figure 15-33 shows the same cross-section, as obtained from a leading order calculation including a detector simulation (using ATLFAST), using the CTEQ3L parton distribution set. The photon was required to have a transverse momentum of at least 40 GeV and be within $|\eta| < 2.5$. Further an isolation criteria was applied. A comparison of the NLO and the LO calculation gives a *K*-factor of about 1.5, however it has to be taken into account that the NLO calculation is restricted to the central pseudorapidity region ($|\eta| < 0.7$), whereas the leading order calculation reaches up to $|\eta| < 2.5$.

15.6.3 Photon pair production

Effects of soft gluon emission can be studied directly by measuring the production of pairs of photons. The transverse momentum of the photon pair and the azimuthal angular difference between the two photons are sensitive to these emissions.

As in the case of inclusive photon production, the main experimental challenge is to reduce the background of fake photon pairs (*i.e.* processes producing two jets or a jet and a photon, where the jet(s) lead to one(two) fake photon(s)). The selection will be based on a trigger requiring two isolated photon candidates within $|\eta| < 2.5$. The threshold on the transverse energy will be 20 GeV for each photon (for low and high luminosity running conditions).

A calculation of the di-photon production at next-to-leading order including the resummation of soft gluon emission is presented in [15-118]. The resummation is performed on initial state gluon emission for $q\bar{q}$, qg and gg initial states, treating the di-photon system in a similar manner as a Drell-Yan virtual photon. The production of one photon via a fragmentation process is taken into account, the NLO contributions for the $q\bar{q}$ and qg initial states are determined exactly and for the gg box diagram NLO contributions are included in an approximation.

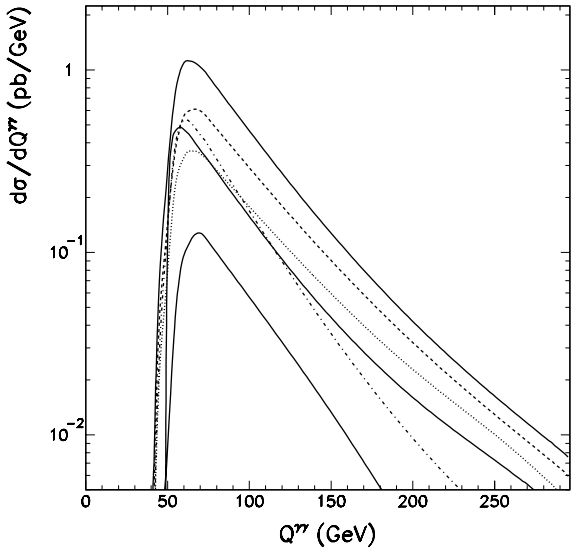

Figure 15-34 Cross-section for photon pair production from [15-119] as a function of the invariant mass $Q^{\gamma\gamma}$ of the pair. The upmost solid curve shows the total NLO prediction, whereas the LO contribution is represented by the middle solid curve. The other curves are explained in the text.

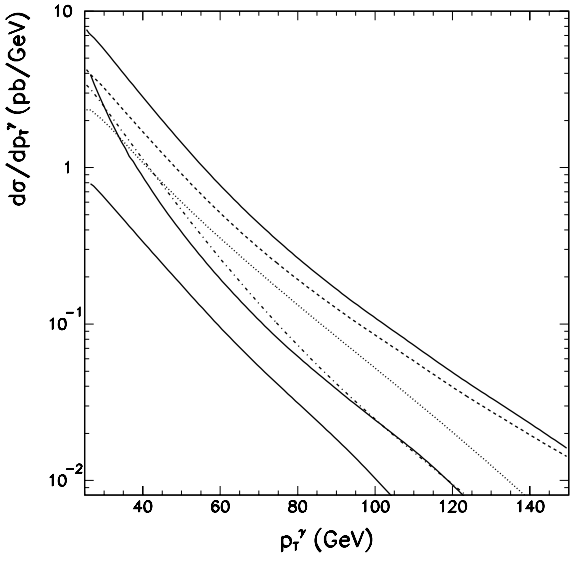

Figure 15-35 Cross-section for photon pair production from [15-119] as a function of the photon transverse momentum p_T^{γ}. The upmost solid curve shows the total NLO prediction, whereas the LO contribution is represented by the middle solid curve. The other curves are explained in the text.

Figure 15-34 shows the cross-section for di-photon production as a function of the invariant mass of the di-photon system. This calculation [15-119] includes the NLO contributions and the resummation of soft gluon emission. The following cuts have been applied to the photons: $p_T > 25$ GeV, $|\eta| < 2.5$, $\Delta R(\gamma,\gamma) > 0.4$ and $p_T^1/(p_T^1 + p_T^2) < 0.7$, where p_T^1 is the transverse momentum of the leading photon (this cut is not used in the analysis of the Higgs decay to two photons, as described in Section 19.2.2). The upmost solid line corresponds to the total cross-section, the dashed line represents the resummed part for $q\bar{q} + gg \rightarrow \gamma\gamma X$. The part of the resummed process due to the $q\bar{q}$ initial state is shown as a dotted line, the one due to the gg initial state as a dash-dotted line. The lowest solid curve shows the fragmentation contribution and the leading order contribution is indicated by the middle solid curve. The importance of the gg initial state for lower di-photon masses should be noted.

A total cross-section of about 61 pb is obtained (using the CTEQ4M distribution), where the leading order part amounts to about 22 pb (CTEQ4L). The total cross-section splits into the contributions from the three initial states as follows: 20.5 pb for $q\bar{q}$, 23.9 pb for gg and 16.6 pb for qg, where the latter includes a fragmentation contribution of 6.8 pb.The understanding of this distribution (representing the irreducible background contribution) is important in estimating the reach in the search for a light Higgs boson, which decays to two photons, or in setting limits on the Higgs production cross-section. The *K*-factor has a value of about two, being rather independent of the photon pair mass.

In Figure 15-35 the distribution of the transverse momentum of the photons is shown, where the labelling of the curves is described above. The comparison of the LO and the NLO result shows a large *K*-factor, which increases with the transverse momentum of the photon up to values of about five.

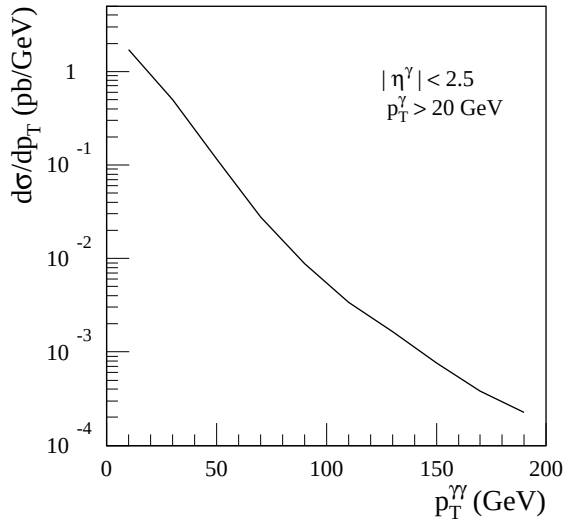

Figure 15-36 Cross-section for photon pair production from a leading order calculation (PYTHIA with ATLFAST) as a function of the transverse momentum $p_T^{\gamma\gamma}$ of the pair.

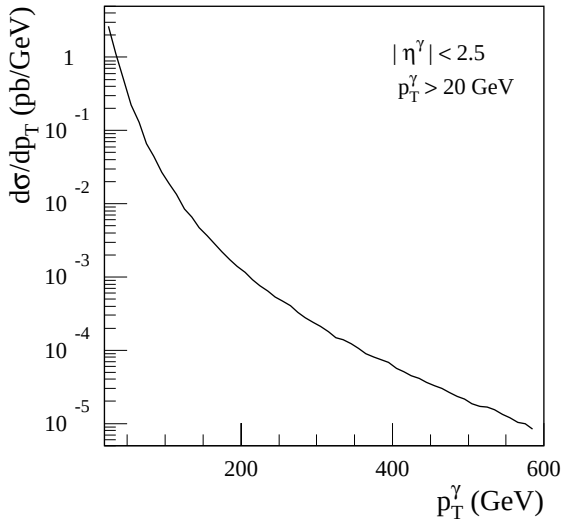

Figure 15-37 Cross-section for photon pair production from a leading order calculation (PYTHIA with ATLFAST) as a function of the transverse momentum p_T^{γ} of the photons.

In Figure 15-38 the cross-section for photon pair production is shown as a function of the invariant mass of the photon pair for masses up to 1 TeV. This cross-section was obtained from a leading order calculation using PYTHIA, including a simulation of the detector response (using ATLFAST). Photons were required to have at least 20 GeV transverse energy, to be isolated and to be restricted to pseudorapidities of $|\eta| < 2.5$. The CTEQ3L parton distributions were used. For the same cuts, Figure 15-36 shows the cross-section as a function of the transverse momentum of the photon pair, indicating that large transverse momenta can be studied with reasonable statistics. In Figure 15-37 the cross-section is shown as a function of the transverse momentum of a photon.

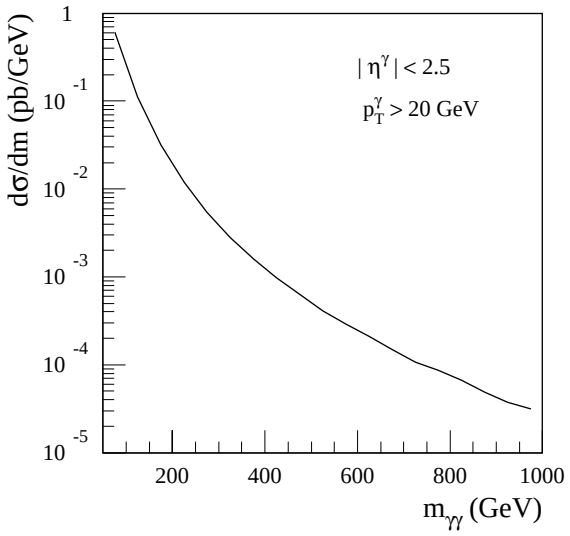

Figure 15-38 Cross-section for photon pair production from a leading order calculation (PYTHIA with ATLFAST) as a function of the invariant mass $m_{\gamma\gamma}$ of the pair.

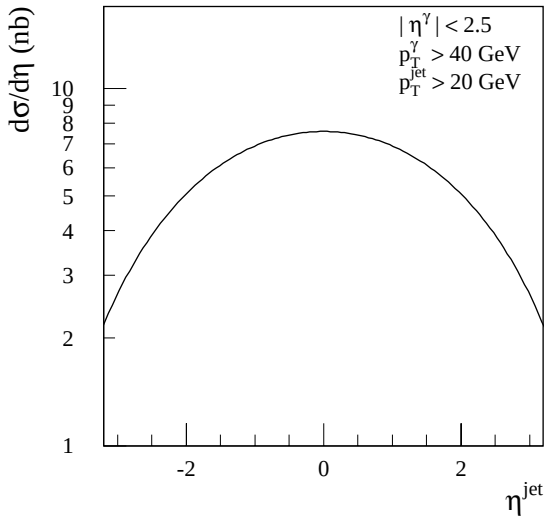

Figure 15-39 Cross-section for direct photon + jet production (PYTHIA with ATLFAST) as a function of the pseudorapidity η^{jet} of the jet, as obtained from a leading order calculation.

15.6.4 Photon + jet production

The measurement of an associated jet for photon production allows better constraints of the parton distribution functions, since both parton momenta of the hard scattering can then be reconstructed. When both the jet and the photon are centrally produced, the x values of the partons are of similar magnitude. The angular distribution is given by the quark propagator, similar to the case of W + jet production. A leading order calculation for photon + n jet production (n = 1,2,3) is available [15-120], the next-to-leading order corrections have been calculated [15-121]. In Figure 15-39 the cross-section for the production of a direct photon and a jet is shown as a function of the pseudorapidity of the jet. The figure has been obtained from a PYTHIA calculation, based on the CTEQ2L parton distributions and taking into account the ATLAS detector response. For the photon a minimal transverse energy of 40 GeV and a limit of $|\eta| < 2.5$ were required, the jet had to have a transverse energy of at least 20 GeV.

The occurrence of double parton scattering represents a source of background for this process. It can be studied by selecting events with a photon and three jets. For two hard scattering processes, the angular difference between the system of photon + leading jet and the second jet is expected to be flat. For a p_T cut of about 40 GeV on the photon transverse momentum, this effect should give a minimal contribution only.

A CDF measurement of the triple differential cross-section for photon + jet production [15-122] (as a function of p_T, η_γ and η_{jet}) allows to cover different ranges in parton momentum x by varying the jet pseudorapidity η_{jet}. Within the errors, this measurement does not discriminate between different parton distribution functions, where the highest sensitivity is expected at large jet pseudorapidities.

In order to quantify the contribution of the bremsstrahlung process ($qg \to qg\gamma$) to the direct photon production, relative to the Compton and the annihilation graph, the CDF collaboration measured the production of photons in association with 2 jets [15-123]. The two dominant sources of systematic uncertainty are the knowledge of the energy scale and the contribution from double hard scattering background. The data are best described with a 50% contribution of the Bremsstrahlung process to the isolated photon cross-section.

A further use of the photon + jet final state is the deduction of information on the $\bar{u}$ content of the proton [15-124]. The two dominant contributions to the production of a high p_T photon and an associated jet are $ug \to u\gamma$ and $u\bar{u} \to g\gamma$. These two processes are enhanced relative to the *d* and *s* quark contribution due to the electric charge of the *u* quarks and the smaller amount of *d* and *s* quarks in the proton.

15.6.5 Photon + charm and photon + beauty production

The production of charm in association with a photon can be used to constrain the charm content of the proton. Leading order calculations of prompt photon and charm production were carried out using two approaches [15-125]. The first approach included Compton scattering off a charm sea quark $gc \to \gamma c$, taking into account also the effect of gluon splitting $g \to c\bar{c}$ and of photons from fragmentation. The second approach is based on a massive charm quark at low energies, including the two following processes: $gg \to \gamma c\bar{c}$ and $q\bar{q} \to \gamma c\bar{c}$ as well as the fragmentation contribution. A non-negligible contribution to the inclusive prompt photon production is expected. For Tevatron energies, both approaches give similar results, indicating that the observation of prompt photon + charm production not necessarily implies a non-vanishing charm sea quark distribution. An analytical next-to-leading order calculation [15-126] indicates a *K*-factor of about 1.5 to 1.9 for Tevatron energies, which decreases with increasing photon transverse momentum. The calculation includes the one loop corrections to $gc \to \gamma c$, the leading order fragmentation graphs and the NLO contributions, like $gg \to \gamma c\bar{c}$, $gc \to \gamma gc$ and so on, which give rise to the large *K*-factor. Differential distributions are available and can be used to test correlations in the matrix elements. The dominant contribution is found to be due to the scattering off a charm sea quark. An implementation of this calculation by combining the analytic and the Monte-Carlo approach is available [15-127] and allows an implementation of experimental cuts.

The tagging of charm production can be done by measuring the associated production of a muon (or an electron) with a photon (inclusive detection of semi-leptonic decays) or by exclusive decay reconstruction (*e.g.* the non-leptonic decay of a D^{*+-} meson) together with a photon in the final state. Measurements done by CDF at the Tevatron for photon + muon production [15-128] and for photon + D^* production [15-129] show an excess of the measured cross-section (about a factor of 2) relative to the prediction of a PYTHIA calculation, the data are however in agreement with the NLO calculation.

The associated production of a photon together with a *b* quark contributes to the γ + charm production. A measurement of this contribution could be based on a selection of a photon together with the tagging of beauty production, as discussed in Section 15.8.3. In comparison to the case of inclusive photon production, in this case lower transverse momentum thresholds for the photon candidate should be possible.

15.7 Drell-Yan physics and gauge-boson production

15.7.1 Overview

The production of Drell-Yan pairs proceeds by the annihilation of quark and anti-quarks via an intermediate vector boson (γ^*/Z or W). This probes the proton structure at a scale Q^2 equal to the mass squared of the lepton pair. In proton-proton collisions, the production of lepton pairs proceeds via γ^*/Z bosons and starts from a combination of a valence quark and a sea quark (or a quark and an anti-quark from the sea) of the same flavour (*e.g.* $u\bar{u}$, $d\bar{d}$, ...). In the case of W production, a valence quark and a sea quark (or a quark and an anti-quark from the sea) of different flavour annihilate. QCD effects enter the cross-section for Drell-Yan production only in the initial state and thus make the predictions less uncertain.

Given the different average momentum fraction carried by valence and sea quarks, in most cases an asymmetric configuration will be preferred, where one momentum fraction is small, and the other large. At leading order, the rapidity y of the lepton pair is related to the momentum fractions $x_{1,2}$ via: $y = 0.5 \ln(x_1/x_2)$ and the invariant mass of the pair is given by $M^2 = x_1 x_2 s$. For a lower bound of 14 GeV on the mass M of the lepton pair, the product of the parton momentum fraction $x_1 x_2$ has to be larger than 10^{-6}. Assuming that the reconstruction of Drell-Yan pairs is done up to rapidities of 2.5, the maximum ratio possible between the two parton momenta is of the order of 150.

In this section, the production of Drell-Yan pairs over the full range of the invariant mass of the lepton pair will be discussed (Section 15.7.2), followed by the presentation of W boson production (Section 15.7.3). Next a discussion of Z boson production is presented (Section 15.7.4) and finally the pair production of vector bosons is described (Section 15.7.5).

15.7.2 Drell-Yan production

15.7.2.1 Di-lepton mass spectrum

The measurement of the lepton pair properties (lepton rapidities and invariant mass of the pair) allows the reconstruction of the parton momenta and thus can give constraints on the parton distribution for quarks. The two leptons are expected to be well separated from jets and other particles. A selection will start from trigger on di-leptons, where details on the thresholds and cuts can be found in Section 11.7. For the lepton pair production, a resummation of soft gluon emission contributions exists [15-130].

Besides the background from cosmic rays for the case of muon pairs, two classes of background sources can be distinguished: the misidentification of leptons and leptons originating from heavy quark decays. In both cases, the main source is the production of QCD jets and thus these (fake) leptons are expected not to be isolated, as are those from Drell-Yan production. Furthermore, the leptons from Drell-Yan production are of opposite charge. The background from misidentification can be determined by studying the same charge lepton pairs. Background of opposite charge lepton pairs from heavy quark decays ($b\bar{b}$ and $t\bar{t}$ production) can be estimated using $e\mu$ events. Measurements of the Drell-Yan pair production have been performed by CDF [15-131] and D0 [15-132].

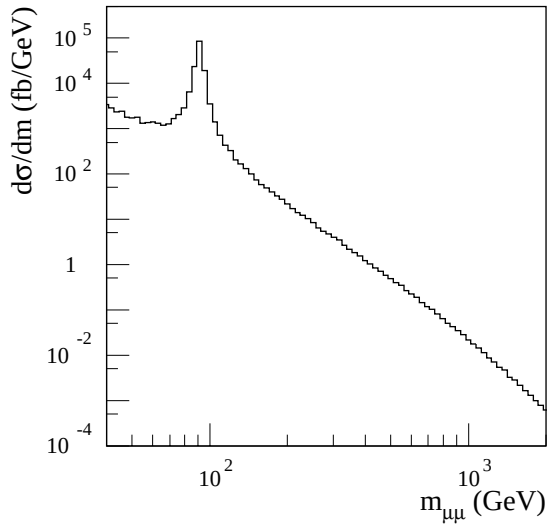

Figure 15-40 Cross-section for Drell-Yan muon pairs as a function of the invariant mass $m_{\mu\mu}$ of the muon pair from a leading order calculation (PYTHIA with ATLFAST) for the following cuts: $p_T^{\mu} > 6$ GeV and $|\eta_{\mu}| < 2.5$.

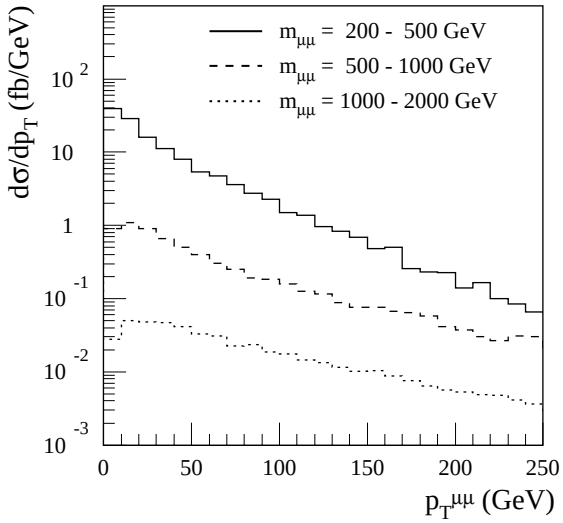

Figure 15-41 Distribution of the transverse momentum $p_T^{\mu\mu}$ of the lepton pair produced in a Drell-Yan process from a leading order calculation (PYTHIA with ATLFAST) for three ranges of $m_{\mu\mu}$. The following cuts have been applied: $p_T^{\mu} > 6$ GeV and $|\eta_{\mu}| < 2.5$.

Figure 15-40 shows the expected cross-section for Drell-Yan production as a function of the invariant mass of the Drell-Yan pair, as obtained from PYTHIA using the CTEQ2L parton distributions [15-15]. Clearly visible is the resonance contribution due to production of the Z boson, which will be discussed in more detail in Section 15.7.4.

15.7.2.2 p_T distribution of lepton pair

In Figure 15-41 the distribution of the transverse momentum of the muon pair produced via the Drell-Yan process is shown for three different ranges of the invariant mass of the two muons: 200-500, 500-1000 and 1000-2000 GeV. The prediction is based on the same cuts as in the previous section. The figure shows that with the LHC statistics a significant number of high mass Drell-Yan pairs will be produced with transverse momenta larger than 100 GeV.

The angular distribution of the leptons (and the lepton pair) produced in a Drell-Yan process should be sensitive to effects of non-perturbative QCD. For these angular observables, next-to-leading order calculations exist [15-133]. As shown by the CDF collaboration[15-134], the forward-backward asymmetry of the lepton pair produced can be used to verify the expected contribution due to the γ^* / Z interference for lepton pair masses significantly larger than the Z pole. Furthermore, the value of the forward-backward asymmetry could be modified in the presence of heavy neutral gauge bosons.

15.7.3 *W* production

15.7.3.1 Cross-section

At the LHC the cross-section for the production of the W^+ is larger than the one for the production of W^- bosons. The contribution from $c\bar{s}$ (and $s\bar{c}$) initial states amounts to 10% at LHC energies (about 2% for the Tevatron). The latter contributions mainly contribute to the central production of W's, whereas forward W production is mostly due to $u\bar{d}$ ($d\bar{u}$) states. The product $x_1 \cdot x_2$ of the parton momenta is fixed to a value of about 3×10^{-5} at leading order.

The experimental selection will start from a trigger on a single lepton (electron or muon) within the pseudorapidity range of $|\eta| < 2.4$ for muons and $|\eta| < 2.5$ for electrons, respectively. Details on the thresholds for these triggers can be found in Section 11.7.3, the selection will then require in addition missing transverse energy (as discussed in more detail in Section 16.1.2). Due to the large statistics expected for the LHC, a restriction to the clean leptonic decay channels (involving an electron or a muon) is possible.

The dominant sources of background are the decay $W \to \tau\nu$ for the electron and the muon channel, and the decay $Z \to \mu\mu$ (where one of the muons is outside the acceptance) for the muon channel. Due to the excellent electron-jet separation (as described in Section 7.4, where it has been shown that jet rejection factors of the order of 10^5 can be achieved, while having an efficiency of about 70% for electrons from W (and Z) decays) the background from QCD multi-jet events is negligible. More details on these and other background sources can be found in Section 16.1.3.7. The efficiency for the lepton detection can be derived from experimental data using the copious production of Z bosons and their decay to two leptons. The dominant systematic uncertainty for the cross-section measurement is expected due to the determination of the absolute luminosity.

15.7.3.2 Rapidity distribution

In contrast to the case of proton anti-proton collisions (as in the case of Tevatron), at the LHC there is no rapidity asymmetry for the produced W's. However, the shape of the rapidity distributions (being symmetric with respect to $\eta = 0$) is different for W^+ and W^-, where the total cross-section is larger for W^+ than for W^-. The difference in the shape of the rapidity distribution should survive in the detectable decay lepton. It is a direct consequence of the parton distribution functions responsible for W^+ ($u\bar{d}$) and W^- ($d\bar{u}$) production.

In Figure 15-42 the expected shape of the rapidity distribution for W^+ and W^- production is shown. The cross-section times leptonic branching ratio has been obtained from PYTHIA using the CTEQ2L parton distributions, without applying cuts on the decay lepton. In Figure 15-43 the corresponding distribution for the decay lepton is shown, where for the lepton (electron or muon), a minimal transverse momentum of 20 GeV and $|\eta| < 2.5$ were required. Furthermore a missing transverse energy of at least 20 GeV was demanded. In both figures the different shapes of the W^+ and the W^- are visible; the W^+ goes further out in rapidity and has a maximum at $|y| = 3$. The central region ($|y| = 0$) corresponds to a symmetric configuration of the parton momenta ($x_{1,2} \sim 0.005$), whereas at $|y| = 2.5$ an asymmetric configuration can be found ($x_1 \sim 0.1$, $x_2 \sim 0.0007$). The precise measurement of these rapidity distributions can be used to constrain the u and $\bar{d}$ (resp. d and $\bar{u}$) distributions.

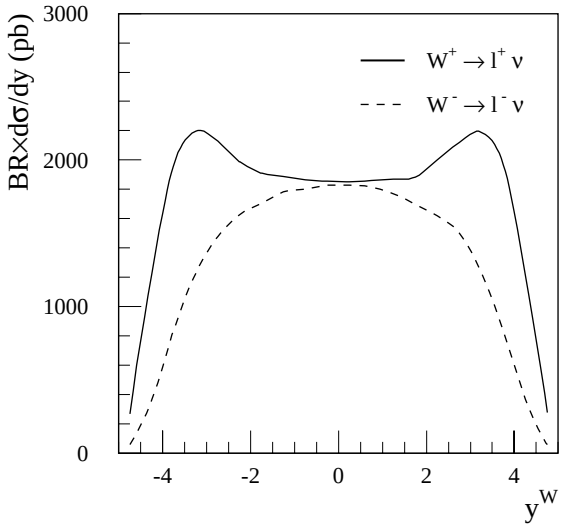

Figure 15-42 Differential cross-section for W^+ and W^- production as a function of the vector boson rapidity y^W from a leading order calculation (PYTHIA).

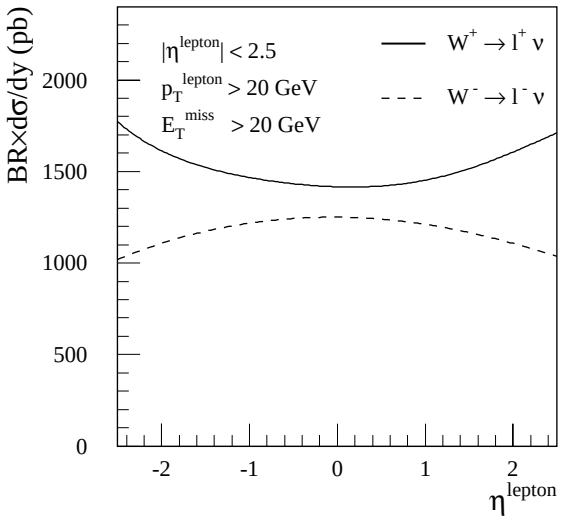

Figure 15-43 Differential cross-section for W^+ and W^- production as a function of the pseudorapidity η^{lepton} of the decay lepton of the W (PYTHIA and ATLFAST).

15.7.3.3 p_T distribution

The transverse momentum of the boson is due to associated production of quarks or gluons. A detailed understanding of the transverse momentum is important for a precise measurement of the W boson mass at hadron colliders. In the case of large q_T (the W transverse momentum) where mostly a single high p_T parton is radiated, an $O(\alpha_s^2)$ calculation exists. This is a one scale problem ($q_T \sim M_W$), where fixed order calculations are reliable. In the case of low q_T, multiple soft gluons can be emitted, leading to the appearance of large logarithms $\log(M_W^2/q_T^2)$. This two scale problem (q_T and M_W) can be solved by a resummation of these logarithmic terms. To provide a scheme for all q_T, a matching procedure has to be devised. These effects do also apply for the production of Z boson, as described in Section 15.7.4.2.

Data from the Tevatron on the W boson p_T show that a fixed order NLO calculation does not reproduce the measured spectrum. The comparison of data from D0 [15-135] to the prediction of Ref. [15-136], where a next-to-leading order calculation has been matched with the resummed calculation (introducing parameters for non-perturbative effects) shows consistency with the data. A second calculation [15-137] performs the matching at a scale where the W transverse momentum is close to the W mass. Using the data from D0, these two cannot be distinguished [15-138]. The non-perturbative part of the prediction has been obtained from a fit to the transverse momentum distribution of Z bosons, at small p_T the two calculations give different predictions. Even more uncertain is whether these non-perturbative parameters can be used universally, *e.g.* when going to LHC energies [15-139].

If the resummation of these logarithms is performed in the q_T space (where q_T is the transverse momentum of the vector boson) [15-140], a unified description of the production of vector bosons both for small and for large q_T is obtained without the need for a matching procedure. In Figure 15-44 the cross-section for inclusive W production is shown as a function of the transverse momentum of the W boson, as obtained from the calculation by Ellis and Veseli [15-140], using the MRS-R1 parton distributions [15-141]. The non-perturbative parameters (for the form factor) were set to the following values: $q_T^{lim} = 4$ GeV and $\tilde{a} = 0.1$ GeV^{-2}. They control the inter-

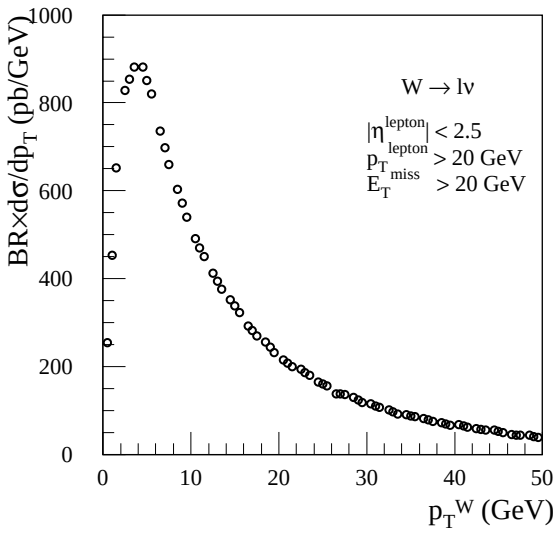

Figure 15-44 Differential cross-section for *W* production (with decay to either an electron or a muon) as a function of the transverse momentum p_T^W of the *W* boson from a next-to-leading order calculation (including resummation of large logarithms).

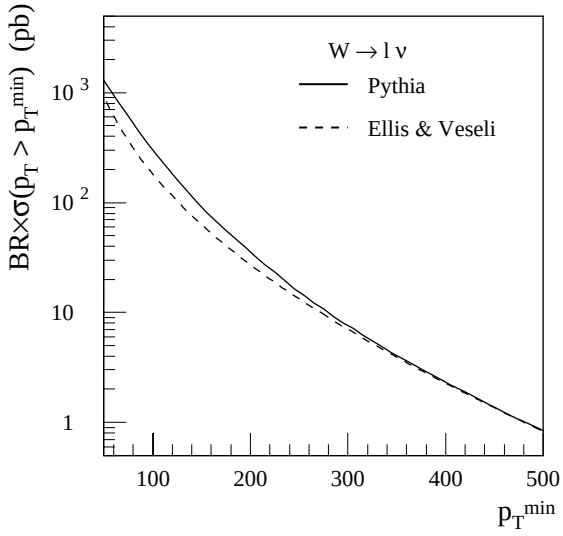

Figure 15-45 Cross-section for *W* production (with decay to either a muon or an electron) as a function of the minimum transverse momentum p_T^{min} of the *W* boson from a NLO calculation (Ellis and Veseli) and from a leading order calculation (PYTHIA).

cept and the first derivative of the differential cross-section for $p_T = 0$. The decay of the *W* boson, leading to a charged lepton (electron or muon) and a neutrino, is included using the following cuts: $p_T > 20$ GeV and $|\eta| < 2.5$ for the charged lepton and $p_T > 20$ GeV for the neutrino, approximating the experimental cut of missing transverse energy. Figure 15-45 shows the corresponding cross-section for *W* production up to transverse momenta of 500 GeV. Two calculations are shown: the resummed calculation from Ellis and Veseli and a leading order calculation from PYTHIA (including effects of parton showers and fragmentation). The cuts are identical to the ones used for Figure 15-44; in the case of PYTHIA a cut on the missing transverse energy (of at least 20 GeV) is performed, instead of the cut on the p_T of the neutrino in case of the Ellis-Veseli calculation. For large transverse momenta both calculations agree, as expected since in this region both are of $O(\alpha_s)$.

15.7.3.4 *W* + jet production

Measurements of the production of W bosons with associated jets were thought to have the potential to be used in a determination of the strong coupling constant. The cross-section for exclusive production of $W + n$ jets (n = 1,2,3,4) has been calculated at leading order [15-142]. A similar calculation [15-143] at leading order for LHC energies predicts for $p_T^W > 20$ GeV a cross-section of about 200 pb for W + 1 jet, about 50 pb for W + 2 jets and about 10 pb for W + 3 jets, where for the last two cross-sections a minimal jet transverse momentum of 19 GeV is required. The inclusive production of a *W* boson with at least one jet is calculated at next-to-leading order [15-84]. The study of the dependence of the associated jet rates in *W* production for different cone sizes defining the jet can give information on the ability of a next-to-leading order calculation to model the jet shape and to describe the overall production rate.The major source of background is the production of multi-jet final states, where one of the jets fakes an electron candidate and the event contains missing transverse energy.

A measurement of the ratio R_{10} of the inclusive cross-sections for W + 1 jet production to the one for W production [15-144] by the D0 collaboration using a cone size of 0.7 for the jet definition showed a NLO prediction being a factor of 2 smaller than the data in the range of 20 - 60 GeV for the minimal jet transverse energy. Furthermore the studies indicated no sensitivity of this ratio to the value of the strong coupling constant. The CDF collaboration measured the same ratio for two cone size: R = 0.4 [15-145] and R = 0.7 [15-146]. In the first case good agreement with the NLO calculation is found for minimal jet transverse energies between 15 and 95 GeV. For the case of R = 0.7, good agreement is observed for small transverse jet energies (< 35 GeV), at larger energies, the NLO prediction is smaller than the data by about 15%, being a 1σ difference. Comparing the results for the two cone sizes, an increase in R_{10} is found when going from 0.4 to 0.7 of about 30% for the data, whereas the NLO calculation only predicts about 10% increase. In both cases, CDF does not find a significant dependence of the ratio on the value of α_s.

Events with a W and associated jets can be used to study effects of colour coherence, which should lead to specific patterns in the parton flow from constructive or destructive interference between soft gluon emissions, as observed in e^+e^- annihilation ('string' effect). An important aspect is whether this pattern survives the hadronisation, as conjectured in the context of local parton hadron duality. The D0 collaboration has compared the distribution of soft particles in a disc of $0.7 < R < 1.5$ around the W and around the opposing jet [15-147], using the W as a template (since it is a colourless object). The data shows an enhancement of particle production around the tagged jet (with respect to the region around the W), as expected if colour coherence occurs. It has been suggested [15-148] to use these W + jet events to get information on properties of the soft gluon radiation. Using relevant event variables it is claimed that one could distinguish between the three partonic subprocesses contributing at lowest order: $qg \rightarrow Wq$, $gq \rightarrow Wq$ and $q\bar{q} \rightarrow Wg$. Possible applications are the derivation of constraints on the quark and gluon parton densities in the initial state and studies of the properties of quark and gluon jets.

The final state containing a W boson and four jets represents the dominant source of background for the top physics in the single lepton final state. The knowledge of the production of $Wb\bar{b}$ and $Wb\bar{b}$ + jet is important for the study of single top production and of the Wtb vertex. It has been calculated at leading order [15-149] (including, besides QCD processes, also the top signal, electroweak and Higgs contributions).

15.7.3.5 *W* + charm and *W* + bottom production

The production of W bosons with associated open charm production can be used to constrain the strange quark content of the proton [15-150]. The dominant production process is the QCD Compton graph with scattering on strange quarks: $gs \rightarrow Wc$. Background is expected from the production of $W + c\bar{c}$ $(b\bar{b})$, where the $c\bar{c}$ $(b\bar{b})$ pair is produced in the jet recoiling against the W and only one of the two heavy quarks is detected. The tagging of charm production could be done by searching for displaced vertices, by an exclusive reconstruction of non-leptonic decays of charmed baryons or mesons (*e.g.* the $D^* \rightarrow K\pi\pi$ decay) or by inclusive semi-leptonic decays.

The production of a W boson with an associated heavy quark pair can be used to deduce information on the gluon splitting to heavy quarks. The process proceeds via the annihilation of a quark-anti quark pair into a W and an off-shell gluon, where the latter splits into a heavy quark pair: $q\bar{q} \rightarrow Wg^* \rightarrow WQ\bar{Q}$. A selection would start from the decay lepton of the W. Next, requirements to identify two heavy quark decays would be added. This could be done by exclusive reconstruction of the decays or by demanding inclusive signatures like impact parameter significance.

For these channels additional studies are needed to assess the reach in kinematics, based on an inclusive trigger selection based on a lepton signature alone. In addition, the feasibility of reconstructing open charm has to be investigated and possibilities for an enrichment of such samples using the higher level triggers could be devised.

15.7.4 *Z* production

15.7.4.1 Cross-section

Besides the absence of final state interactions, the signature of a lepton pair from the production of a *Z* boson provides an unambiguous identification, in contrast to jet physics. Compared to the case of *W* boson production, for *Z* bosons the kinematics can be reconstructed accurately, since there is no neutrino carrying part of the boson momentum.

The cross-section for *Z* production at LHC energies is expected to have a contribution of more than 10% due to $s\bar{s}$ initial states. The product $x_1 \cdot x_2$ of the parton momenta is fixed to a value of about 4×10^{-5} at leading order. The major background sources are similar to the ones relevant for the inclusive *W* production (see Section 15.7.3.1). The experimental selection of *Z* production in ATLAS will be based on triggers requiring two leptons (electrons or muons), where a detailed description can be found in Section 11.7. This restriction to the clean leptonic decay mode of the Z is possible due to the large statistics expected for the LHC.

15.7.4.2 p_T distribution

Figure 15-46 shows the cross-section for production of *Z* bosons as a function of the transverse momentum $p_T{}^Z$, as obtained from a next-to-leading order calculation, including the resummation of large logarithms in the q_T space [15-140]. The various approaches to calculate the transverse momentum have been discussed for the case of *W* boson production in Section 15.7.3.3. The parton distribution MRS-R1 [15-141] has been used. For the decay leptons (electrons or muons) a minimal transverse momentum of 20 GeV was required and the leptons had to be produced within $|\eta| < 2.5$. The invariant mass of the lepton pair had to be within ±6 GeV of the nominal *Z* boson mass. The corresponding cross-section for larger transverse momentum of the *Z* boson is shown in Figure 15-47, both for the Ellis-Veseli calculation and the leading order calculation from PYTHIA (including parton showers and fragmentation effects). A cross-check with ISAJET gave cross-sections consistent with the ones obtained from PYTHIA.

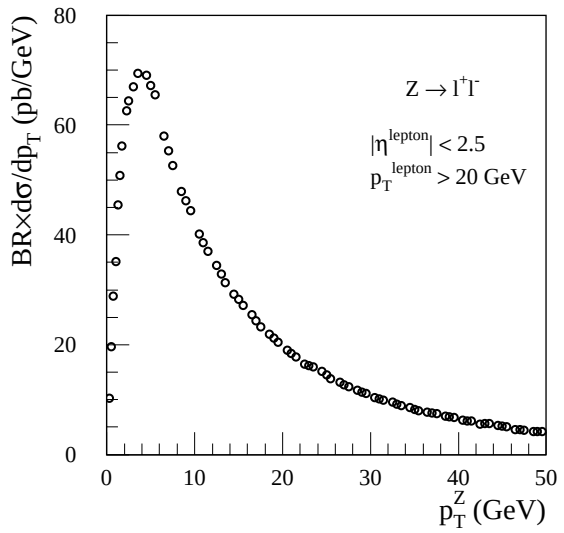

Figure 15-46 Differential cross-section for Z production (decay into either an electron or a muon pair) as a function of the transverse momentum p_T^Z of the Z boson from a next-to-leading order calculation including resummation of large logarithms.

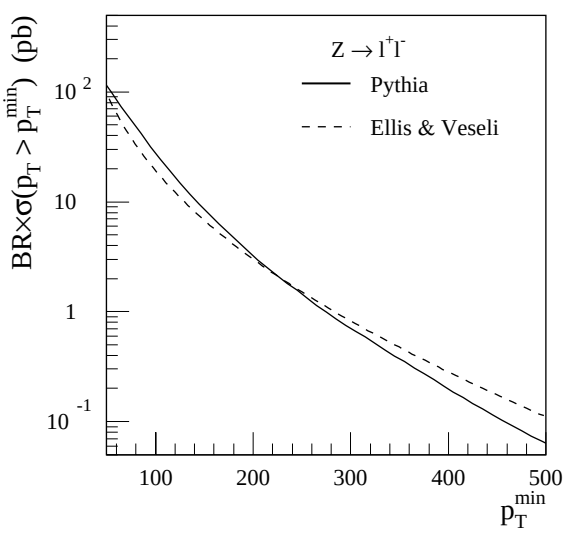

Figure 15-47 Cross-section for Z production (decay into either an electron or a muon pair) as a function of the minimum transverse momentum p_T^{min} of the Z boson from a NLO calculation (Ellis and Veseli) and from a leading order calculation (PYTHIA).

15.7.4.3 Forward-backward asymmetry

In Figure 15-48 the expected forward-backward asymmetry of Drell-Yan lepton pair production in the mass region of the Z resonance is shown as a function of the Z boson rapidity. The asymmetry A_{FB} is defined as the ratio of cross-sections $A_{FB} = (\sigma_F - \sigma_B)/(\sigma_F + \sigma_B)$, where $\sigma_{F/B} = \int_{0/-1}^{1/0} (d\sigma/d\cos\hat{\theta}) d\cos\hat{\theta}$ is the integrated cross-section for the angular distribution in the lepton pair centre-of-mass system. The prediction has been obtained using PYTHIA with the CTEQ2L parton distribution set and requiring the leptons to have $p_T > 20$ GeV and $|\eta| < 2.5$. The lepton pair mass had to be within ±6 GeV of the nominal Z boson mass. The errors shown correspond to the statistical uncertainty for an integrated luminosity of 30 fb^{-1}.

At the Tevatron, the measurement of the forward-backward asymmetry by CDF [15-151] has been used to determine the effective Weinberg angle $(\sin\theta_W)^2$. The determination of the effective Weinberg angle requires the subtraction of contributions to A_{FB} from background

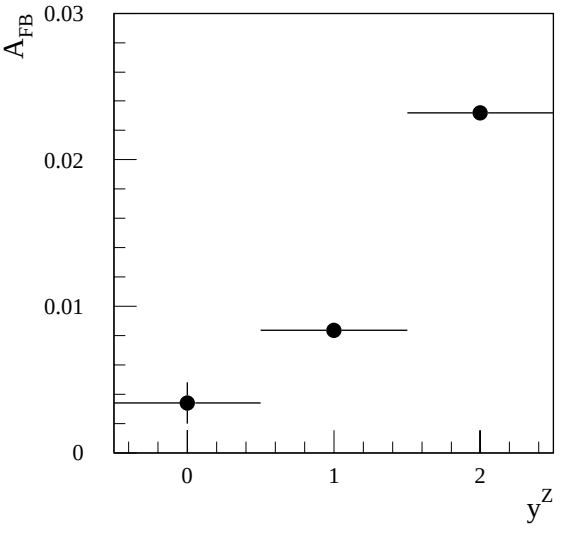

Figure 15-48 Expected forward-backward asymmetry of Z production as a function of the Z boson rapidity y^Z. For the PYTHIA (and ATLFAST calculation, the following cuts have been applied: $|\eta| < 2.5$, $p_T > 20$ GeV and $|M_{ll} - M_Z| < 6$ GeV.

processes as well as from higher QCD, QED and weak processes. The measurement performed by CDF reached a systematic uncertainty of about 1% on $(\sin\theta_W)^2$. This uncertainty is dominated by the uncertainty on the knowledge of the QCD background and on the QCD corrections.

15.7.4.4 *Z* + jet production

The exclusive production of a *Z* boson with *n* associated jets (*n* = 1,2,3,...) is known at leading order[15-142] while the inclusive production of a *Z* boson with at least one associated jet has been calculated at next-to-leading order[15-84]. An accurate measurement of *Z* + jet production can be used (in the case of four jets) to normalise the background from *W* + 4 jets to top quark production in the case of a single lepton and *b*-tag final state. In addition for gluino pair production leading to final states with four jets and missing E_T, the dominant background from the standard model is *Z* + 4 jet production, with an invisible decay of the *Z* to neutrinos. The calculation of the ratio of *W* + 4 jet to *Z* + 4 jet process [15-152] is insensitive, for Tevatron energies, to experimental cuts and theoretical ambiguities. Both processes are also calculated including heavy quark flavour identification.

15.7.5 Gauge boson pair production

15.7.5.1 *WW* and *ZZ* production

The production of gauge boson pairs [15-153] is used to study the triple gauge boson couplings (the result of the non-Abelian nature of the theory) and to derive limits on new interactions in Chapter 16. Boson pair production in hadronic collisions is dominated by the quark-antiquark annihilation process. In the case of *ZZ* and *WW* production the gluon-gluon fusion process also contributes (at $O(\alpha_s^2)$). However, even at LHC energies, it never dominates the $q\bar{q}$ annihilation. The experimental selection of gauge boson pair production will use criteria very similar to the inclusive *W* and *Z* production, based on leptonic decay modes. A detailed study of the *ZZ* production is important as the final state *ll*νν from *ZZ* represents a background to Higgs searches.

The production of *WW* boson pairs is in leading order due to the process $q\bar{q} \rightarrow WW$, either via *t*-channel quark exchange or via *s*-channel production of a γ^*/Z boson. The detection of the *WW* pair can proceed via a leptonic final state (*lνl'*ν') or semi-leptonic (*lνqq̄*).

The calculation of the cross-section for the pair production of the heavy gauge bosons has been performed in NLO. The results [15-154] are given for the following cuts: $p_T^l > 25$ GeV, missing transverse momentum > 50 GeV, $|\eta| < 3$ and an isolation cut for the leptons. At LO, the cross-section for *ZZ* production is found to be 36 fb, at NLO it increases to 43 fb. In the case of W^+W^-, the values are 470 fb at LO and 960 fb at NLO. The calculation has also includes results on kinematical distributions, like the transverse momentum spectrum for a pair of gauge bosons with (or without) an associated jet.

In Figure 15-49 the cross-section for *WW* production is shown as a function of the transverse momentum of the lepton from the *W* decay. The following cuts have been applied: the leptons (*l* = *e*, μ) are required to have a minimal transverse momentum of 20 GeV and have to be within $|\eta| < 2.5$. A missing transverse energy of at least 20 GeV is demanded in addition. The calculation is based on [15-155]; shown are the results at leading order and at next-to-leading order. Figure 15-50 shows the corresponding cross-section as a function of the missing transverse momentum. For a lepton transverse momentum of 100 GeV, the *K*-factor is about 1.5 and rises to

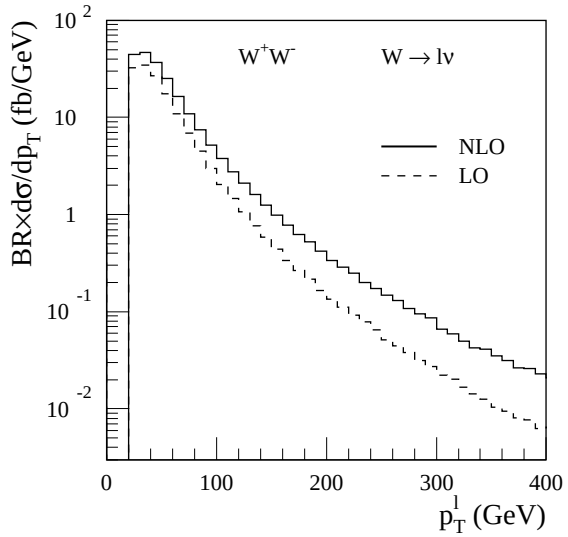

Figure 15-49 Differential cross-section for W^+W^- production and decay to leptons (where $l = e, \mu$) at leading and next-to-leading order as a function of the lepton transverse momentum p_T^l for the following cuts: $|\eta^l| < 2.5$, $p_T^l > 20$ GeV and $p_T^{miss} > 20$ GeV.

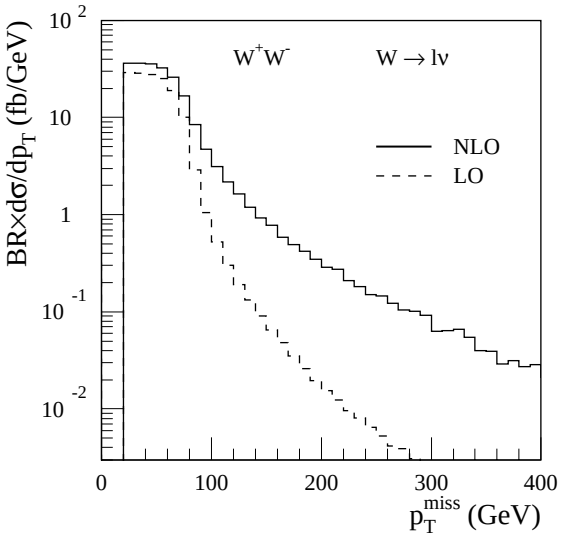

Figure 15-50 Differential cross-section for W^+W^- production and decay to leptons (where $l = e, \mu$) at leading and next-to-leading order as a function of the missing transverse momentum p_T^{miss} for the following cuts: $|\eta^l| < 2.5$, $p_T^l > 20$ GeV and $p_T^{miss} > 20$ GeV.

about three at $p_T = 400$ GeV. At a missing transverse momentum of 300 GeV, a huge *K*-factor of about 90 is obtained. These *K*-factors (which change also the shape of the distribution) are partially due to the appearance of real emission diagrams at next-to-leading order ($q\bar{q} \rightarrow WWg$ and $qg \rightarrow WWq$). In the latter diagram, one *W* boson is produced at large transverse momentum and recoils against the *q*, which radiates a soft *W* boson (almost collinear to the quark).

The selection criteria for the pure leptonic final state require two isolated leptons (*ee*, *e*μ, μμ) together with missing transverse energy to account for the neutrinos. The dominant background is due to top pair production (being larger than the *WW* signal), to a lesser extent also $Z \rightarrow \tau\tau$ and Drell-Yan production of *ee* and μμ contribute. Further sources of background include the production of multi-jets or *W* + jets, where jets are misidentified as electrons or heavy quark production whose decay leads to muons in the final state.

In case of the final state with two jets, the efficiency to resolve the two jets from the *W* decay drops significantly for values of $p_T^W > 200$ - 300 GeV (as discussed in Section 9.3.1). The production of a W boson with two or more associated jets dominates as background, multi-jet configurations with a jet being misidentified as an electron and with missing transverse energy can fake this signature too.

A next-to-leading order calculation of *ZZ* production [15-119] with subsequent decay to an electron pair and a muon pair has been performed restricting the leptons to $p_T^l > 25$ GeV, $|\eta^l| < 3$, requiring a separation of at least 0.4 in η–φ between the leptons and missing transverse energy of at least 50 GeV. The range in pseudo-rapidity for the leptons is slightly larger than the actual acceptance of $|\eta| < 2.5$. In Figure 15-51 the cross-section for the production of *ZZ* pairs is shown as a function of the invariant mass of the *ZZ* pair, in Figure 15-52 the cross-section for *ZZ* production is shown as a function of the transverse momentum of the *Z* boson. The calculation is based on the full NLO contributions, including a resummation of large logarithmic terms due to soft gluon radiation. For an integrated luminosity of 30 fb^{-1}, about 5×10^5 *ZZ* pairs are ex-

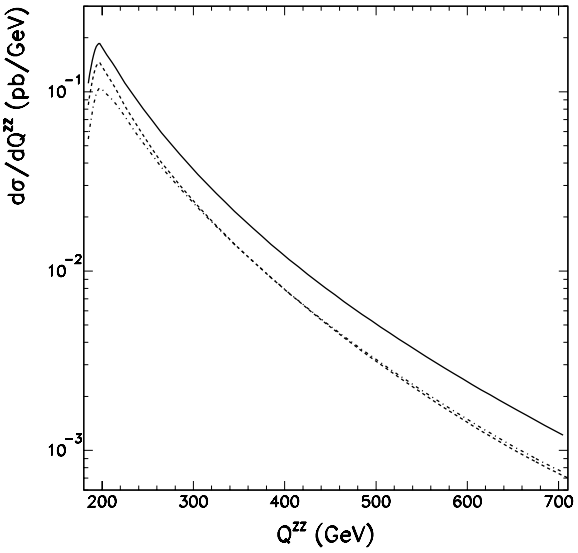

Figure 15-51 Cross-section for ZZ production as a function of the invariant mass Q^{ZZ} of the ZZ boson pair for a resummed calculation (from [15-119]). The cuts used in the calculation are: $p_T^l > 25$ GeV, $|y| < 3$ and $p_T^{miss} > 50$ GeV. The solid line shows the NLO results, the other curves are explained in the text.

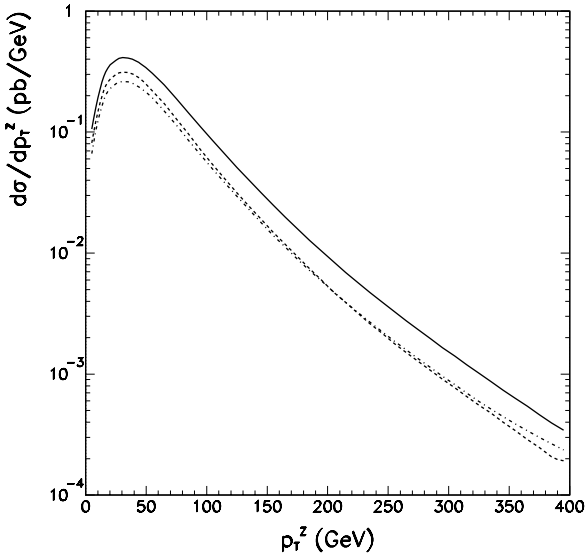

Figure 15-52 Cross-section for ZZ production as a function of the transverse momentum p_T^Z of one Z boson for a resummed calculation (from [15-119]). The cuts used in the calculation are: $p_T^l > 25$ GeV, $|y| < 3$ and $p_T^{miss} > 50$ GeV. The solid line shows the NLO results, the other curves are explained in the text.

pected to be produced at the LHC. For both figures, the rapidity of the Z boson produced has been restricted to $|y| < 3$, giving a total cross-section of 14.8 pb (with the CTEQ4M parton distributions), which is dominated by the $q\bar{q}$ initial state (10.9 pb) wrt the qg initial state (3.9 pb). The leading order contribution amounts to about 9 pb (for the CTEQ4L parton distributions). In both figures, the solid curve represents the full calculation, the dashed curve the contribution from the $q\bar{q}$ initial state and the dash-dotted curve the leading order part for the $q\bar{q}$ initial state.

15.7.5.2 $W\gamma$ and $Z\gamma$ production

The measurement of $W\gamma$ production can be used to probe to the $WW\gamma$ coupling. A typical selection will require a final state with a lepton, a photon and missing transverse energy. The dominant background source is due to W + jet production, where the jet fakes a photon. Smaller contributions are expected from $Z\gamma$ production and $W\gamma$, where the W decays via $\tau\nu$ to $l\nu\nu$. The calculation of $W\gamma$ production has been performed at NLO for several differential distributions [15-156]. An additional study at next-to-leading order has investigated the rapidity correlations between the lepton and the photon at LHC energies [15-157]. Using cuts on the photon ($p_T > 100$ GeV and $|\eta| < 2.5$), on the lepton ($p_T > 25$ GeV and $|\eta| < 3$), demanding a separation of at least 0.7 in η–ϕ between the lepton and the photon and requiring missing transverse energy of at least 50 GeV, it has been found that the QCD corrections lead to a K-factor of about 3. Although the actual acceptance in pseudo-rapidity is slightly smaller ($|\eta| < 2.5$), none of the conclusions will change. The differential distribution of the rapidity difference between photon and lepton shows that at the LHC the radiation zero amplitude is obscured by NLO corrections. The radiation zero amplitude (at parton level all helicity amplitudes vanish at lowest order for a certain value of the scattering angle between quark and photon) is one reason for the large K-

factor. A second reason is the collinear enhancement in $qg \rightarrow qW\gamma$, where a soft W is radiated off the quark (at the LHC the qg luminosity is large). As in the case of WW, this real emission diagram appears only at next-to-leading order.

The production of $Z\gamma$ can be used to study the triple boson couplings of $ZZ\gamma$ and $Z\gamma\gamma$, which at tree level in the Standard Model are zero. A similar selection as in the case of $W\gamma$ is required, except for the missing energy cut, which is replaced by demanding a second charged lepton. Background from Z + jet events, where the jet fakes a photon or an electron (in the latter case, this is being misidentified as a photon) dominates. Smaller contributions are due to multi-jet production and direct photon production. A calculation of the differential cross-section as a function of the transverse momentum of the photon at next-to-leading order, including the decay of the Z to leptons is available [15-158]. Applying the following cuts on the photon ($p_T^{\gamma} > 100$ GeV, $|\eta^{\gamma}| < 3$, isolation), on the leptons ($p_T^{l} > 20$ GeV, $|\eta^{l}| < 3$) and requiring a separation of at least 0.7 in η–ϕ between the photon and each lepton and an invariant mass of the photon-lepton pair of at least 100 GeV, a K-factor between 1.4 (for $p_T^{\gamma} = 100$ GeV) and 2 ($p_T^{\gamma} = 1$ TeV) is found. A previous calculation [15-159] gave a total cross-section of 230 fb at leading order and of 310 fb at next-to-leading order, using the following cuts: $p_T^{\gamma} > 50$ GeV, $|\eta^{\gamma}| < 2.5$, $p_T^{l} > 25$ GeV, $|\eta^{l}| < 3$, a separation of at least 0.7 between lepton and photon and a cut of 15% of the photon energy on the hadronic energy in a cone of 0.7 around the photon direction. As in the case of $W\gamma$ and WZ, the large NLO corrections at high transverse momentum of the photon are due to collinear enhancement in a real emission diagram ($qg \rightarrow Z\gamma q$) and the large qg luminosity at the LHC. The high p_T photon recoils against the quark, which radiates a soft Z boson. Due to the absence of a radiation zero amplitude at tree level, the K-factor for the $Z\gamma$ case is smaller than *e.g.* for $W\gamma$ or WZ.

15.7.5.3 *WZ* production

The measurement of WZ production probes the WWZ coupling. A calculation at next-to-leading order [15-160] is available, including the leptonic decays of the W and of the Z. A leading order cross-section of about 26 fb is obtained, using the following cuts: $p_T^{l} > 25$ GeV, $|\eta^{l}| < 3$, separation in η-ϕ of at least 0.4 between the leptons and missing transverse energy of at least 50 GeV. The total next-to-leading order cross-section (with the same cuts) amounts to about 52 fb. Lowering the cut on the missing transverse energy to 20 GeV increases the cross-section to about 81 fb at leading order. In Figure 15-53 the cross-section for WZ production as a function of the missing transverse momentum is shown, in Figure 15-54 the corresponding distribution as a function of transverse momentum of the lepton. The following cuts have been applied: the leptons ($l = e,\mu$) are required to have a minimal transverse momentum of 20 GeV and have to be within $|\eta| < 2.5$. A missing transverse energy of at least 20 GeV is demanded in addition. Both figures show large NLO corrections for large transverse momenta, *e.g.* for the lepton transverse momentum dependence the K-factor is about 2 at 100 GeV and rises to more than 5 at 400 GeV. In the case of the missing transverse momentum dependence, the K-factor amounts to about 4 at 400 GeV. The reason for these large K-factors is on one hand due to the radiation zero amplitude at tree level and on the other hand due to a collinear enhancement in the process $q_1 g \rightarrow WZq_2$, where at large p_T of the Z boson this is balanced by the quark, which then radiates a soft W boson. These real emission diagrams only appear at next-to-leading order and are further enhanced due to the large qg luminosity at the LHC.

For the final state of a lepton pair and an additional charged lepton at the Tevatron the CDF collaboration has one candidate event with three electrons and missing transverse energy [15-161]. The dominant background source for this channel is similar to the WW production for the semi-leptonic final state.

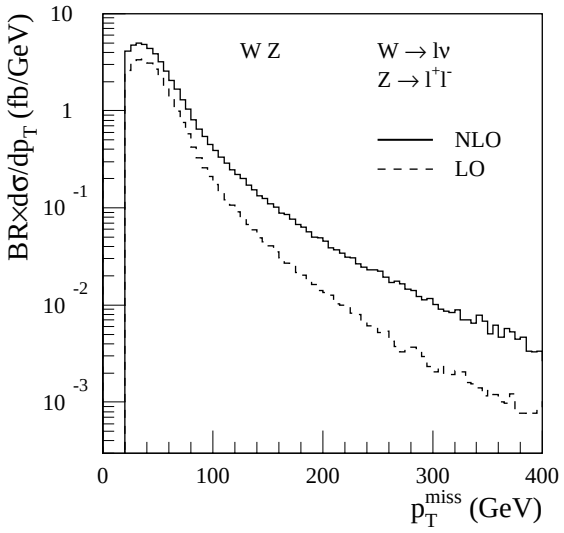

Figure 15-53 Differential cross-section for *WZ* production and decay to leptons (where $l = e, \mu$) at leading and next-to-leading order as a function of the missing transverse momentum p_T^{miss} for the following cuts: $|\eta^l| < 2.5$, $p_T^l > 20$ GeV and $p_T^{miss} > 20$ GeV.

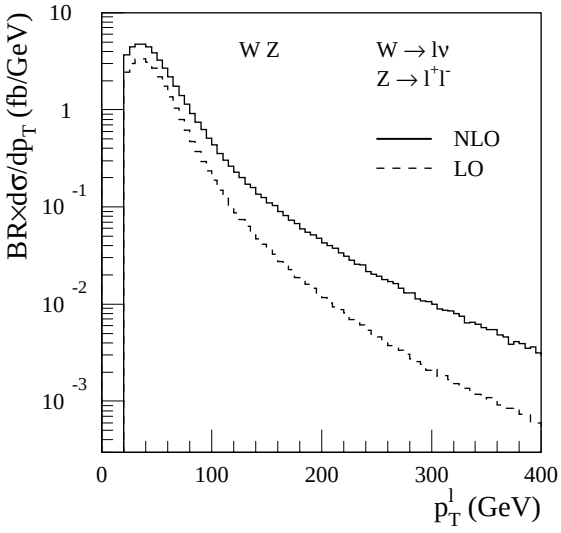

Figure 15-54 Differential cross-section for *WZ* production and decay to leptons (where $l = e, \mu$) at leading and next-to-leading order as a function of the lepton transverse momentum p_T^l for the following cuts: $|\eta^l| < 2.5$, $p_T^l > 20$ GeV and $p_T^{miss} > 20$ GeV.

15.8 Heavy flavour physics

15.8.1 Overview

Due to the quark mass involved, the production of heavy quarks (charm, bottom and top) provides an important process for the study of perturbative QCD and of the effects of non-perturbative aspects [15-162]. A perturbative approach is justified for large transverse momenta. In Figure 15-55 the differential cross-section for the production of a heavy quark pair is shown as a function of the transverse momentum of the heavy quark for *c*, *b* and *t* quarks (from [15-163], based on the calculations of [15-164] and [15-165]). Except for very small p_T ($p_T < 20$ GeV) the cross-sections for charm and bottom production are identical, showing that for transverse momenta much larger than the quark mass effects of the quark mass can be neglected. When higher-orders than NLO are included, the spectrum for *c* quarks is expected to become softer and differ-

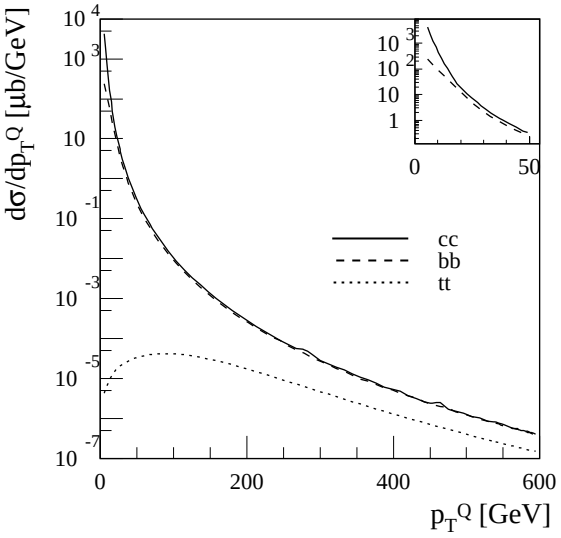

Figure 15-55 Differential cross-section for heavy quark pair production as a function of the transverse momentum p_T^Q of the heavy quark (for charm, bottom and top pair production, from [15-163]). The smaller figure shows for charm and bottom production the region of $p_T^Q < 50$ GeV.

ences might be visible even for larger p_T values. The total cross-sections for charm production is 7.8 mb, the one for bottom production 0.5 mb. The top-pair production cross-section is only 0.8 nb.

In this section, the production of charm quarks is discussed first (Section 15.8.2), concentrating mainly on the production of charmonium states (J/ψ and ψ'). Next, the production of b quarks is discussed (Section 15.8.3), where the emphasis lies on open bottom production, related to the studies of B physics as discussed in Chapter 17. Finally, the QCD related issues of top pair production will be presented (Section 15.8.4).

15.8.2 Charm production

15.8.2.1 Prompt J/ψ production

The direct production of J/ψ mesons can be studied due to the availability of vertexing detectors, which allow the separation of the contribution due to the production of B mesons with subsequent decay into final states containing a J/ψ. Further background is due to the production of χ_c mesons [15-166], which decay radiatively to a J/ψ meson. Measurements at the Tevatron [15-167],[15-168] have shown that the prediction of the colour-singlet model underestimates the data. This model uses perturbative QCD for the production of a colour-singlet state for the $c\bar{c}$ pair, which then can hadronise in a non-perturbative way to a charmonium state.

The discrepancy of the Tevatron data from this prediction led to a modified approach [15-55]; firstly all diagrams of perturbative QCD leading to a $c\bar{c}$ state are taken into account, whether or not the state forms a colour-singlet. Next the transformation of this state into a colour-singlet state is performed, assuming non-perturbative processes [15-169] (*e.g.* the colour-octet state is changed into a singlet state by emission of a very soft gluon). This leads to an expected similarity in the shape of the p_T distribution for different charmonium states, which is supported by the data. These models were then tuned to the data obtained at the Tevatron and subsequently used to extrapolate to LHC energies. This assumes that the non-perturbative contributions are universal.

Figure 15-56 shows the cross-section for direct J/ψ production (times the branching ratio for the decay to muons) [15-170] as a function of p_T. The calculation uses the CTEQ2L distribution and a cut on $|y| < 2.5$. The cross-section is decomposed into the contributions from the colour-singlet part and two colour-octet parts, which appear in the expansion as a function of the relative velocity of the two quarks: the ${}^1S_0^{(8)}$ '+' ${}^3P_J^{(8)}$ part and the ${}^3S_1^{(8)}$ part. These in total three parts can be determined from the Tevatron data and are then used to make the predictions shown above.

15.8.2.2 Prompt ψ(2S) production

In Figure 15-57 the cross-section for direct ψ' production [15-170] is shown, as a function of the p_T of the ψ' meson. The rapidity acceptance for the mesons is restricted to $|y| < 2.5$ and the CTEQ2L distribution has been used. For comparison, the cross-section for J/ψ production is also shown. Both give a similar shape and differ by about a factor of ten in absolute value.

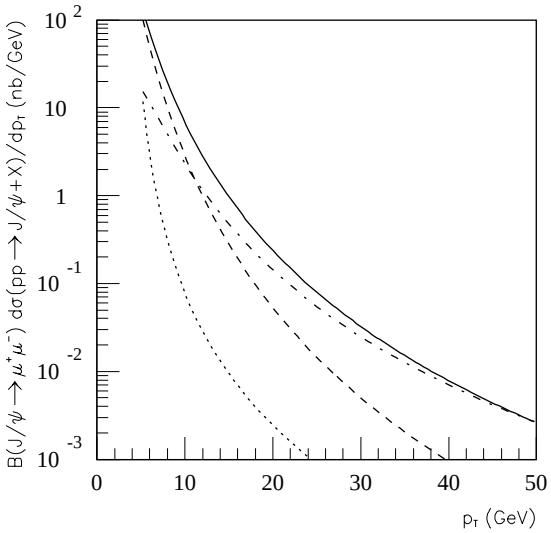

Figure 15-56 The cross-section for direct *J/ψ* production (with the decay to two muons) at the LHC a function of the *J/ψ* transverse momentum (from [15-170]). Shown are the total cross-section (solid), the colour-singlet contribution (dotted) and two colour-octet contributions (dashed for the ${}^1S_0^{(8)}$ '+' ${}^3P_J^{(8)}$ contribution and dot-dashed for the one of ${}^3S_1^{(8)}$).

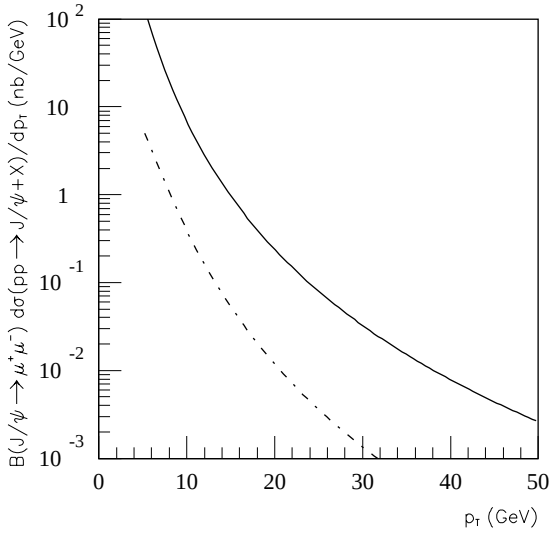

Figure 15-57 The cross-section for direct ψ' production (with the decay to two muons, the dash-dotted line) at the LHC as a function of the ψ' transverse momentum (from [15-170]). Also shown is the corresponding cross-section for *J/ψ* production (the solid line) as a function of the *J/ψ* transverse momentum.

15.8.2.3 Production of J/ψ with a photon or a massive vector boson

The associated production of a *J/ψ* meson at the LHC, together with a photon, should not be dominated by fragmentation contributions up to p_T values of 50 GeV [15-171]. This should be due to the fact that $q\bar{q}$ initial states are suppressed at the LHC. The more abundant *gg* initial states do not contribute to this process at leading order, higher order corrections are expected to be negligible. The expected differential cross-section (with the restriction $|y| < 2.5$) ranges from about 0.1 pb / GeV for p_T = 20 GeV to 0.5 nb / GeV at 100 GeV transverse momentum. A further possibility is the associated study of the production of *J/ψ* mesons with a *W* or *Z* boson, as discussed in [15-172], which can be used to cross-check the predictions of the colour octet model.

15.8.2.4 Open $c\bar{c}$ production

As discussed in [15-55], the production of open charm (*i.e.* the production of $D\overline{D}$ pairs) is expected to show a similar kinematical dependence on x_F as the production of *J/ψ* mesons. This can be used as a further constraint to verify predictions of different models. The experimental challenge is the selection of a sample of open charm production. When the *D* meson decays are reconstructed via π and *K* final states, there is no trigger available to select these. One possibility would be to use a sample of minimum-bias events (selected either by a trigger on random bunch crossings or by a trigger using information from dedicated detectors in the forward region, as mentioned in Section 15.3.2) where $c\bar{c}$ should contribute to a sizeable fraction of the total cross-section. To enrich this sample of events, it could be helpful to do a reconstruction of

charged tracks in the Inner Detector at the higher trigger levels and to pre-select *D* meson decay candidates. Further studies have to be performed in order to quantify the possible reach of such a selection.

15.8.3 Bottom production

15.8.3.1 Prompt Υ production

The production of bottomonium states should proceed either directly or via the decay of higher mass $b\bar{b}$ states. It exhibits similar discrepancies with respect to the predictions of the colour-singlet model. The cross-sections measured at the Tevatron for the production of the Υ(1S), Υ(2S) and Υ(3S) states [15-173] are larger then the predicted ones, with the discrepancy factor depending on the transverse momentum of the Υ resonance and increasing with increasing p_T (exceeding a factor of ten in the case of the Υ(1S)). An advantage of using Υ production, with respect to the production of charmonium states, is the possibility to reach smaller transverse momenta in case of the Υ, due to experimental selection requirements.

The associated production of an Υ meson together with a *W* or *Z* boson has been proposed [15-174] as a possible check for different model predictions. The dominant contribution to this process is expected from the production of a $b\bar{b}$ colour-octet state, which then binds to a *P*-wave state, that subsequently decays to an Υ. The expected cross-section amounts to 44 fb for Υ + *W* and 7 fb for Υ + *Z* production. This channel could also be used to search for heavy particles, decaying into a *W* or *Z* boson together with a $b\bar{b}$ pair.

15.8.3.2 Beauty production features

ATLAS will observe *B*-hadrons produced in proton-proton collisions at $\sqrt{s}$ = 14 TeV in the central rapidity region, $|\eta| < 2.5$. The lower limit for the *B*-hadron transverse momentum $p_T(B)$ is set by the trigger requiring a muon with $p_T(\mu) > 6$ GeV. This corresponds to approximately $p_T(B) > 10$ GeV. The specific property of this kinematical region is that beauty production should be governed mostly by perturbative QCD. Contributions from non-perturbative diffractive processes are expected to be small, and the interaction between the reaction products and the beam remnants is negligible.

The observed particle spectra represent a composite effect of three factors: the parton densities, the hard partonic subprocess and the hadronisation or fragmentation. The quark distribution functions are measured precisely in deep-inelastic scattering (see Section 15.2) over a range in x from 10^{-1} to 10^{-5}, which fully includes the range $10^{-4} < x < 10^{-1}$ accessible in *B* production at ATLAS. The fragmentation functions are clearly determined at LEP in e^+e^- annihilation. In the cases when the hard QCD dynamics is well understood, LHC gives access to direct measurements of gluon densities by means of the dominant gluon-gluon fusion process.

The present experimental results at Fermilab [15-175][15-176] indicate that the theory of beauty production is still not complete, suggesting important contributions from higher-order corrections beyond the LO and NLO calculations [15-164][15-177]. At the phenomenological level, the higher-order QCD contributions are interpreted in terms of additional production mechanisms, such as the Flavour Excitation and Parton Showering [15-14]. Methods of experimental separation of different production mechanisms based on the observation of specific phase space regions are discussed in the next sections.

15.8.3.3 Single *b* differential cross-section

The inclusive single *b* quark (or *B*-hadron) distributions together with the total visible production cross-section provide the simplest test of theoretical consistency. Typically the shape of the differential cross-section $d^2\sigma / dp_T d\eta$ shows only little sensitivity to the details of the production mechanism. The difference between models is mainly in the overall cross-section normalisation and usually does not exceed the inherent theoretical uncertainties. In this sense, the single *b* distributions can not be easily used to discriminate between different theories, unless a significant discrepancy is observed.

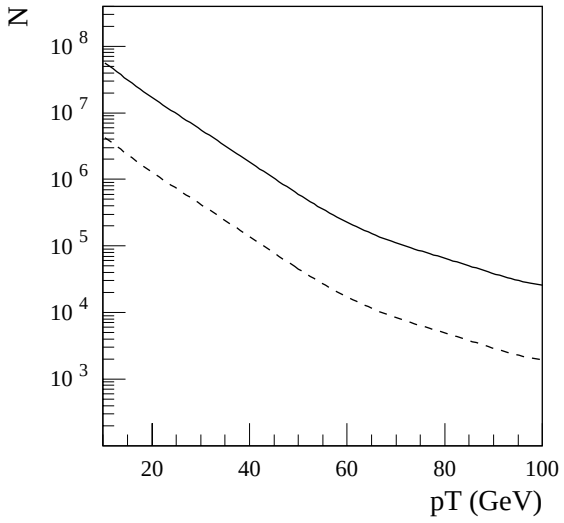

Figure 15-58 Number of reconstructed inclusive and exclusive *B*-hadron decays to $J/\psi(\mu\mu)$ for 30 fb^{-1}, as a function of the minimum transverse momentum of the *B*-hadron. The solid line corresponds to inclusive events ($b\bar{b} \rightarrow J/\psi\, X$ with $J/\psi \rightarrow \mu\mu$). The sum of the following exclusive channels is shown as the dashed line: $B_d \rightarrow J/\psi\, K^0(\pi\pi)$, $B_d \rightarrow J/\psi\, K^{0*}(K^+\pi^-)$, $B^+ \rightarrow J/\psi\, K^+$, $B_s \rightarrow J/\psi\, \phi(KK)$ and $\Lambda_b \rightarrow J/\psi\, \Lambda^0(p\pi^-)$, always with $J/\psi \rightarrow \mu\mu$.

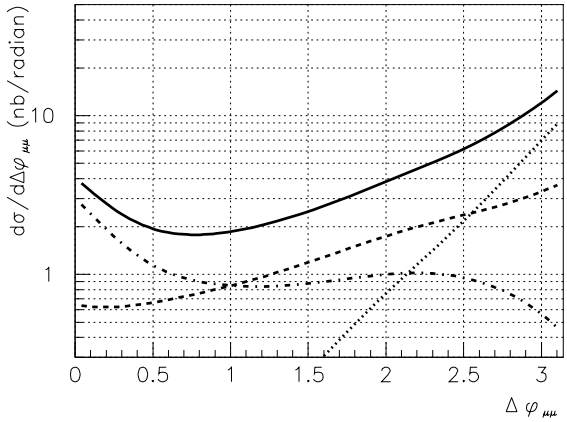

Figure 15-59 Azimuthal μμ correlations at the LHC (from [15-179]). Shown are the different mechanisms contributing in PYTHIA to the $\Delta\phi_{\mu\mu}$ spectrum: flavour excitation $gb \rightarrow gb$ (dash-dotted curve), gluon–gluon fusion $gg \rightarrow b\bar{b}$ (dotted curve), gluon–gluon scattering followed by gluon splitting $gg \rightarrow gg$ with $g \rightarrow b\bar{b}$ (dashed curve) and the sum of all contributions (solid curve).

Due to a large beauty production cross-section and a selective trigger, ATLAS can reconstruct large samples of exclusive *B*-hadron decays. Statistically dominant, with the trigger criteria that have been considered so far, are the exclusive channels with $J/\psi \rightarrow \mu\mu$ (Figure 15-58), which will allow measurements up to $p_T \sim 100$ GeV with negligible statistical errors (about 2000 events with $p_T > 100$ GeV). The region of higher p_T can be covered by inclusive $J/\psi \rightarrow \mu\mu$ measurements. It has been shown that a J/ψ vertex cut will remove the direct J/ψ contribution. A comparison with exclusive decays can be used for calibration.

Using $b\bar{b} \rightarrow J/\psi(\mu\mu)\, X$ events (where the *b* quark was required to have a transverse momentum larger than 40 GeV), which were passed to a full detector simulation, the efficiency for the reconstruction of muons using the combined information from the muon chambers, the Inner Detector and the calorimeters was studied (for more details on the combined reconstruction procedure see Section 8.1). As seen in Figure 15-60, the muons from the J/ψ decay can be identified with high efficiency, despite the large transverse momentum of the *b* jet. For a transverse momentum of the muon larger than 10 GeV the efficiency reaches a value of about 85%. In

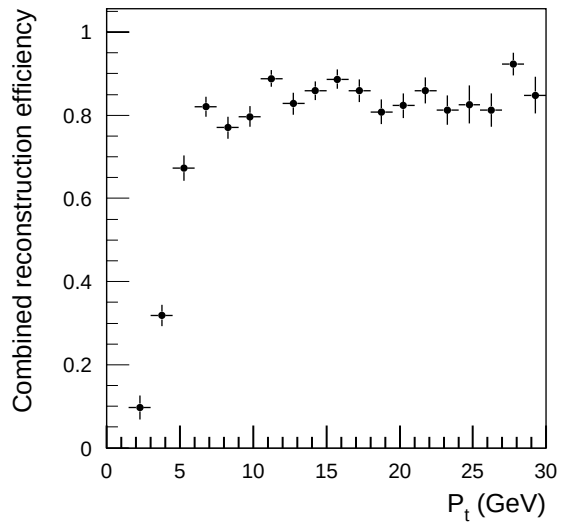

Figure 15-60 Reconstruction efficiency for muons from $b\bar{b} \rightarrow J/\psi(\mu\mu)\,X$ events (with a minimal transverse momentum of the b quark of 40 GeV) as a function of the minimum muon transverse momentum p_T.

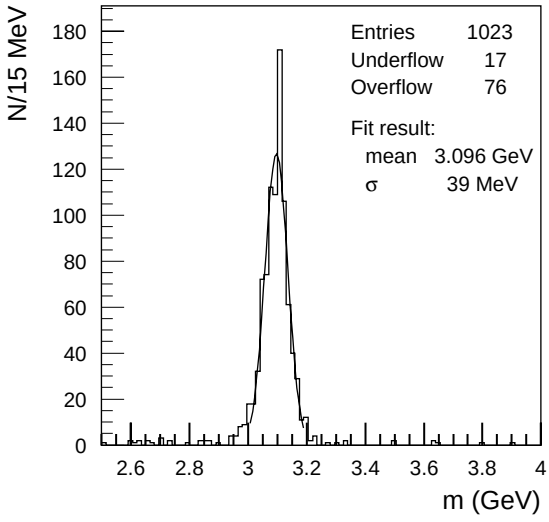

Figure 15-61 Mass resolution for muon pairs from $b\bar{b} \rightarrow J/\psi(\mu\mu)\,X$ events (with a minimum transverse momentum of the b quark of 40 GeV). Shown is the distribution of the invariant mass m of the muon pair.

Figure 15-61 the resolution in the invariant mass of the muon pair is shown, from a fit of a Gaussian a resolution of 39 MeV is obtained. The resolution does not degrade in comparison with the case when the J/ψ is reconstructed from the tracks of the Inner Detector (using information from the event simulation for the identification of the muons, as discussed in Section 6.6.1 of [15-178]). The probability to lose an event due to the matching of a muon (from the muon system) to a wrong track in the Inner Detector is only about 10%, leading to events where the invariant mass of the muon pair is outside a 3σ window around the nominal J/ψ mass. This is the result of a first study, where further improvements, especially on the loss of events, are expected.

The lower p_T limit on channels with $J/\psi \rightarrow \mu\mu$ comes from the muon trigger and muon identification performance. There are exclusive channels with electrons and hadrons reconstructed with $p_T < 10$ GeV, but they are biased by a LVL1 p_T cut on the muon coming from the associated B hadron. These events can be used for b-$\bar{b}$ correlation measurements, as discussed below.

15.8.3.4 $b - \bar{b}$ correlations

The correlations between the b and $\bar{b}$ quarks are usually presented in terms of the azimuthal angular difference $\Delta\phi$. In Figure 15-59 the expected azimuthal correlation $\Delta\phi_{\mu\mu}$ between the muons from the b and $\bar{b}$ decay is shown, which can be used to get information about the correlation between the b and $\bar{b}$. The domain of back-to-back kinematics, $\Delta\phi_{\mu\mu} \sim \pi$, is mostly populated by the LO QCD contribution. On the contrary, the effects of higher orders are most pronounced in the deviations from this back-to-back configuration. The region of $\Delta\varphi_{\mu\mu} \sim 0$ is free of the LO contribution, and so is only sensitive to the NLO contributions.

b-$\bar{b}$ correlations can be measured by full reconstruction of one of the associated B hadrons and by the inclusive reconstruction (lepton) of the other B hadron (see Section 17.1.1). After the exclusive reconstruction of a B hadron, no isolation cuts are needed to separate an accompanying lepton. This type of event gives a possibility to detect b and $\bar{b}$ quarks produced close to each other. There will be approximately 5×10^5 events of this type after three years, however, they are

mostly concentrated at $\Delta\varphi \sim \pi$, with only a minor part contributing to the region of interest $\Delta\varphi \sim 0$. Besides that, the angular correlations should be studied for different transverse momenta of b and $\bar{b}$ quarks. All this requires high statistics, which can be obtained by an inclusive reconstruction of J/ψ from B hadrons and a lepton from the semileptonic decays of the associated anti-B hadrons. The argument for not requiring the lepton to be isolated from J/ψ is still valid. The expected number of events as listed in Table 15-1 is of the order of 6×10^6. The exclusive decays can be used for calibration. For large transverse momenta the statistics can be extended by using inclusive events with two muons of opposite charge coming from semileptonic decays of two B hadrons. The selection of these events at the trigger is under study; as discussed in Section 11.6 the second level trigger is capable to accept the expected rate of two muon events. Requiring for the second muon a threshold of $p_T(\mu) > 5$ GeV will give in 3 years of the order of 10^9 events (after the second level trigger) with two muons from $b\bar{b}$ events (including the contribution from minimum bias events). More studies are needed to assess the final contribution from $c\bar{c}$ production and from π/K decays.

Table 15-1 Expected number of inclusive $b\bar{b} \rightarrow J/\psi X$ events (where the J/ψ decays to leptons) reconstructed after 3 years. These events will be used for $b - \bar{b}$ correlations studies. For each inclusive channel the number of exclusive events with the same lepton content is given. Here '*had*' denotes any of K^0, K^{0*}, K^+, Λ^0 or ϕ, and '*B*' stands for either B^0, B^+, B_s or Λ_b.

Inclusive decay channel	Number of events for inclusive reconstruction	Exclusive channels with the same lepton content	Number of events in reconstructed exclusive channels
$b\bar{b} \rightarrow \mu\ \ J/\psi(\mu\mu)\ X$	2.8×10^6	$bB \rightarrow \mu\ \ J/\psi(\mu\mu)\ had$	2.1×10^5
$b\bar{b} \rightarrow e\ \ J/\psi(\mu\mu)\ X$	3.6×10^6	$bB \rightarrow e\ \ J/\psi(\mu\mu)\ had$	2.1×10^5
$b\bar{b} \rightarrow \mu\ \ J/\psi(ee)\ X$	0.6×10^6	$bB \rightarrow \mu\ \ J/\psi(ee)\ had$	0.9×10^5

15.8.3.5 Production asymmetry

The B-hadron production asymmetry is defined as the difference of the probabilities of B and $\overline{B}$ hadron production in pp collisions. From the theoretical point of view, the asymmetry can provide information on the effects of soft dynamics during the fragmentation (*i.e.* the soft interactions between the produced b quark and the remnants of the disrupted proton). However, the relevant physical effects are expected [15-14],[15-180],[15-181] to be unimportant [15-182],[15-183] in the central rapidity region covered by ATLAS.

A production asymmetry always occurs at the presence of a *CP*-violation asymmetry originating from the B-hadron decays (see Section 17). In some cases these two effects are expected to be of the same order, for instance in the channels $B^0 \rightarrow J/\psi(\mu\mu)\, K^{0*}$, $B^+ \rightarrow J/\psi(\mu\mu)\, K^+$ and $\Lambda_b \rightarrow J/\psi(\mu\mu)\, \Lambda^0$. These channels are expected to have small CP violation (< 1%) due to interference between the lowest and higher-order decay amplitudes. A method of separation of these two effects is considered, which is based on the fact that the production asymmetry varies with transverse momentum and the rapidity of produced b quark, while the decay process should remain the same.

However, measurements of such small effects will require very good understanding of the possible detection asymmetries. For the selected channels the LVL1 trigger asymmetries due to muon charge are not relevant, as a muon comes from the decay of the J/ψ. In the Inner Detector

the asymmetry may come from differences in hadron reconstruction with opposite charges, *e.g.* due to strong interaction cross-sections. More details on systematic uncertainties can be found in Chapter 17.

15.8.3.6 Production polarisation

The polarisation phenomenon is closely related to the production mechanism and, probably, includes an interplay between 'hard' and 'soft' interactions. This topic is addressed in Section 17.5.

15.8.3.7 Double beauty production

The production of two heavy-quark pairs is a fourth-order QCD process, and so provides a sensitive test of perturbative QCD. The full fixed-order $O(\alpha_s^4)$ calculation [15-184] for $p\,p$ collisions at the LHC gives a cross-section of about 440 nb which contrasts with a value of 3800 nb predicted by PYTHIA. This difference maybe due to an underestimation of higher order effects in the fixed order QCD calculation, together with an overestimation of these by PYTHIA.

Even the larger (PYTHIA) cross-section prediction is, however, too small to allow the double beauty production detection and its separation from the background processes. For the *B* physics studies requiring tagging of *B* flavour it was shown [15-184] that the probability of a wrong tag due to double *b* production will be negligible: 10^{-4} - 10^{-3}, as also discussed in more detail in Section 17.2.2.4.

15.8.4 Top production

15.8.4.1 Total cross-section

Within perturbative QCD, higher order corrections to the total cross-section for top pair production are under control and the scale uncertainty for a NLO calculation is of the order of 10% at Tevatron energies and similar for the LHC. When taking into account a resummation of soft gluon effects [15-185], the uncertainty is decreased to about 5% for LHC energies. The inclusion of the soft gluon resummation leads to an increase of the cross-section for a large scale and even to a decrease at a small scale, thus reducing the scale dependence. The total cross-section for $t\bar{t}$ production (assuming a top quark mass of 175 GeV and using the MRSR2 parton distribution set [15-141]) is 803 pb at NLO and 833 pb for NLO including the NLL resummation [15-185]. In Figure 15-62 the dependence of the total $t\bar{t}$ cross-section on the top mass, m_{top}, is shown for the NLO calculation including the NLL resummation. In addition, the predictions of the NLO+NLL as well as the one of the NLO calculation alone are shown, for setting the scale μ to the values $\mu = 2\mu_0$ and $\mu = \mu_0/2$ (where $\mu_0 = m_{top}$). As mentioned above, the sizeable scale dependence at NLO is reduced when the NLL resummation is included.

An uncertainty of similar size (to the one of the scale uncertainty) arises due to the choice of the parton distribution function. The precision on the measurement of the total cross-section is expected to be dominated by the knowledge of the absolute scale of the luminosity. More details on the experimental selection and the study of systematic uncertainties can be found in Section 18.1.4.1. An error of 5% on the total $t\bar{t}$ cross-section corresponds (when the validity of the NLO+NLL calculation is assumed) to an error of 1% on the top mass.

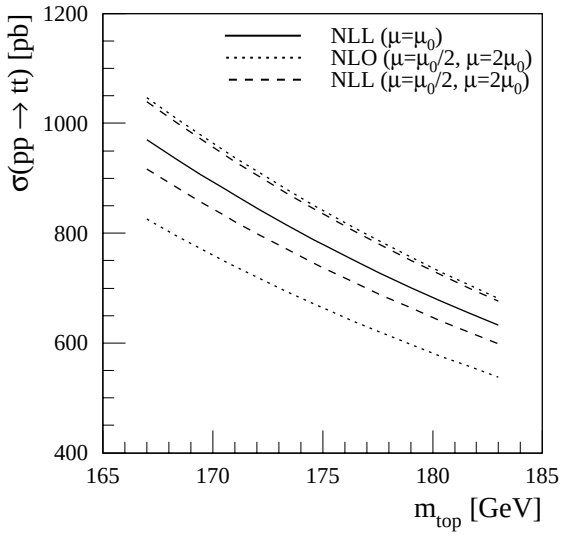

Figure 15-62 Total cross-section for top pair production as a function of the top mass, m_{top}. The solid line shows the cross-section at NLO, including the resummation of soft gluon contributions (NLL), based on [15-185]. The dashed (dotted) line indicates the scale uncertainty for the NLO+NLL (NLO only) calculation.

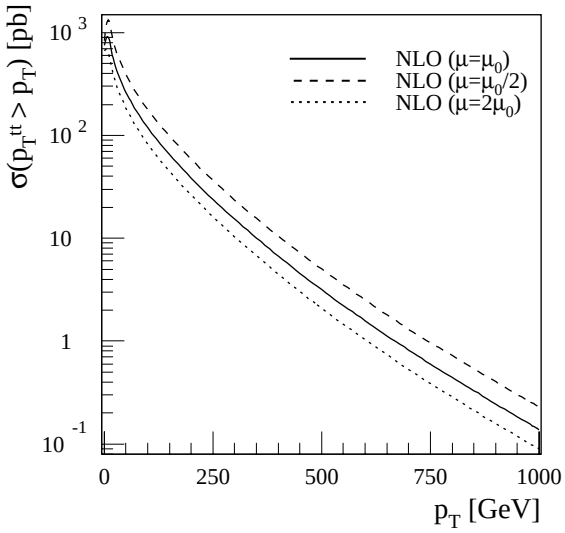

Figure 15-63 Cross-section for top pair production as a function of the minimum transverse momentum of the top pair from a NLO calculation (solid line). The dashed and the dotted lines indicate the scale uncertainty of the NLO calculation [15-177], using the MRST pdf.

15.8.4.2 Inclusive p_T distribution of the $t\bar{t}$ pair

The measurement of the p_T of the top quark for the top pair production is important for the understanding of the top production efficiencies needed for a precise cross-section measurement. In contrast to the measurement of the inclusive p_T distribution for b quark production (which can be done using the inclusive measurement of the transverse momentum of muons), this measurement will start from a reconstructed top quark decay, where details on the cuts for the selection of top quarks are given in Section 18.1.2.

In Figure 15-63 the integrated cross-section for $t\bar{t}$ production is shown as a function of the minimal transverse momentum of the $t\bar{t}$ pair. The NLO calculation [15-177] (using the MRST parton distribution set) is shown for a value of the scale μ being equal to μ_0, where μ_0 is given by $\mu_0^2 = m_{top}^2 + p_{T,\,top}^2$. The scale uncertainty is obtained by choosing the settings $\mu = 2\mu_0$ and $\mu = \mu_0 / 2$ for the scale μ.

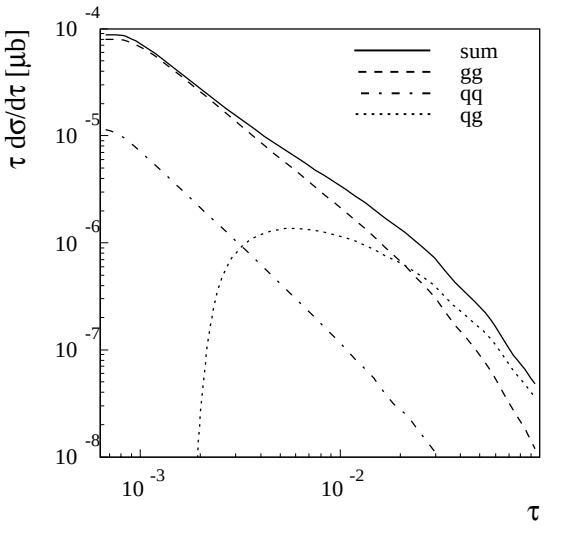

Figure 15-64 Differential cross-section for $t\bar{t}$ production as a function of the normalised centre-of-mass energy $\sqrt{\tau}$ (where $\tau = \hat{s}/s$) of the partonic initial state for the three different parton-parton initial states (from [15-163], using the MRST pdf).

15.8.4.3 $t\bar{t}$ mass distribution

A clarification of possible deviations in the production cross-section regarding new physics needs to study kinematical distributions, like the invariant mass of the $t\bar{t}$ pair. Deviations from the QCD expectation (like new *s*-channel resonances) should give characteristic signatures in the invariant mass distribution. Furthermore the extraction of Higgs decay into $t\bar{t}$ (at low tanβ) requires a precise knowledge of the invariant mass distribution. More details can be found in Section 18.1.4.

The precise measurement of the production of top quark pairs can be used to put constraints on the gluon density. Figure 15-64 shows the differential cross-section for top pair production at the LHC as a function of the normalised hard process centre-of-mass energy $\sqrt{\tau} = \sqrt{x_1 \cdot x_2}$. For value of $\sqrt{\tau} < 0.1$ the cross-section is dominated by the gluon-gluon initial state, for larger values of $\sqrt{\tau}$ the quark-gluon initial state starts to dominate.

15.9 Conclusion

The overview presented in this section illustrates the variety of QCD related processes that can be studied using the ATLAS detector. These measurements are of importance as a study of QCD at the LHC, accessing a new kinematic regime at the highest energy accessible in the laboratory. On the other hand, a precise knowledge and understanding of QCD processes is important for the studies of the Higgs boson(s) and searches for new physics beyond the Standard Model, where QCD represents a large part of the background.

The study of diffractive processes, which allows to access the hard and soft regime of QCD at the same time, presents a significant experimental challenge in the LHC environment and given the limited angular acceptance of the ATLAS detector. More detailed studies are needed to quantify and prove the ideas sketched in this section and to validate the design of the additional detectors envisaged.

At the present stage of these studies of QCD related processes, the possible constraints on parton density functions are difficult to quantify. Given more precise information about the actual measurement range possible and the achievable accuracy (obtained from detailed simulation of the detector response), it will be necessary to perform ‘global fits’ to determine the impact of the LHC measurements. As a further study one should investigate the amount of information on the parton distributions, that can be deduced from the LHC data alone.

Candidate signatures to provide constraints on the quark and anti-quark distributions are the production of *W* and *Z* bosons via the Drell-Yan process as well as lepton pair production in general. On the other hand, the production of direct photons, of jets and of top quarks can be used to get information on the gluon distribution.

The LHC will extend the kinematic range to larger values of Q^2, the hard scale of the partonic process, reaching scales of the order of TeV^2. The fraction of the proton momentum attributed to a parton will allow access to values below 10^{-5}, while keeping the scale above 100 GeV^2, in contrast to HERA measurements, where these small momentum fractions are only reached for hard scales close to or even below 1 GeV^2.

15.10 References

15-1 J.E. Huth and M.L. Mangano, Ann. Rev. Nucl. Part. Sci. **43** (1993) 585.

15-2 R.K. Ellis, W.J. Stirling, B.R. Webber, 'QCD and Collider physics', Cambridge, UK, Univ. Pr. (1996).

15-3 J. Huston, 'QCD at High Energies', plenary talk at the XXIX International Conference on High Energy Physics (ICHEP 98), Vancouver, Canada, 23-29 Jul 1998, preprint hep-ph/9901352 (1999).

15-4 ATLAS Collaboration, Trigger Performance Status Report, CERN/LHCC/98-15 (1998).

15-5 J. Huston, 'LHC Guide to Parton Distribution Functions and Cross Sections', ATLAS Internal Note ATL-PHYS-99-008 (1999).

15-6 H.L. Lai *et al.*, preprint hep-ph/9903282 (1999).

15-7 A.D. Martin *et al.*, Eur. Phys. J. **C4** (1998) 463.

15-8 H.L. Lai *et al.*, Phys. Rev. **D55** (1997) 1280.

15-9 Yu. L. Dokshitzer, preprint hep-ph/9812252, (1998).

15-10 Yu.L. Dokshitzer, Sov. Phys. JETP **46** (1971) 641;
V.N. Gribov and L.N. Lipatov, Sov. J. Nucl. Phys. **15** (1972) 438 und 675;
G. Altarelli and G. Parisi, Nucl. Phys. **B126** (1977) 298.

15-11 E.A. Kuraev, L.N. Lipatov and V.S. Fadin, Zh. Eksp. Teor. Fiz. **71** (1976) 840;
E.A. Kuraev, L.N. Lipatov and V.S. Fadin, Zh. Eksp. Teor. Fiz. **72** (1977) 377;
Ya.Ya. Balitsky and L.N. Lipatov, Yad. Fiz. **28** (1978) 1597.

15-12 W.J. Stirling, 'Structure Functions', Talk given at the LHCC workshop 'Theory of LHC processes', Feb. 1998, CERN.

15-13 G. Marchesini *et al.*, Comp. Phys. Comm. **67** (1992) 465.

15-14 T. Sjostrand, Comp. Phys. Comm. **82** (1994) 74.

15-15 Wu-Ki Tung, 'Perspectives on Global QCD Analyses', in Proceedings of the International Workshop on Deep Inelastic Scattering and Related Subjects, Eilat, Israel (1994), ed. A. Levy, World Scientific Publishing Co., Singapore.

15-16 W.T. Giele and S. Keller, Phys. Rev. **D58** (1998) 94023.

15-17 J. Huston *et al.*, Phys.Rev. **D58** (1998) 1140.

15-18 A.M. Cooper-Sarkar, R.C.E. Devenish and A. De Roeck, Int. J. Mod. Phys. **A13** (1998) 3385.

15-19 L. Apanasevich *et al.*, Phys. Rev. **D59** (1999) 074007.

15-20 G. Ingelman, (ed.), A. De Roeck, (ed.) and R. Klanner, (ed.), 'FUTURE PHYSICS AT HERA', preprint DESY 96-235 (1996), Hamburg, Germany.

15-21 M. Dittmar, F. Pauss, D. Zuercher, Phys. Rev. **D56** (1997) 7284.

15-22 F. Paige and S. Protopopescu, in Supercollider Physics, p. 41, ed. D. Soper, World Scientific, (1986).

15-23 R. Engel, Z. Phys. **C66** (1995) 203;
R. Engel, 'PHOJET manual', preprint SI-95-05, University of Siegen (1995).

15-24 A. Capella *et al.*, Phys. Rep. **236** (1994) 227.

15-25 P. Aurenche *et al*., Phys. Rev. **D45** (1992) 92;
P. Aurenche *et al*., Comp. Phys. Comm. **83** (1994) 107

15-26 A. Kupco, 'MC event generators and their predictions for minimum bias events at LHC energies', ATLAS Internal Note ATL-COM-PHYS-99-023 (1999).

15-27 F. Abe *et al.*, Phys. Rev. **D41** (1990) 2330.

15-28 F. Abe *et al.*, Phys. Rev. Lett **61** (1988) 1819.

15-29 N. Moggi (for the CDF collaboration), Nucl. Phys. B Proc. Suppl. **71** (1999), 221.

15-30 G. Ingelman and P. Schlein, Phys. Lett. **152B** (1985), 256.

15-31 R. Bonino *et al.*, Phys. Lett. **211B** (1988) 239.

15-32 E.L. Berger *et al.*, Nucl. Phys. **B286** (1987) 704.

15-33 J.D. Bjorken, 'Final state hadrons in deep inelastic processes and colliding beams', publ. in Proc. of Int. Symposium on Electron and Photon Interactions at High Energies, p. 281, Cornell, (1971).

15-34 A. Donnachie and P.V. Landshoff, Phys. Lett. **B191** (1987) 309;
A. Donnachie and P.V. Landshoff, 'Hard Diffraction at HERA', Proc. of the HERA Workshop, ed. R.D. Peccei, DESY, Hamburg (1987) 351.

15-35 P. Marage, preprint hep-ph/9810551, (1998).

15-36 A. Donnachie and P.V. Landshoff, Nucl. Phys. **B303** (1988) 634.

15-37 A. Brandt *et al.*, 'A Forward Proton Detector at D0', preprint FERMILAB-Pub-97/377 (1997).

15-38 J.A. Crittenden, 'Exclusive Production of Neutral Vector Mesons at the Electron-Proton Collider HERA', preprint DESY-97-068 (1997).

15-39 C. Adloff *et al.*, Z.Phys. **C76** (1997) 613.

15-40 CDF collaboration (M.G. Albrow, for the collaboration), 'Diffractive Dijet Production in CDF', preprint FERMILAB-CONF-98-134-E (1998).

15-41 CDF collaboration (M.G. Albrow, for the collaboration), 'Di-Jet Production by Double Pomeron Exchange', preprint FERMILAB-CONF-98-138-E (1998).

15-42 B. Abbott *et al.*, Phys. Lett. **B440** (1998) 189.

15-43 F. Abe *et al.*, Phys. Rev. Lett **80** (1998) 1156.

15-44 C. Adloff *et al.*, Eur. Phys. J. **C6** (1999) 587.

15-45 K. Terashi (for the CDF and D0 collaborations), 'Rapidity Gap Results from Tevatron', proceedings 13th Topical Conference on Hadron Collider Physics, Mumbai, India, Jan. 14-20, 1999;
K. Goulianos, 'Diffractive Production of Jets, Di-Jets, W+jets and b', XXXIVe Rencontres de Moriond, Les Arcs, France, Mar. 20-27, 1999.

15-46 L. Alvero *et al.*, preprint hep-ph/9805268 (1998).

15-47 J.C. Collins, Phys.Rev. **D57** (1998), 3051.

15-48 L. Alvero *et al.*, preprint hep-ph/9806340 (1998).

15-49 A. Levy, Phys. Lett. **B424** (1998) 191.

15-50 A. Brandt *et al.*, Nucl. Phys. **B514** (1998) 3.

15-51 F.E. Low, Phys. Rev. **D12** (1975) 163.

15-52 S. Nussinov, Phys. Rev. Lett. **34** (1974) 1286.

15-53 J.D. Bjorken and Kogut, Phys. Rev. **D8** (1973) 1341.

15-54 W. Buchmuller, Phys. Lett. **B353** (1995) 335;
W. Buchmuller and A. Hebecker, Phys. Lett **B355** (1995) 573.

15-55 O.J.P. Eboli *et al.*, '(No) Colour in QCD: Charmonium, Charm and Rapidity Gaps', preprint MADPH 96-965 (1996).

15-56 R. Engel and J. Ranft, 'Hard Diffraction and Central Diffraction in Hadron-Hadron and Photon-Hadron Collisions', preprint SI-97-17, University of Siegen, Nov. 1997;
F.W. Bopp *et al.*, 'Rapidity Gaps and the PHOJET Monte Carlo', preprint SI-98-25, University of Siegen, Mar. 1998.

15-57 TOTEM Collaboration, Technical Proposal, CERN / LHCC / 99-07 (1999).

15-58 A. Brandt *et al.*, Nucl. Instr. and Meth. **A327** (1993) 412.

15-59 K. Eggert and G. Morsch, 'Leading Proton Detection in Diffractive Events for an LHC Low-Beta Insertion', preprint CERN-AT-94-09-DI, (1994).

15-60 K. Eggert and G. Morsch, Nucl. Instr. and Meth.**A351** (1994) 174.

15-61 ATLAS Collaboration, First-Level Trigger Technical Design Report, CERN / LHCC / 98-14 (1998).

15-62 F. Abe *et al.*, Phys. Rev. Lett. **79** (1997) 2636.

15-63 G. Ballistoni and S. Tapprogge, 'Studies of Hard Diffraction in ATLAS', ATLAS Internal Note ATL-COM-PHYS-99-022 (1998).

15-64 D. Graudenz and G. Veneziano, Phys. Lett. **B365** (1996) 302.

15-65 M. Heyssler *et al.*, Phys. Lett. **B406** (1997) 95.

15-66 J. Pumplin, Phys. Rev. **D47** (1993) 4820;
J. Pumplin, Phys. Rev. **D52** (1995) 1477.

15-67 A. Berera and J.C. Collins, 'An Estimate of the Double Pomeron Dijet Cross Section at FELIX', preprint VAND-TH-97-07 (1997).

15-68 J.D. Bjorken, Phys. Rev. **D47** (1992) 101.

15-69 A. Schaefer *et al.*, Phys. Lett. **B249** (1990) 331.

15-70 A. Bialas and P.V. Landshoff, Phys. Lett. **B256** (1991) 540.

15-71 J.R. Cudell, O.F. Hernandez, Nucl. Phys. **B471** (1996) 471.

15-72 M.G. Albrow and A. Rostovtsev, private communication.

15-73 P. Bruni and G. Ingelman, Phys. Lett. **B311** (1993) 317.

15-74 F. Abe *et al.*, Phys. Rev. Lett. **78** (1997) 2698.

15-75 M. Derrick *et al.*, Phys. Lett. **B356** (1995) 129.

15-76 H. Fritzsch and K.-H. Streng, Phys. Lett. **B164** (1985) 391.

15-77 M. Heyssler, Z. Phys. **C73** (1997) 299.

15-78 F. Abe *et al.*, Phys. Rev. Lett **77** (1996) 438.

15-79 B. Abbott *et al.*, Phys. Rev. Lett. **82** (1999) 2451.

15-80 G.C. Blazey (for the D0 collaboration), 'Inclusive Jet Production at 630 and 1800 GeV', preprint FERMILAB-CONF-98-367-E (1998).

15-81 J. Alitti *et al.*, Phys. Lett. **B257** (1991) 232.

15-82 S. Catani *et al.*, Nucl. Phys. **B406** (1993) 187.

15-83 W.B. Kilgore and W.T. Giele, preprint hep-ph/9903361 (1999).

15-84 W.T. Giele *et al.*, Nucl. Phys. **B403** (1993) 633.

15-85 B. Abbott *et al.*, Eur. J. Phys. **C5** (1998) 687.

15-86 H. Stenzel and S. Tapprogge, 'Prospects of Studies with QCD Jets in ATLAS', ATLAS Internal Note ATL-COM-PHYS-99-021 (1999).

15-87 A.D. Martin *et al.*, Phys. Rev. **D50** (1994) 6734.

15-88 M. Gluck *et al.*, Z. Phys. **C67** (1995) 433.

15-89 W.T. Giele, E.W.N. Glover and J. Yu, Phys.Rev. **D53** (1996) 120.

15-90 F. Abe *et al.*, Phys. Rev. Lett **70** (1993) 713.

15-91 M. Klasen and G. Kramer, Phys. Rev. **D56** (1997) 2702.

15-92 M.H. Seymour, Nucl. Phys. **B513** (1998) 269.

15-93 H. Akimoto *et al.*, Phys. Rev. **D**, in preparation.

15-94 W.T. Giele, E.W.N. Glover and D.A. Kosover, Phys.Rev. **D52** (1995) 1486.

15-95 S.D. Ellis and D.E. Soper, Phys. Rev. Lett. **74** (1995) 5182.

15-96 F. Abe *et al.*, 'The Two-Jet Differential Cross-Section at CDF', preprint FERMILAB-CONF-93-201-E (1993).

15-97 S. Abachi *et al.*, 'Measurement of the Inclusive Triple Differential Dijet Cross Section, $d^3\sigma/dE_T d\eta_1 d\eta_2$ in $p\bar{p}$ Collisions at $\sqrt{s}$ = 1.8 TeV', preprint FERMILAB-CONF-95-217-E (1995).

15-98 T. Asakawa (for the CDF and D0 collaborations), 'Dijet Results from CDF and D0', proceedings 13th Topical Conference on Hadron Collider Physics, Mumbai, India, Jan. 14-20, 1999.

15-99 B. Abbott *et al.*, 'The Dijet Mass Spectrum and a Search for Quark Compositeness in $p\bar{p}$ Collisions at $\sqrt{s}$ = 1.8 TeV', preprint FERMILAB-PUB-98-220-E (1998).

15-100 A.H. Mueller and H. Navelet, Nucl. Phys. **B282** (1987) 727.

15-101 W.J. Stirling, Nucl. Phys. **B423** (1994) 56.

15-102 V. Del Duca and C.R. Schmidt, Phys. Rev. **D51** (1995) 2150.

15-103 L.H. Orr and W.J.Stirling, Phys.Lett. **B436** (1998) 372.

15-104 B. Abbott *et al.*, 'The Azimuthal Decorrelation of Jets Widely Separated in Rapidity', preprint FERMILAB-CONF-97-371-E (1997).

15-105 F. Abe *et al.*, Phys. Rev. Lett **75** (1995) 608;
F. Abe *et al.*, Phys. Rev. **D54** (1996) 4221.

15-106 F.A. Berends *et al.*, Phys. Lett. **B232** (1989) 266.

15-107 F.A. Berends and H. Kuijf, Nucl. Phys. **B353** (1991) 59.

15-108 B. Andersson, G. Gustafson and T. Sjostrand, Phys. Lett. **B94** (1980) 211

15-109 F. Abe *et al.*, Phys. Rev. **D50** (1994) 5562.

15-110 B. Abbott *et al.*, 'Colour Coherent Radiation in Multi-jet Events from $p\bar{p}$ Collisions at $\sqrt{s}$ = 1.8 TeV', preprint FERMILAB-Pub-97/201-E (1997).

15-111 G. Calucci and D. Treleani, Nucl. Phys. B, Proc. Suppl. **71** (1999) 392.

15-112 F. Abe *et al.*, Phys. Rev. **D56** (1997) 3811.

15-113 H. Baer *et al.*, Phys. Rev. **D42** (1990) 61.

15-114 P. Aurenche *et al.*, Phys. Rev. **D42** (1990) 1440.

15-115 E.L. Berger and J. Qiu, Phys. Rev. **D44** (1991) 2002.

15-116 S. Frixione, Phys. Lett. **B429** (1998) 369.

15-117 L.E. Gordon and W. Vogelsang, Phys. Rev. **D50** (1994) 1901.

15-118 C. Balazs *et al.*, Phys. Rev. **D57** (1998) 6934.

15-119 C. Balazs and C.-P. Yuan, preprint hep-ph/9810319 (1999).

15-120 V. Barger *et al.*, Phys. Lett. **B232** (1989) 371.

15-121 H. Baer *et al.*, Phys. Lett **B234** (1990) 127.

15-122 F. Abe *et al.*, Phys. Rev. **D57** (1998) 1359.

15-123 F. Abe *et al.*, Phys.Rev. **D57** (1998) 67.

15-124 R.G. Badalian and S. Heppelmann, Phys. Rev. **D57** (1998) 4367.

15-125 M. Stratmann and W. Vogelsang, Phys. Rev. **D52** (1995) 1535.

15-126 E.L. Berger and L.E. Gordon, Phys. Rev. **D54** (1996) 2279.

15-127 B. Bailey *et al.*, Phys. Rev. **D54** (1996) 1896.

15-128 F. Abe at al., preprint hep-ex/9902001 (1999).

15-129 F. Abe *et al.*, Phys. Rev. Lett. **77** (1996) 5005.

15-130 C. Balazs and C.-P. Yuan, Phys. Rev. **D56** (1997) 5558.

15-131 F. Abe *et al.*, 'Measurement of Z^0 and Drell-Yan Production Cross Section Using Dimuons in $p\bar{p}$ Collisions at $\sqrt{s}$ = 1.8 TeV', preprint FERMILAB-PUB-98-280-E (1998).

15-132 B. Abbott *et al.*, 'Measurement of the High-Mass Drell-Yan Cross Section and Limits on Quark-Electron Compositeness Scales', preprint FERMILAB-PUB-98-391-E (1998).

15-133 E. Mirkes and J. Ohnemus, Phys.Rev. **D51** (1995) 4891.

15-134 F. Abe *et al.*, Phys. Rev. Lett. **77** (1996) 2616.

15-135 B. Abbott *et al.*, Phys. Rev. Lett. **80** (1998) 5498.

15-136 P.B. Arnold and R. Kauffmann, Nucl. Phys. **B349** (1991) 381.

15-137 G.A. Ladinsky and C.P. Yuan, Phys.Rev. **D50** (1994) 4239.

15-138 C.E. Gerber (for the CDF and D0 collaborations), 'Review of W and Z production at the Tevatron', preprint FERMILAB-Conf-98-148-E (1998).

15-139 C.-P. Yuan, 'Gluon Resummation in Vector Boson Production and Decay', preprint CTEQ-851 (1998), Talk given at the XXXIIIe Rencontres de Moriond 'QCD and High Energy Hadronic Interactions', 21-28 March 1998, Les Arcs, France.

15-140 R.K. Ellis and S. Veseli, Nucl. Phys. **B511** (1998) 649.

15-141 A.D. Martin, R.G. Roberts and W.J. Stirling, Phys. Lett. **B387** (1996) 419.

15-142 F.A. Berends *et al.*, Nucl. Phys. **B357** (1991) 32.

15-143 V. Barger *et al.*, Phys. Rev. **D40** (1989) 2888.

15-144 B. Abbott *et al.*, 'A Measurement of the Ratio of Production Cross Sections for W+1 Jet to W+0 Jets and Comparisons to QCD', preprint FERMILAB-Conf-97/369-E (1997).

15-145 F. Abe *et al.*, Phys. Rev. Lett. **81** (1998) 1367.

15-146 CDF collaboration (B. Flaugher, for the collaboration), 'Measurement of $R_{10}(\sigma(W+ \geq 1 \text{ jet})/\sigma(W))$ at CDF', preprint FERMILAB-CONF-98-339-E (1998).

15-147 B. Abbott *et al.*, 'Colour Coherence in W + Jet Events', preprint FERMILAB-Conf-97/372-E(1997).

15-148 J. Amundson *et al.*, Phys. Rev. **D57** (1998) 527.

15-149 E. Boos *et al.*, preprint hep-ph/9903215 (1999).

15-150 U. Baur *et al.*, Phys.Lett.**B318** (1993) 544.

15-151 F. Abe *et al.*, Phys. Rev. Lett. **67** (1991) 1502.

15-152 V. Barger *et al.*, Phys. Lett. **B338** (1994) 336.

15-153 J. Ellison and J. Wudka, 'Study of Trilinear Gauge Boson Couplings at the Tevatron Collider', preprint UCR-D0-98-01 (1998).

15-154 J. Ohnemus, Phys.Rev. **D50** (1994) 1931.

15-155 U. Baur *et al.*, Phys. Rev. **D53** (1996) 1098.

15-156 U. Baur *et al.*, Phys. Rev. **D48** (1993) 5140.

15-157 U. Baur *et al.*, Phys. Rev. **D50** (1994) 1917.

15-158 U. Baur *et al.*, Phys. Rev. **D57** (1998) 2823.

15-159 J. Ohnemus, Phys. Rev. **D51** (1995) 1068.

15-160 U. Baur *et al.*, Phys. Rev. **D51** (1995) 3381.

15-161 J. Huston, private communication.

15-162 S. Frixione, M.L. Mangano, P. Nason and G. Ridolfi, in 'Heavy Flavours II', eds. A.J. Buras and M.Lindner, Advanced Series on Directions in High Energy Physics, World Scientific Publishing Co., Singapore.

15-163 M. Mangano, 'Heavy flavour production', Talk given at the LHCC workshop 'Theory of LHC processes', Feb. 1998, CERN.

15-164 P. Nason *et al.*, Nucl. Phys. **B303** (1988) 607;
P. Nason *et al.*, Nucl. Phys. **B327** (1989) 49;
erratum *ibid.*, Nucl. Phys. **B335** (1990) 260.

15-165 W. Beenakker *et al.*, Nucl. Phys. **B351** (1991) 507.

15-166 F. Abe *et al.*, Phys. Rev. Lett. **79** (1997) 578.

15-167 F. Abe *et al.*, Phys. Rev. Lett. **79** (1997) 572.

15-168 S. Abachi *et al.*, Phys. Lett. **B370** (1996) 239;
B. Abbott *et al.*, 'Small Angle J/ψ Production in $p\bar{p}$ Collisions at $\sqrt{s}$ = 1.8 TeV', preprint FERMILAB PUB-98/237-E (1998).

15-169 K. Sridhar, Mod. Phys. Lett. **A11** (1996) 1555.

15-170 B. Cano-Coloma and M.A. Sanchis-Lozano, Nucl. Phys. **B508** (1997) 753.

15-171 P. Mathews *et al.*, preprint hep-ph / 9901276 (1999).

15-172 V. Barger *et al.*, Phys. Lett **B371** (1996) 111.

15-173 F. Abe *et al.*, Phys. Rev. Lett. **75** (1995) 4358.

15-174 E. Braaten *et al.*, 'Associated Production of Y and Weak Gauge Bosons in Hadron Collisions', preprint UTPT-98-18 (1998).

15-175 S. Abachi *et al.*, Phys. Rev. Lett. **74** (1995) 3548.

15-176 F. Abe *et al.*, Phys. Rev. Lett. **71** (1993) 500;
F. Abe *et al.*, Phys. Rev. Lett. **71** (1993) 2396;
F. Abe *et al.*, Phys. Rev. Lett. **71** (1993) 2537;
F. Abe *et al.*, Phys. Rev. Lett. **75** (1995) 1451;
F. Abe *et al.*, Phys. Rev. **D50** (1994), 4252.

15-177 M. Mangano *et al.*, Nucl. Phys. **B373** (1992) 295.

15-178 ATLAS Collaboration, Inner Detector Technical Design Report Vol. I, CERN / LHCC 97-16 (1997).

15-179 S. Baranov and M. Smizanska, 'Beauty production overview from Tevatron to LHC', ATLAS Internal Note ATLAS-PHYS-98-133 (1998).

15-180 R. Vogt and S.J. Brodsky, Nucl. Phys. **B438** (1995) 261.

15-181 R.C. Hwa, Phys. Rev. **D51** (1995) 85.

15-182 G.A. Alves *et al.*, Phys. Rev. Lett. **72** (1994) 812.

15-183 M. Adamovich *et al.*, Phys. Lett. **B305** (1993) 402.

15-184 A. Likhoded and A. Berezhnoy, private communication.

15-185 R. Bonciani *et al.*, Nucl. Phys. **B529** (1998) 424.

15-186 W. Bernreuther *et al.*, Phys. Lett. **B368** (1996) 153.